

ABSTRACT

Title of Document: ELECTRONIC TRANSPORT IN BISMUTH
SELENIDE IN THE TOPOLOGICAL
INSULATOR REGIME

Dohun Kim, Doctor of Philosophy, 2013

Directed By: Professor, Michael S. Fuhrer,
Department of Physics

The 3D topological insulators (TIs) have an insulating bulk but spin-momentum coupled metallic surface states stemming from band inversion due to strong spin-orbit interaction, whose existence is guaranteed by the topology of the band structure of the insulator. While the STI surface state has been studied spectroscopically by e.g. photoemission and scanned probes, transport experiments have failed to demonstrate clear signature of the STI due to high level of bulk conduction. In this thesis, I present experimental results on the transport properties of TI material Bi_2Se_3 in the absence of bulk conduction (TI regime), achieved by applying novel *p*-type doping methods. Field effect transistors consisting of thin (thickness: 5-17 nm) Bi_2Se_3 are fabricated by mechanical exfoliation of single crystals, and a combination of conventional dielectric (300 nm thick SiO_2) and electrochemical or chemical gating methods are used to move the Fermi energy through the surface Dirac point inside bulk band gap, revealing the ambipolar gapless nature of transport in the Bi_2Se_3 surface states. The minimum

conductivity of the topological surface state is understood within the self-consistent theory of Dirac electrons in the presence of charged impurities. The intrinsic finite-temperature resistivity of the topological surface state due to electron-acoustic phonon scattering is measured to be 60 times larger than that of graphene largely due to the smaller Fermi and sound velocities in Bi_2Se_3 , which will have implications for topological electronic devices operating at room temperature. Along with semi-classical Boltzmann transport, I also discuss 2D weak anti-localization (WAL) behavior of the topological surface states. By investigating gate-tuned WAL behavior in thin (5-17 nm) TI films, I show that WAL in the TI regime is extraordinarily sensitive to the hybridization induced quantum mechanical tunneling between top and bottom topological surfaces, and interplay of phase coherence time and inter-surface tunneling time results in a crossover from two decoupled (top and bottom) symplectic 2D metal surfaces to a coherently coupled single channel. Furthermore, a complete suppression of WAL is observed in the 5 nm thick Bi_2Se_3 film which was found to occur when the hybridization gap becomes comparable to the disorder strength.

ELECTRONIC TRANSPORT IN BISMUTH SELENIDE
IN THE TOPOLOGICAL INSULATOR REGIME

By

Dohun Kim

Dissertation submitted to the Faculty of the Graduate School of the
University of Maryland, College Park, in partial fulfillment
of the requirements for the degree of
Doctor of Philosophy
2013

Advisory Committee:

Professor Michael S. Fuhrer, Chair

Assistant Professor Johnpierre Paglione

Associate Professor Min Ouyang

Associate Research Scientist William G. Cullen

Professor Ichiro Takeuchi

© Copyright
Dohun Kim
2013

To my parents 김 건 태, 이 증 균

Acknowledgements

On writing this thesis organizing my past works in Ph.D. study, I feel strongly more than ever that my journey so far would not be possible without supports from people around me. First and foremost, my parents, 김건태 and 이증균, have always encouraged my path as a scholar. All of my rational abilities are inherited from them.

Mentorship is an essential part in any higher level study, and doctorate course is not an exception. I express my sincere gratitude to my advisor Prof. Michael S. Fuhrer. As a student having an engineering background, diverting from what I have learned in undergraduate was not an easy task especially when it comes to entering the field of physics research. He is the first person who acknowledged my motivation in studying physics. He is always open to discussing with people and guided us by first knowing exactly what one's strength is. I particularly admire his comprehensive knowledge in general subjects of condensed matter physics and ability to see the big picture. He taught me by showing how academic insight can lead to consistent interpretation on the problem at hand. It is mutual faith between him and I which made fruitful accomplishments possible. Most definitely I will be a mentor someday, and it is my hope that I become proud of myself by putting lessons from him into practice.

I would like to thank the members of my dissertation committee, Prof. Johnpierre Paglione, Prof. Min Ouyang, Dr. William G. Cullen and Prof. Ichiro Takauchi, for their guidance that leads to the completion of this thesis. I would like to thank Dr. Nicholas Butch, Paul Syers, and Kevin Kirshenbaum for providing me high quality Bi_2Se_3 starting

material. My academic accomplishments during Ph.D study were possible entirely because I fortuitously had colleagues who are experts in single crystal growth techniques.

I would like to thank all the people who have helped me in finishing the work in this thesis: Dr. Chaun Jang, Dr. SungJae Cho, Dr. Claudia Ojeda, Dr. Wenzhong Bao, Dr. Daniel Lenski, Dr. Enrique Cobas, Dr. Alexandra Curtin, Xinghan (Harold) Cai, Jack Hellerstedt, Liang Li, Jinglei Ping, Jacob Tosado, Dr. Yilin Wang, Kristen Burson, Michelle Zimmermann and Mahito Yamamoto. I would like to thank Prof. Sankar Das Sarma, Prof. Shaffique Adam, Prof. Euyheon Hwang and Qiuzi Li for sharing of theoretical insights. My gratitude is also extended to all my friends.

I do realize that completing Ph.D study is only the starting point of my future career and I am sure that unprecedented adversities will come as I move on. I appreciate what they have done for me during my Ph.D. program and cherish all the wonderful memories. With helpful communication and supports that I have enjoyed, I feel that I am already seeing the solution. I hope that their memories with me are equally joyful as mine.

2013. 3. 10. Late night in my office,

Dohun Kim

Table of Contents

Acknowledgements.....	iii
Table of Contents	v
List of Figures.....	vii
Chapter 1 Introduction to topological insulators	1
1.1 Introduction.....	1
1.2. Bi ₂ Se ₃ : toward realization of topological transport regime.....	9
1.3 Outline of the thesis	12
Chapter 2 Charge transport in gapless Dirac surface states.....	14
2.1 Transport theory of surface charge transport in Dirac system.....	14
2.2 Minimum conductivity and Self-consistent theory.....	18
Chapter 3 Experimental methods.....	21
3.1 Bi ₂ Se ₃ field effect transistor fabrication.....	21
3.1.1 Mechanical exfoliation of bulk Bi ₂ Se ₃ single crystals	21
3.1.2 Field effect transistor fabrication process	25
3.2 Novel p-type doping methods for achieving topological transport regime	28
3.2.1 Charge transfer doping with organic molecules	28
3.2.2 Polymer electrolyte gating	29
3.3 Measurement setup	30
3.3.1 Four probe AC lock-in technique	30
3.3.2 Variable temperature ⁴ He cryostat.....	32
Chapter 4 Surface conduction of topological Dirac electrons in bulk insulating Bi ₂ Se ₃ .	35
4.1 Electronic transport in the topological insulator regime.....	36
4.1.1 <i>p</i> -type doping effects near room temperature	36
4.1.2 Gapless ambipolar field effect	39
4.1.3 Single band conduction in the topological transport regime	42
4.1.4 Absence of band bending effect : the role of bulk capacitance	44
4.2 Charge inhomogeneity driven minimum conductivity in Dirac surface states.....	51
4.2.1 Charged-impurity limited transport in the Boltzmann transport regime	51
4.2.2 Charge inhomogeneity driven electron hole puddles and minimum conductivity.....	55
4.3 Conclusion	59

Chapter 5 Intrinsic electron-acoustic phonon resistivity of Bi_2Se_3 in the topological insulator regime	60
5.1 Temperature dependent carrier density in gate tuned Bi_2Se_3 : experiment.....	61
5.2 Temperature dependent carrier density in gate tuned Bi_2Se_3 : modelling	65
5.3 Electron-acoustic phonon resistivity.....	68
5.3 Conclusion	76
Chapter 6 Coherent topological transport on the surface of Bi_2Se_3	78
6.1 Phase coherent transport	79
6.1.1 Weak localization and anti-localization.....	79
6.1.2 Weak anti-localization in topological insulator thin films in multi-channel limit	82
6.2 Finite size effects in thin films of topological insulators.....	84
6.2.1 Inter-layer coupling and band gap opening	84
6.2.2 Signatures of hybridization induced band gap in gate tuned semi-classical transport	87
6.3 Weak anti-localization in the topological insulator regime	91
6.3.1 Coherently coupled single channel to multichannel crossovers	91
6.3.2 Physical origin of the crossovers	94
6.4 Conclusion	97
Chapter 7 Conclusion and outlook.....	99
Appendix A.....	101
Appendix B	103
Bibliography	106

List of Figures

Figure 1.1 Integer Quantum Hall effect. (a) Quantized Hall conductivity as a function of external magnetic field perpendicular to the sample. (b) Bulk gap due to Landau levels and gapless edge states at the boundary in IQH state.	4
Figure 1.2 Helical edge states in 2D Topological insulator (QSH) state.	6
Figure 1.3 Observation of QSH state in a HgTe/CdTe quantum well. Figure from Ref. [11].	7
Figure 1.4 Surface band structure of a 3D topological insulator.	9
Figure 1.5 Surface band structure of representative 3D topological insulators. (a) Theoretically predicted band structure for Sb ₂ Se ₃ (upper left), Sb ₂ Te ₃ (upper right), Bi ₂ Se ₃ (lower left), and Bi ₂ Te ₃ (lower right) -Figure reproduced from Ref. [2] (b) Angle-resolved photoemission of Bi ₂ Se ₃ showing bulk conduction and valence bands (black solid) and surface band (blue and red solid) -Figure reproduced from Ref. [21, 22] (c) Spin polarization in Bi ₂ Se ₃ along k _x direction-Figure reproduced from Ref. [15]	11
Figure 2.1 Charge transport in graphene on 300 nm SiO ₂ (a) Longitudinal conductivity σ vs. back gate induced carrier density. (b) Hall carrier density n_H vs. back gate induced carrier density.	15
Figure 2.2 Potential fluctuation and electron-hole puddle formation near Dirac point. ..	19
Figure 3.1 (a) Crystal structure of Bi ₂ Se ₃ illustrating the unit cell and lattice vectors (black) and the quintuple layer (QL) unit (red). Picture from Ref. [2] (b) Bulk Bi ₂ Se ₃ grown by binary flux method (Prof. Johnpierre Paglione group at University of Maryland [24].	22
Figure 3.2 Optical image of a thin Bi ₂ Se ₃ flake dispersed on SiO ₂ /doped-Si substrate. Thicknesses indicated are confirmed with AFM topography measurements.	24
Figure 3.3 (a) Optical and (b) Atomic Force Microscopy of a few quintuple layer Bi ₂ Se ₃ flake. (c) Height profile along the white vertical line indicated in (b).	25
Figure 3.4 Schematics of device structure and <i>p</i> -type doping schemes. (a) Charge transfer doping with F4TCNQ organic molecules. (b) Polymer electrolyte (Polyethylene oxide : LiClO ₄ = 1 : 0.12 by weight ratio) top gating method.	30
Figure 3.5 Schematic of gate-tuned longitudinal and Hall resistivity measurement setup	32
Figure 3.6 Quantum Design PPMS equipped with pulse condenser and 9T superconducting magnet.	33
Figure 4.1 Charge transfer <i>p</i> -type doping with F4TCNQ. (a) Hall carrier density n_H at zero gate voltage and at room temperature for 15 devices with (red) or without (blue) F4TCNQ deposition ranging in thickness from 5 to 17 nm. Arrows indicate change of n_H measured in the same sample. (b) Conductivity σ of a F4TCNQ-doped 12 nm thick device as a function of n_H at 300 K and ambient condition. The device was exposed to air for 1 (black square), 15 (red circle), and 25 (green triangle) days.	37
Figure 4.2 Electrolyte gating of a 10 nm Bi ₂ Se ₃ device at 300K. Resistivity (ρ_{xx}) and sheet carrier density determined from Hall voltage (n_H) as a function of electrolyte gate voltage.	39
Figure 4.3 Gate tuned transport in TI regime. (a) Longitudinal resistivity (ρ_{xx}) and (b) Hall carrier density n_H of device 4 (F4TCNQ doped) as functions of back gate voltage at	

various temperatures from 2 K to 50 K indicated in caption. The inset shows an optical micrograph of the device. The scale bar is 2 μ m.	41
Figure 4.4 Single band conduction in TI regime. Hall resistivity ρ_{xy} of the F4TCNQ-doped 10 nm Bi ₂ Se ₃ device as a function of magnetic field B at a temperature of 2 K at different carrier densities tuned by the back gate electrode.....	44
Figure 4.5 Dual gate transport in TI regime. (a) Schematic of dual dielectric gating on a F4TCNQ doped Bi ₂ Se ₃ device. (b) Polar plot of the normalized longitudinal resistivity ρ of a dual gated Bi ₂ Se ₃ thin film device as a function of total magnitude of displacement field (D_{total}) and gating asymmetry factor α (defined in the text).	47
Figure 4.6 Displacement field induced surface charge density. (a) Capacitor network model of a dual gated Bi ₂ Se ₃ thin film device. (b) Calculated charge densities for top (blue) and bottom (red) surfaces as a function of total magnitude of applied field. Dashed black line is carrier density for symmetric applied field ($\alpha=0$). The solid, dot, dashed-dot lines are charge densities calculated for highly asymmetric applied field ($\alpha=-0.5$) in the strong, intermediate, and weak interlayer coupling limits, respectively.....	51
Figure 4.7 Transport properties of Bi ₂ Se ₃ surface state. (a) The conductivity per surface vs. carrier density per surface $\sigma(n)$ at zero magnetic field for five different devices. Device 1 to 3 are electrolyte gated and device 4 and 5 are F4TCNQ doped. The inset shows $\sigma(n)$ near the Dirac point. Dashed lines are fits to Eqn. (1a). Transport data outside the topological regime ($n > n_{bulk} = 5 \times 10^{12}/\text{cm}^2$) are denoted as dotted curves. (b) Hall carrier density per surface vs. carrier density measured at the same conditions as in (a). Dashed lines show residual carrier density n^* (defined in the text) for different devices (c) Variation of field effect mobility as a function of carrier density. Dashed curves indicate the region $ n < n^*$ within which electron and hole puddles dominate transport.	54
Figure 4.8 Charge inhomogeneity driven electron-hole puddles in (a) graphene measured using scanning single electron transistor [36] ($n^* \sim 10^{11}/\text{cm}^2$) (b) Mn-doped Bi ₂ Se ₃ using scanning tunneling microscope [53] ($n^* \sim 10^{12}/\text{cm}^2$)	56
Figure 4.9 Minimum conductivity and charge inhomogeneity vs. inverse mobility. (a) Residual carrier density n^* vs. inverse field effect mobility ($1/\mu_{FE}$) and (b) minimum conductivity σ_{min} vs. $1/\mu_{FE}$. Shaded areas indicate the expectations of the self-consistent theory of Ref. [30], symbols are experimental data.....	58
Figure 5.1 Temperature dependent carrier density : experiment (a) Measured Hall carrier density (n_H) of a thin exfoliated Bi ₂ Se ₃ device as a function of back gate voltage (V_g) and temperature (T). Pink dashed curve shows a T dependent trace of charge neutrality point (CNP; $V_{g,0}$) (b) n_H vs. V_g at various temperatures indicated by dashed lines in (a). Dashed lines indicate points of charge neutrality. The inset shows an optical micrograph of the device. The scale bar is 2 μ m. (c) n_H vs. T at $V_g=-90$ as indicated by a vertical dashed line (a).	64
Figure 5.2 Determination of bulk valence band edge. Arrhenius plot of excess carrier density $n = C_g(V_{g,0}(T)-V_{g,0}(2K))$ in the temperature range $50 < T < 200$. Linear fit to the form $n=n_0 \exp(-E_v/k_B T)$ results the position of bulk valence band edge $E_v=60\text{meV}$	65
Figure 5.3 Temperature dependent carrier density : calculation (a) Calculated surface band carrier density as a function of V_g and T using a thermal activation model discussed in text. (b) Energy-dependent density of states $D(E)$ for the thermal activation model, showing surface (red and blue solid lines) bands and bulk valence (black solid line) band.	68

Figure 5.4 Temperature dependent resistivity : experiment (a) Longitudinal resistivity ρ_{xx} of a 10nm thick Bi_2Se_3 (device 1) as a function of gate voltage V_g and temperature T (b) ρ_{xx} of the device 1 as a function of temperature at different carrier densities for which thermal activation from the bulk is negligible. 70

Figure 5.5 Temperature dependent resistivity : calculation. Calculated total resistivity ρ_{xx} as a function of temperature for different carrier densities $n = 2,3,4,5,6,7,8,9 \times 10^{12} \text{ cm}^{-2}$ from top to bottom. In (a) the charged impurity density is $n_{\text{imp}} = 3 \times 10^{13} \text{ cm}^{-2}$ and the potential fluctuation strength $s = 90 \text{ meV}$. In (b) $n_{\text{imp}} = 1.5 \times 10^{13} \text{ cm}^{-2}$ and $s = 65 \text{ meV}$. 73

Figure 5.6 Electron-phonon coupling strength. Comparison of experimental and theoretical estimation of electron-phonon coupling strength (a) Slope of ρ_{xx} vs. carrier density in the linear temperature regime ($50 \text{ K} < T < 150 \text{ K}$). Dashed line indicates the high carrier density value of the slope used to compare to the theoretical model. (b) Calculated slope $d\rho_{xx}/dT$ vs. n in the linear temperature regime ($50 \text{ K} < T < 150 \text{ K}$). The solid line is the result including only electron-phonon scattering, while the dot-dashed and dashed lines correspond to Fig. 5.4 (a) and (b), respectively 76

Figure 6.1 Quantum correction due to self-intersecting time reversed loops (a) Enhanced backscattering (constructive interference) of a spin-less electron wave function leading to weak localization (b) Suppressed backscattering (destructive interference) of a Dirac electron by acquiring Berry phase of π leading to weak anti-localization..... 80

Figure 6.2 Gate tunable coherent coupling of multi-channels in non TI regime (from Ref. [74]). (a) Optical micrograph and schematic of device structure (b) Measured WAL correction and variation of α as a function of top gate voltage V_{TG} 84

Figure 6.3 ARPES and transport study of opening a band gap in ultrathin Bi_2Se_3 thin films. (a) ARPES band structure of MBE grown ultrathin Bi_2Se_3 films. Figure from Ref. [81] (b) Insulating behavior observed in the transport study of mechanically exfoliated Bi_2Se_3 . Figure from Ref. [83]..... 87

Figure 6.4 (a) AFM image of a 12QL Hall bar device. (b) height profiles of 5,7,12,17QL Bi_2Se_3 thin films. 88

Figure 6.5 Drude transport in thin TI films ranging in thickness from 5 to 17 QL. (a) Longitudinal resistivity ρ_{xx} . (b) sheet carrier density n_{H} determined from Hall measurement as a function of back gate voltage at the temperature of 2K. 89

Figure 6.6 Temperature dependent resistivity of 5QL device. (a) Longitudinal resistivity ρ_{xx} as a function of gate voltage V_g and temperature T . Dashed curve shows a trace of the position of ρ_{max} . (b) ρ_{xx} vs. T at various gate voltages. The inset shows ρ_{max} as a function of T 91

Figure 6.7 Weak anti-localization in the topological insulator regime. Magneto-conductivity $\Delta\sigma$ as a function of perpendicular magnetic field H in (a) 17, (b) 12, (c) 7, and (d) 5QL devices measured at 2 K at gate-induced carrier densities indicated in the legends. Dashed curves show least-square fits to Eqn. 6.1. Zeros of all curves are offset by $0.7 e^2/h$ for clarity. 92

Figure 6.8 Coupled / decoupled coherent transport in Bi_2Se_3 surface states. Variation of the amplitude of weak anti-localization α as a function of 2D carrier density n for 17 (black square), 12 (red circle), 7 (green triangle), and 5 QL (blue triangle) thick devices measured at 2K. For the 12 QL device, the error bars show standard deviations determined from WAL measurements taken at five different thermal runs. The inset shows detailed behavior of suppression of WAL for 5 QL at small n 94

Figure 6.9 Comparison of experimentally measured and theoretically predicted hybridization induced surface gap Δ in Bi_2Se_3 . Solid circles are ARPES data from Ref. [81] and open triangles are theoretical calculation from Ref. [86] 95

Figure 6.10 Phase coherence time (τ_ϕ) vs. interlayer tunneling time (τ_t). Comparison of phase coherence time τ_ϕ determined from fit to Eqn. 6.1 and transport scattering time to interlayer tunneling time τ_t estimated from surface hybridization induced energy gap Δ as a function of 2D carrier density n . Symbols are experimentally measured τ_ϕ for 17 (black square), 12 (red circle), 7 (green triangle), and 5 QL (blue triangle) devices. The hatched areas with corresponding colors show estimated windows of inter-surface tunneling time τ_t 97

Chapter 1 Introduction to topological insulators

1.1 Introduction

A topological insulator is a bulk insulator in two or three dimensions with an energy gap between conduction and valence bands, but possessing gapless, metallic boundary states which result from the topological nature of the electronic states [1, 2]. The conventional classification of ordered phases of matter is characterized by spontaneous symmetry breaking. For example, a crystalline solid breaks continuous translation symmetry and a ferromagnet breaks continuous rotational symmetry of the vacuum, and examining relevant symmetry breaking served as a starting point for understanding thermodynamic equilibrium states of the solid state system as well as phase transitions between them. In contrast, a topological phase, as exemplified by the topological insulators considered in this thesis, is not associated with breaking of symmetry, but rather is distinct due to a topological invariant of the electronic states of the system. Thus a topological insulator phase includes all states whose electronic structure can be deformed continuously from one to another without changing the topological invariant of the state, which can only be changed through a quantum phase transition corresponding to closing the bulk gap. Thus topological classification of states of matter first deals with identifying topological invariants rather than underlying symmetry of the system in consideration.

Perhaps the simplest way to understand the topological insulator is to consider two exemplars of insulating states, one of which is topologically trivial and the other is nontrivial: the vacuum and the integer quantum Hall (IQH) state [3] , respectively. The

former is an obviously insulating state with an energy gap corresponding to the creation of an electron and positron, and the latter is characterized by a quantized energy gap in the bulk (cyclotron energy) separating Landau levels that are created by confining electrons to two dimensions and subjecting them to a strong perpendicular magnetic field. As discovered in the groundbreaking experiments in 1980 by Klaus von Klitzing, it was found that the IQH state, although gapped in the 2D bulk, shows finite quantized Hall conductivity [3, 4],

$$\sigma_{xy} = n \frac{e^2}{h} \quad (1.1)$$

where e is elementary charge, h is the Planck's constant, and n is an integer (see Fig 1.1a). This quantization is exact not only in the theoretical sense but also can be measured with remarkable accuracy independent of the size or impurities of the sample [5]. Obviously the two states of matter (vacuum and IQH) show quite distinct macroscopic properties although they have similar gapped bulk band structure. Moreover, states of IQH at different n show different quantized values of Hall conductivity, however, transitions from n to m ($n \neq m$) states (or from the vacuum to finite n) cannot be understood by symmetry breaking.

The integer n is an example of a topological invariant. In the IQH case where time reversal symmetry is broken by external magnetic fields, it is called a TKNN (after the authors of Ref [4]: Thouless-Kohmoto-Nightingale-Nijs) invariant or a first Chern number [4]. The topological invariant n can be calculated by a surface integral of the Berry flux over the Brillouin zone (BZ),

$$n = \frac{1}{2\pi} \sum_j \int_{BZ} \nabla \times A_j d^2k \quad (1.2)$$

where $A_j = i \langle u_j | \nabla_k | u_j \rangle$ is the Berry connection, $|u_j\rangle$ are the Bloch wave functions of j^{th} band, and the sum runs over the contributions from all occupied bands. The quantized Hall conductivity is direct consequence of certain topological features of the bulk wave function, i.e., nonzero conductivity is possible since the TKNN invariant of the IQH state is nonzero, and IQH states can be classified based on the value of TKNN invariant. In this sense, we can think of vacuum as having topological invariant of zero (trivial insulator).

Intuitively, one can think of quantized Hall conductivity as resulting from chiral one-dimensional (1D) edge states depending on the direction of the magnetic field, which can be viewed as a result of the classical cyclotron motion of the electrons around the edge (see Fig. 1.1b). In real space this corresponds to existence of gapless metallic states at the edge of 2D bulk due to boundary condition although bulk states are gapped in Landau levels. In terms of the topological classification, these metallic edge states result from topological transition at the boundary where two materials with different topological invariant meet. In a band insulator, transition of topological invariant can be done only when the bulk gap closes. Therefore, a topological state must have gapless (metallic) states on its surfaces, since that area is the border between a topological phase and a trivial phase (e.g. vacuum). What authors in Ref. [4] showed is that the number of these topological gapless edge modes can be predicted by solely using certain topological property of the bulk states. This is an example of ‘bulk-boundary correspondence’ stating that topologically nontrivial insulator with topological invariant m generally has m number of metallic boundary states. The origin of conducting edge modes in IQH state by topological invariant naturally explains the robustness of quantized Hall conductivity as

well. The existence of metallic boundary state is guaranteed by a topological property of the bulk, and particularly in the case of IQH states transport at the edge is determined only by TKNN invariant of the bulk so that size or moderate impurities at the edge do not play significant role unless the bulk states are completely altered. The extremely high precision with which the quantum of conductivity has been measured (1 in 10^9) is characteristic of quantization resulting from a topological invariant [5].

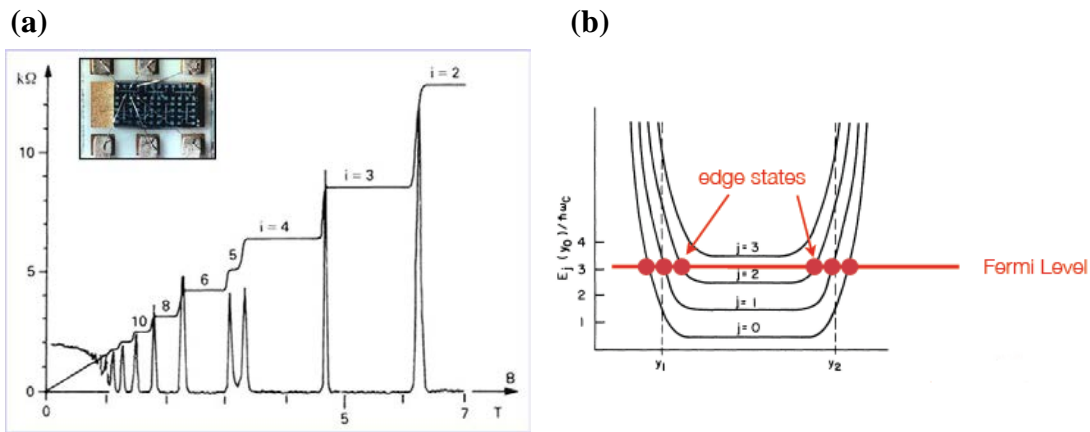


Figure 1.1 Integer Quantum Hall effect. **(a)** Quantized Hall conductivity as a function of external magnetic field perpendicular to the sample. **(b)** Bulk gap due to Landau levels and gapless edge states at the boundary in IQH state.

The classification of states of matter by topological invariant is not necessarily confined to time reversal symmetry-broken systems (as in IQH states) and the subject of this thesis, the 3D topological insulator, is a new class of topologically nontrivial insulator discovered in time reversal invariant (TRI) systems [6]. The time reversal invariant topological insulator in 2D, also referred to as the quantum spin Hall (QSH) phase [7, 8], was first discovered in a model consisting of two superimposed copies of Haldane's model [9], with opposite spins moving in opposite directions on the edge [7-9]. Since IQH is realized in a strong magnetic field spin degree of freedom is quenched and

time reversal symmetry is broken. On the other hand one can conceptually think of two copies of the IQH state including spin degree of freedom, with opposite spin and effective magnetic field (see Fig. 1.2), together which obviously preserves time reversal symmetry. The metallic edge modes of such a state necessarily have opposite chirality for opposite spin; hence momentum (current direction) is closely locked to electron spin. In this sense QSH exhibits a spin-dependent metallic edge state. In the TRI system the TKNN invariant necessarily vanishes when the Berry curvature is integrated over the Brillouin Zone hence it appears necessary to find a new invariant which distinguishes the QSH phase from a trivial insulator. It was shown that the topological invariant in TRI can be classified by a so-called Z_2 invariant [7]. In this classification scheme there are two classes of topological states of insulators: topologically trivial insulator having even integer Z_2 invariant and nontrivial insulator with odd integer Z_2 invariant. It was first theoretically shown that the proposed 2D system of two copies of IQH states has odd Z_2 invariant hence falls into topologically nontrivial insulator [7]. Therefore by applying bulk-boundary correspondence, one can immediately see that this system, although gapped in 2D bulk, will have conducting edge modes which will show quantized conductivity of odd integer $\times 2$ (spin) $\times e^2/h$.

This conductance quantization requires time reversal invariance. Given TRI, backscattering in 1D edge channel is not allowed considering elastic scattering off a non-magnetic impurity on the edge of a topological insulator. Because of spin-momentum locking the initial and backscattered final states necessarily have opposite spin, thus exhibit perfect destructive interference. Therefore, given TRI no backscattering is

allowed and in this sense robustness of quantized edge conductivity of odd integer $\times 2$ (spin) $\times e^2/h$ is said to be ‘topologically protected’.

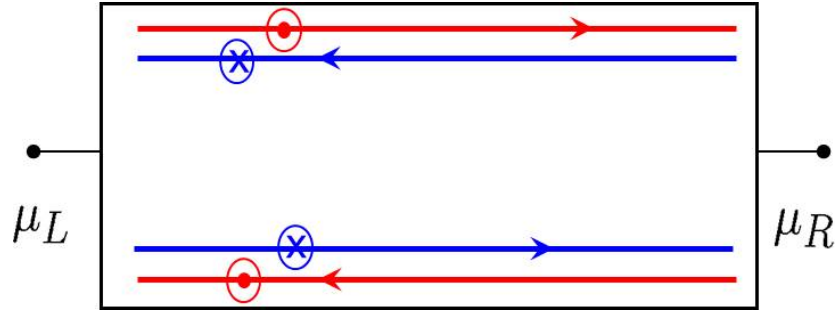


Figure 1.2 Helical edge states in 2D Topological insulator (QSH) state..

How can a TRI topological insulator be realized? The necessary type of effective magnetic field, opposite for opposite spins, can originate from spin-orbit interactions, and experimentally realizable in certain heavier elements having inverted electronic band. After the theoretical prediction [10], QSH states were experimentally discovered in HgTe/CdTe quantum wells [11]. Figure 1.3 shows the observation of QSH state in HgTe/CdTe as inferred by transport measurement. The authors showed that below critical thickness of 6.7 nm HgTe is ordinary insulator having nearly infinite electrical resistance when the Fermi level is tuned inside the bulk gap (Fig. 1.3, I). However, for thickness exceeding 6.7 nm the HgTe becomes band inverted QSH state and the existence of edge state was confirmed by measuring quantized conductance of $1 \times 2e^2/h$ inside the bulk gap. As the measurement shows HgTe was found to have Z_2 invariant of one. The initial experiment detected only the existence of metallic edge state by measuring electrical conductance which cannot resolve spin polarization. More recently, the spin polarization

of the upper/lower edge channels was confirmed in a split top gated HgTe quantum well device [12].

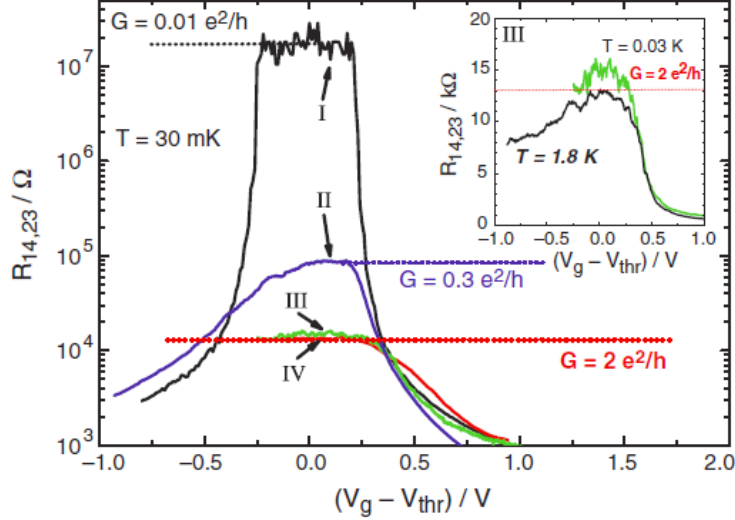


Figure 1.3 Observation of QSH state in a HgTe/CdTe quantum well. Figure from Ref. [11]

It is natural to ask if there is a 3D counterpart to the QSH state. Unlike IQH state which exists only in 2D, it was predicted that a 3D analog of QSH is possible [6]. The topological classification based on Z_2 invariant is valid in 3D as well and it has been shown that addition of one more dimension (k_z) leads to four topological invariants to uniquely define topological state of matter [1, 6]. Consequently the Z_2 invariants in 3D are denoted in the form of $(\nu_0, \nu_1, \nu_2, \nu_3)$. $\nu_0 = \nu_1 = \nu_2 = \nu_3 = 0$ corresponds to ordinary insulator (topologically trivial). $\nu_0 = 0, \nu_1, \nu_2, \nu_3 \neq 0$ corresponds to weak topological insulator, and this state is conceptually equivalent to 3D stack of 2D topological insulators (QSH) [1]. The weak topological insulator has an even number of Dirac cones on its surface and is not robust to (non-magnetic) disorder.

Most importantly, $\nu_0 = 1$ corresponds to a new state of matter called a ‘strong topological insulator (STI)’, which cannot be interpreted as a stack of 2D QSH insulators

[1]. In a strong topological insulator the surface Fermi circle encloses an odd number of Dirac points [2, 13]. The surface electronic structure of a STI is similar to graphene [14], except rather than having four Dirac points (2 valley x 2 spin) there are an odd number of Dirac points. The exact number of Dirac points depends on the material [2]. Unlike an ordinary metal, which has up and down spins at every point on the Fermi surface, the surface states are not spin degenerate [15]. Since TRI requires that states at momenta $\hbar k$ and $-\hbar k$ have opposite spin, the spin must rotate with k around the Fermi surface, as indicated in Fig. 1.4 This leads to a non-trivial Berry phase of π acquired by an electron going around the Fermi circle. The existence of spin polarized metallic surface state, absence of back scattering by TRI disorders, and non-trivial Berry phase are a few of novel electronic properties of STIs. Many theoretical predictions have been made discussing, for example, anomalous magneto-electric response of STIs [16], possibility of observing magnetic monopoles on STI/ferromagnet interfaces [17], and realization of long sought Majorana fermion bound states at STI/superconductor interfaces [18]. As I show in the next section, 3D STIs quickly attracted intensive research efforts, and soon after its general theoretical prediction they were experimentally realized in a number of bismuth- and/or antimony-containing compounds having strong spin-orbit coupling [2, 13, 15].

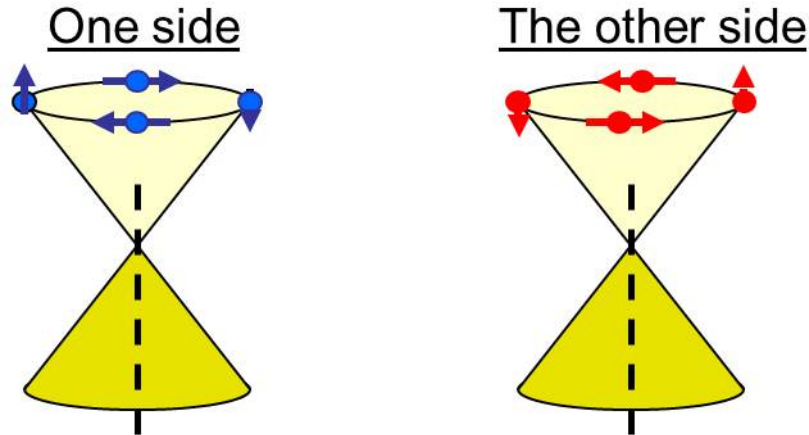


Figure 1.4 Surface band structure of a 3D topological insulator.

1.2. Bi_2Se_3 : toward realization of topological transport regime

The proposed 3D topological insulator phase was first experimentally confirmed in $\text{Bi}_x\text{Sb}_{1-x}$ compounds (first generation) [19]. Figure 1.5 shows comparison of theoretical prediction and experimental identification of so called the second generation of topological insulators in 3D [20]. Using first principle calculation, the authors of Ref. [2] predicted existence of gapless Dirac surface bands in materials such as Bi_2Se_3 , Bi_2Te_3 (Fig 1.5a). Surface states in these materials were examined using angle resolved photo electric spectroscopy (ARPES) technique [21, 22], which is capable of directly map surface electronic band structure, and it was found that indeed there are robust metallic surface states in these materials (Fig.1.5 b). Spin polarization of surface states were also confirmed in more recent studies using spin resolved ARPES technique [15] (Fig 1.5c).

ARPES measurements indicate Bi_2Se_3 has a single Dirac cone, gapless surface state in the bulk gap. Bi_2Se_3 seems to be one of the most promising TIs for practical

applications in that it has a large bulk band gap of 0.3 eV, corresponding to 3600 K and could therefore behave as a topological insulator up to high temperatures. Using experimentally realized STIs, it has been expected that novel spin electronic devices can be realized [17, 18, 23]. However there has been a major difficulty to achieve electronic transport experiments in the regime where conduction is dominated by surface states (topological transport regime or topological insulator regime). In particular for Bi_2Se_3 , typically as-grown single crystals contain thermodynamically stable Se vacancies which donate free electrons [24]. Thus as can be seen in Figure 1.5b (white dashed line), the Fermi level of typical Bi_2Se_3 is not located inside the bulk gap, but in the conduction band. Due to high n -type doping, metallic bulk conduction dominates electronic transport in Bi_2Se_3 and makes it difficult to observe the novel properties of surface states [24].

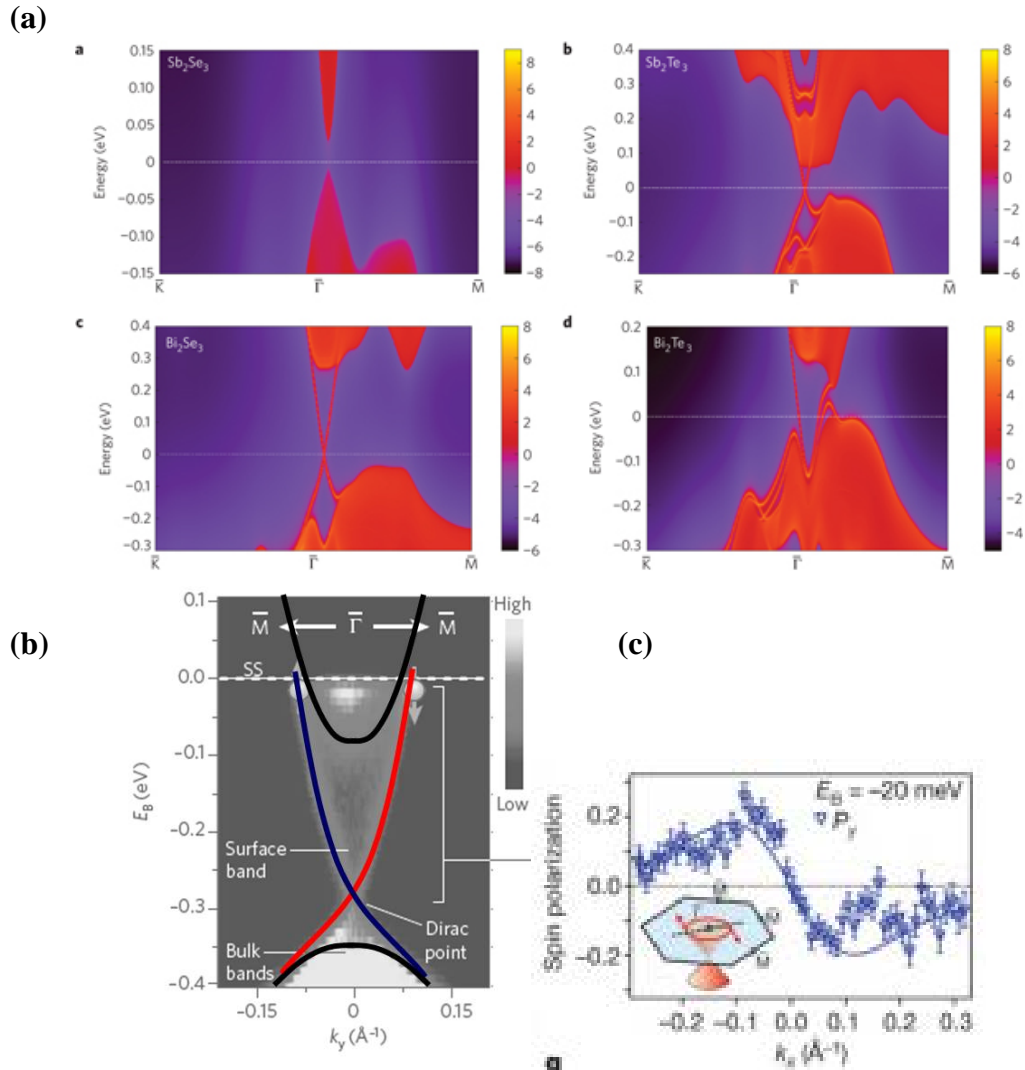


Figure 1.5 Surface band structure of representative 3D topological insulators. (a) Theoretically predicted band structure for Sb_2Se_3 (upper left), Sb_2Te_3 (upper right), Bi_2Se_3 (lower left), and Bi_2Te_3 (lower right) -Figure reproduced from Ref. [2] (b) Angle-resolved photoemission of Bi_2Se_3 showing bulk conduction and valence bands (black solid) and surface band (blue and red solid) -Figure reproduced from Ref. [21, 22]) (c) Spin polarization in Bi_2Se_3 along k_x direction-Figure reproduced from Ref. [15]

A number of strategies to reduce the contribution of bulk conduction in bismuth based STIs has been developed. The first method is to substitute bismuth with electron acceptor dopants to reduce bulk carrier density. In Ref. [15] and Ref. [25] the authors

showed that substitution of Bi to Ca or Sb leads to significant reduction of Fermi level as well as the metallic surface states survives upon chemical doping because of topological protection robustness. The second method is to fabricate very thin STI layers [26]. As I will show in the Chapter 3, this is experimentally feasible owing to the 2D layered crystal structure of Bi based STI compounds [2]. The advantage of fabricating thin layers is two-folded. Firstly, the effectively 2D thin layer has much higher surface/bulk ratio. Secondly, one can use a conventional dielectric gate to tune charge carrier density and hence the Fermi level. Electronic transport experiments on thin Ca and Sb doped Bi_2Se_3 films have been reported [25, 27]. In this thesis I developed novel *p*-type doping schemes, namely charge transfer doping and electrolyte gating, and combined with micro fabrication of Bi_2Se_3 , to achieve the topological insulator regime.

1.3 Outline of the thesis

This thesis is focused on the fundamental electronic transport properties of a representative 3D topological insulator, Bi_2Se_3 , and there are three main subjects: the scattering of charge carriers by charged impurities (Chapter 4), electron-acoustic phonon scattering (Chapter 5), and coupled/decoupled coherent transport on the surface of thin films of Bi_2Se_3 (Chapter 6). From each subject I draw clear conclusions implying surface quality of currently grown samples. A brief introduction on the charge transport in semi-classical Boltzmann transport regime as well as charge inhomogeneity dominant regime in bulk insulating 3D topological insulators is given in Chapter 2. The experimental methods, including device fabrication, novel doping methods that are used to achieve TI regime, and experimental setup are presented in details in Chapter 3. Chapter 4 discusses the first experiments to directly probe fundamental electronic transport properties of bulk

insulating Bi_2Se_3 in the charged impurity limited transport regime, and minimum conductivity physics in Dirac electronic system in the presence of charged inhomogeneity introduced in Chapter 2, which is first developed for explaining charge transport in graphene, is used to understand the observation. The results of Chapter 4 are published in *Nature Phys.* **8** 460 (2012) (Ref.[28]). Chapter 5 focuses on the electron-phonon coupling strength on the surface of Bi_2Se_3 . The temperature dependence of the carrier density is examined to identify region of Fermi level where surface dominant conduction even at room temperature is possible. Temperature dependent resistivity in this regime is measured and compared to theoretical calculation to determine the strength of the deformation potential. The results of Chapter 5 are published in *Phys. Rev. Lett.* **109** 166801 (2012) (Ref. [29]). Moving beyond the semi-classical Boltzmann transport in Chapter 4 and 5, Chapter 6 covers phase coherent transport in Bi_2Se_3 , as it is investigated by measuring weak anti-localization (WAL) phenomena at low temperature. I first introduce WAL in TIs in multichannel regime and finite size effects that occur in ultra-thin films of TIs. Experimental observation of WALs is presented for samples with different thicknesses and the results are interpreted in terms of interplay between phase coherence time, inter surface tunneling time, and disorder strength. The results of Chapter 6 are available in a preprint form in *arXiv:1212.2665* (2012). Finally, the thesis is summarized in Chapter 7 with the outlook for future works.

Chapter 2 Charge transport in gapless Dirac surface states

Generic Dirac band dispersion refers to electronic band possessing linear energy vs. momentum relation (see Fig. 1.4) where the Fermi velocity is defined by $v_F = \frac{1}{\hbar} dE / dk$. Although significant bulk conduction dominates electronic transport in as-fabricated Bi_2Se_3 devices, transport in TI regime can be achieved by methods used in this thesis (Chapter 3) [28]. Typically micromechanically exfoliated Bi_2Se_3 is transferred to 300 nm thick SiO_2 on Si substrate which, along with novel p -type doping methods used in this thesis, provides a convenient way to continuously tune Fermi level through the Dirac point. In the following chapter (Chapter 4) I examine how electronic conductivity changes when the Fermi level moves from n - to p - type conduction. Here I introduce the theoretical framework to understand the transport experiments. I discuss the semi-classical Boltzmann transport theory of a two-dimensional Dirac metal with disorder modeled by a random Coulomb potential representing charged impurities, a model originally developed in the context of graphene in Refs. [30, 31]. The model predicts the functional dependence of conductivity on carrier density in TI surface states and the existence of the finite minimum conductivity near Dirac point.

2.1 Transport theory of surface charge transport in Dirac system

Before discussing charge transport in Bi_2Se_3 surface states, it is worth mentioning another famous Dirac system, i.e., graphene which is extensively studied both experimentally and theoretically. Although Dirac band of graphene stems from conventional band theory irrelevant to topological invariant, the general theory of

transport in 2D sheet of graphene can be directly applied to 2D surface states of TI as well. Figure 2.1 shows the most common charge transport experiment done in graphene where longitudinal conductivity and transverse Hall carrier density are measured as functions of back gate voltage. Most notable features that are also expected for TI surface state are as follows. Upon carrier density tuning by global back gate voltage, (1) σ and n_H show ambipolar conduction with well-defined p - and n - regions, (2) $|n_H|$ shows a minimum value (n^*) for p - and n - conduction, (3) σ shows a roughly linear carrier density dependence for $n^* < n$, and (4) a minimum conductivity σ_{\min} near charge neutrality is observed.

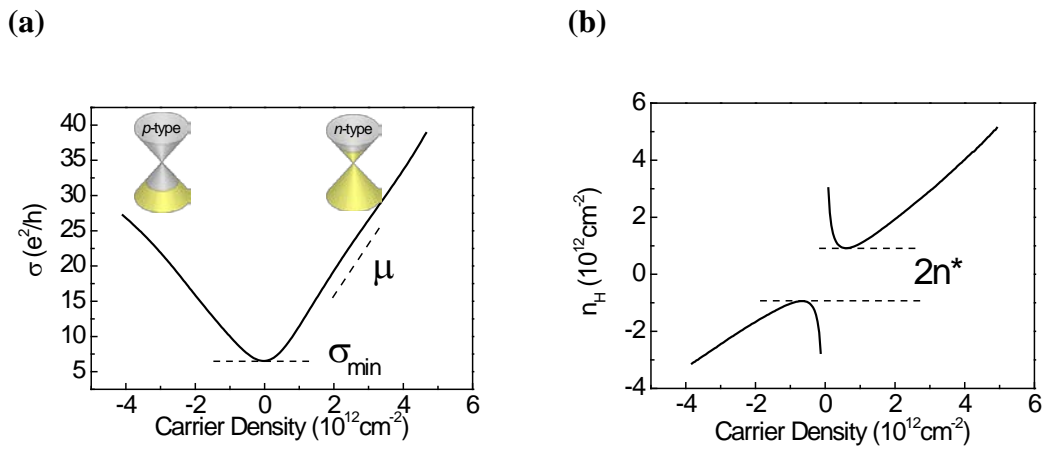


Figure 2.1 Charge transport in graphene on 300 nm SiO₂ (a) Longitudinal conductivity σ vs. back gate induced carrier density. (b) Hall carrier density n_H vs. back gate induced carrier density.

The features (2) and (4) will be discussed in the next section. I first discuss the linear σ vs. n . Charged impurity scattering has been widely studied in 2D electron systems (2DESs) especially in the context of understanding the transport properties of MOSFETs. Although Bi₂Se₃ and graphene have massless Dirac fermions as its charge carriers, the charge carriers can still be scattered by the Coulomb potential of charged impurities as in conventional 2D electron gases and the charged impurity scattering is

dominant at low carrier density. In Boltzmann transport theory the semi-classical diffusive conductivity of a linear Dirac band (both for graphene and TI surface states) is given by [32-36]

$$\sigma = \frac{g_s g_v e^2}{h} \frac{E_F \tau}{2\hbar}, \quad (2.1)$$

where g_s, g_v are the spin and valley degeneracy factors ($g_s = g_v = 2$, for graphene and $g_s = g_v = 1$ for Bi_2Se_3) and the scattering time τ at temperature $T = 0$ is given by [33, 35]

$$\frac{\hbar}{\tau(k)} = \frac{n_{\text{imp}}}{4\pi} \int dk' \left[\frac{V(|k-k'|)}{\varepsilon(|k-k'|)} \right]^2 [1 - \cos(\theta)][1 + \cos(\theta)] \delta(E_k - E_{k'}), \quad (2.2)$$

where n_{imp} is the two-dimensional density of charged impurities and $V(q) = 2\pi e^{-qd} e^2 / (\kappa q)$ is the Fourier transform of bare Coulomb potential at the transfer momentum q :

$$q = |k - k'| = 2k_F \sin(\theta/2), \quad (2.3)$$

where d is the impurity-graphene distance (assumed to be ~ 1 nm for impurities near the SiO_2 surface) and κ is the effective dielectric constant of the surrounding media. Eqn. 2.2 contains two angular dependences, i.e, $1 - \cos(\theta)$ and $1 + \cos(\theta)$. The former accounts for forward momentum scattering and the latter stems from spin overlap of initial final states, which suppresses backscattering.

Using the functional form [33] of $\varepsilon(|k-k'|)$ from the random phase approximation (RPA) to evaluate the integral in Eqn. 2.2, a recent theoretical work predicts the conductivity of the form [35]

$$\sigma(n) \sim C \left| \frac{n}{n_{\text{imp}}} \right| [e^2/h] \text{ for } n > n^*, \quad (2.4)$$

where n is the carrier density, C is a constant which depends on the Wigner-Seitz radius r_s , and n^* is identified as the residual carrier density in electron and hole puddles. This result explains the linear dependence of conductivity on carrier density at high carrier density [35]. For clean samples the charged impurity scattering is weak at high carrier density. Although charged impurity scattering is dominant over a wide range of gate voltage, at high gate voltage the n -independent short-range scattering, in addition to charged impurity scattering, is needed to explain the deviation from the linear behavior [30-32]. The difference between short-range scattering and Coulomb scattering can be easily explained by Boltzmann transport theory discussed above. Coulomb potential $V(q) \propto q^{-1}$ and short-range potential is independent of q . The integral in Eqn 2.2 is proportional to k_F^{-1} and k_F , respectively, for Coulomb potential and short-range potential. With $E_F \propto k_F$, conductivity $\sigma \propto k_F^2 \propto n$ for Coulomb potential and σ is independent of n for short-range scattering. The above discussion only considers linear Dirac band which is a good approximation in graphene over a wide range of carrier density [35, 36]. However, the range of carrier density in Bi_2Se_3 where linear approximation is valid is somewhat limited since the general surface band structure also includes higher order terms. Considering up to second order correction the effective Hamiltonian describing the surface states of topological insulators can be written in the form

$$H_o = Dk^2 + A\sigma \cdot k \quad (2.5)$$

where σ is Pauli spin matrices and it is understood that $\mathbf{k} = (k_x, k_y)$. Near $\mathbf{k} = 0$, when the spectrum is accurately described by a Dirac cone, the scalar term is overwhelmed by the spin-dependent term and can be safely neglected. The scalar and spin-dependent terms in the Hamiltonian are of the same magnitude when $Dk_f = A$, corresponding to $k_f \sim 10^9 \text{ m}^{-1}$

in Bi_2Se_3 , that is, a density of 10^{14}cm^{-2} , which is higher than the realistic densities in transport experiments. Consequently, in this thesis I ignore quadratic terms.

	2DEG	Bi_2Se_3
Bare Coulomb scattering	$\sigma \sim n^2$	$\sigma \sim n$
Screened Coulomb	$\sigma \sim n$	$\sigma \sim n$
Short-range scattering	$\sigma \sim n$	$\sigma \sim \text{const.}$

Table 2.1 Summary of Boltzmann transport results in conventional 2D electron gases and surface states of topological insulators (Bi_2Se_3). Taken from Ref. [35]

2.2 Minimum conductivity and Self-consistent theory

Away from the Dirac point, the conductivity limited by charged impurity scattering is linear in the carrier density i.e. $\sigma = en\mu$ where the mobility μ is calculated from the Boltzmann transport theory (Section 2.1). However, at low carrier density, i.e. for Fermi energies near the Dirac point, this picture is expected to break down [31, 37]. The corresponding Fermi surface cannot cover the potential fluctuations generated by the charged impurities. Charged impurities not only scatter the carriers, but create fluctuations in carrier density that are larger than the average carrier density (“electron and hole puddles”) across a macroscopic sample [37] as shown in figure 2.2. The non-zero carrier density in the puddles gives rise to a minimum conductivity $\sigma_{\min} = n^* e \mu$, where n^* is the characteristic density of carriers inside the puddles (see Fig. 2.1b). In my experiments on Bi_2Se_3 I observe both these signatures of charged impurities (Chapter 4). More importantly, I measure σ_{\min} , n^* and μ as independent experimental parameters, and test the charged impurity picture by checking to see if the variation of σ_{\min} and n^* with μ is consistent with theoretical expectations.

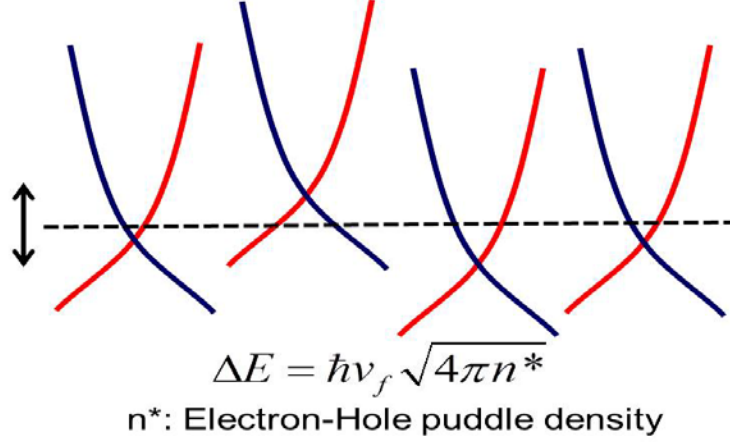


Figure 2.2 Potential fluctuation and electron-hole puddle formation near Dirac point.

The carrier density induced by the bare Coulomb impurity potential depends on the screening properties of the carriers, which itself depends on the carrier density. Thus a self-consistent theory [31] is necessary to evaluate the screened voltage fluctuations induced by charged impurities. Such a theory was originally developed to explain graphene transport near Dirac point. The self-consistent theory has three parameters: the density of charged impurities n_{imp} , the effective interaction parameter (dimensionless Wigner-Seitz radius) $r_s = e^2/\kappa_{\text{eff}}\hbar v_f$, where κ_{eff} is average dielectric constant, and the distance d of the impurities from the surface. For simplicity we ignore the weak dependence of μ on d , and assume that the surface bands have constant v_f (linear Dirac band). In this case, the self-consistent equation has the form [31, 33],

$$\frac{\mu}{\mu_0} = \frac{5}{4r_s^2} \frac{n_0}{n_{\text{imp}}} \left[\frac{\pi}{4} + \frac{3r_s}{2} - \frac{3r_s^2\pi}{8} + \left(\frac{3r_s^3}{4} - 2r_s \right) \frac{\arccos(2/r_s)}{\sqrt{r_s^2 - 4}} \right]^{-1} \quad (2.6)$$

where $\mu_0 = 1 \text{ m}^2/\text{Vs}$ and $n_0 = 10^{10} \text{ cm}^{-2}$. Following Ref. [31], n^* is calculated self-consistently. Using the Thomas-Fermi screening theory, we have

$$\frac{n^*}{n_{\text{imp}}} = \frac{r_s^2}{2} \left[-1 + e^{4r_s d \sqrt{\pi n^*}} \left(1 + 4r_s d \sqrt{\pi n^*} \right) \Gamma_0 \left(4r_s d \sqrt{\pi n^*} \right) \right] \quad (2.7)$$

where Γ_0 is the exponential integral function $\Gamma_0(x) = \int_x^\infty t^{-1} e^{-t} dt$. Given n^* and μ , we can calculate $\sigma_{\text{min}} = n^* e \mu$. In Appendix A2 I attached *Mathematica* code for the numerical calculation of n^* and σ_{min} at a given n_{imp} . Due to uncertainty in v_f and κ , I show in Chapter 4 the window of theoretical results obtained for $0.1 \text{ \AA} < d < 15 \text{ \AA}$ and $0.05 < r_s < 0.2$. The r_s range corresponds to the existing estimates in the literature of $3 < v_f < 7 \times 10^7 \text{ cm/s}$ [2, 38], and $30 < \kappa_{\text{eff}} < 60$ [24, 35] for Bi_2Se_3 surface states.

Chapter 3 Experimental methods

In this chapter, I summarize the device fabrication process and experimental setup for the measurement of charge transport properties of Bi_2Se_3 thin films. The device fabrication section includes mechanical exfoliation and identification of thin Bi_2Se_3 flakes with combined use of optical and atomic force microscopy (AFM) followed by field effect transistor (FET) device fabrication. The emphasis is put on achieving the topological insulator regime by using novel p -type doping methods (Section 3.2), which will serve as the basis for the experimental works done in the following chapters. Finally, I briefly discuss the experimental setup I used, including standard four probe AC lock-in technique and variable temperature ^4He cryostat.

3.1 Bi_2Se_3 field effect transistor fabrication

3.1.1 Mechanical exfoliation of bulk Bi_2Se_3 single crystals

As discussed in Chapter 2, transport experiment using thin film geometry is a natural route to achieve surface dominant conduction in 3D TIs. On one hand, numerous works demonstrated epitaxial growth of thin films of TIs using Van der Waals epitaxy, including Bi_2Se_3 [39], Bi_2Te_3 [40], and more recently Sb doped TI compounds such as $(\text{Bi}_x\text{Sb}_{1-x})_2\text{Te}_3$ [25]. On the other hand, most of currently known 3D TIs have common crystal structures which enable fabrication of thin films by top-down method starting from bulk crystals [2]. Bi_2Se_3 is a binary compound with rhombohedral structure. Figure 3.1a shows the crystal structure of Bi_2Se_3 [2]. Bi and Se atoms occur in 2D layers with atoms in each layer arranged in a triangular lattice. The stacking sequence is repeated by

the layers of Se-Bi-Se-Bi-Se, called a quintuple layer (QL), whose thickness is approximately 1 nm. The adjacent QLs have two Se atoms as neighbors, which are bonded by weak Van der Waals force. Therefore, Bi_2Se_3 is much easier to be cleaved between the quintuple layers and form a thin piece by repeated cleaving. In this sense, Bi_2Se_3 bulk crystal which can be prepared using macroscopic techniques is naturally structured at the nanometer scale in two dimensions.

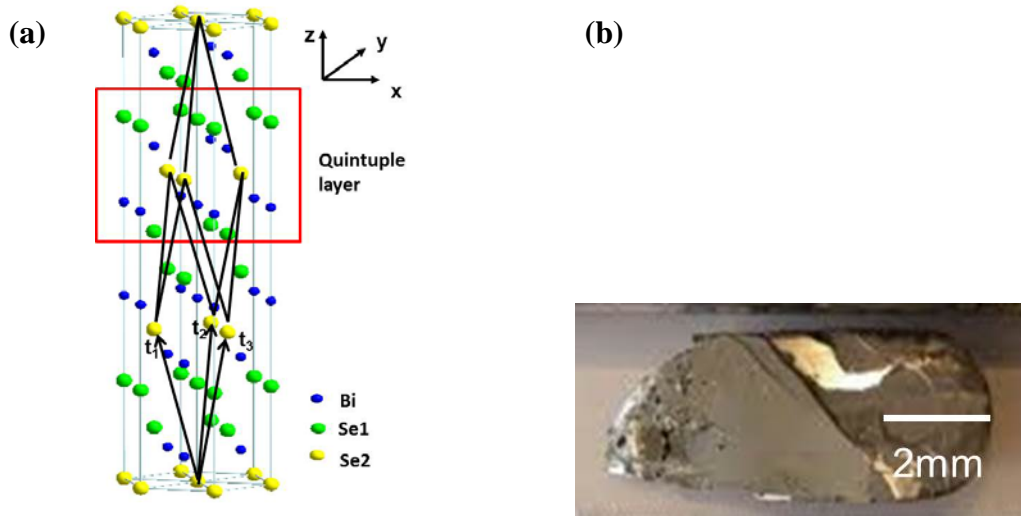


Figure 3.1 (a) Crystal structure of Bi_2Se_3 illustrating the unit cell and lattice vectors (black) and the quintuple layer (QL) unit (red). Picture from Ref. [2] (b) Bulk Bi_2Se_3 grown by binary flux method (Prof. Johnpierre Paglione group at University of Maryland [24])

For making ‘nano-patches’ of Bi_2Se_3 , I used a well-known technique for exfoliating thin single crystals using an ordinary Scotch tape. Pioneered by Geim and Novoselov on the study of graphene [41], a single sheet of carbon atoms constituting bulk graphite, mechanical exfoliation of single crystals using Scotch tape has been successfully applied on other 2D layered materials such as boron nitride (BN) [42], molybdenum disulfide (MoS_2) [43], tungsten disulfide (WS_2) [44], and 3D topological insulators [27-29].

Figure 3.1b shows Bi_2Se_3 single crystal that is grown by Paul Syers in Prof. Johnpierre Paglione group in University of Maryland. The details of the single crystals are given in Ref. [24], where the authors developed a growth technique to reduce bulk n-type doping, achieving carrier density $n \sim 10^{17} \text{ cm}^{-3}$ and bulk resistivity exceeding $2 \text{ m}\Omega \text{ cm}$ at room temperature. The crystal is mechanically exfoliated using a Scotch tape. The process of exfoliation is repeated until the tape is covered with flakes of Bi_2Se_3 . The tape containing thin layers of freshly exposed Bi_2Se_3 crystals is then pressed onto SiO_2 on degenerately doped Si substrates. Van der Waals force between the substrate and Bi_2Se_3 flakes micro-mechanically exfoliate the crystals promoting possibility of transferring even thinner flakes on the surface of SiO_2 .

After the transfer step, SiO_2/Si substrates are examined under optical microscopes (Fig. 3.2). The basic principle is that as the crystal becomes thin, visible light can transmit through the sample resulting in optical contrast change due to interference between the light that is multiply reflected inside the oxide layer. The 300 nm-thick SiO_2 enhances the interference of visible light and provides good optical contrast for thin films on it [41]. The advantage of 300 nm-thick SiO_2 is well known from extensive graphene research, but the same thickness of SiO_2 also provide good optical contrast for finding thin Bi_2Se_3 flakes. Moreover, it was found that covering the surface with 300 nm PMMA layer further enhances optical contrast for identifying thin Bi_2Se_3 flakes, the principle of which is likely the same as using SiO_2 under the sample.

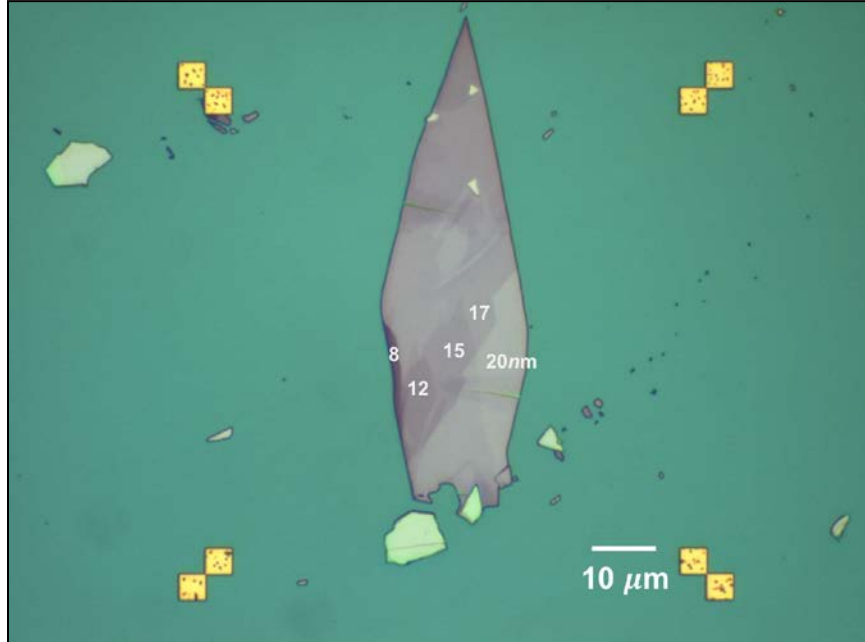


Figure 3.2 Optical image of a thin Bi_2Se_3 flake dispersed on $\text{SiO}_2/\text{doped-Si}$ substrate. Thicknesses indicated are confirmed with AFM topography measurements.

Figure 3.2 shows a typical optical micrograph of thin Bi_2Se_3 on SiO_2 surface covered with PMMA e-beam resist layer. Most of flakes dispersed on SiO_2 have thicknesses > 100 nm whose surfaces are highly reflective under visible light. As the thickness becomes < 20 nm, the films become transparent and one can identify these films based on optical contrast change. After optical identification, the sample location is recorded and transferred to the AFM stage, where the thickness is more precisely and accurately measured. Figure 3.3 shows the comparison of optical and AFM images of a few QL Bi_2Se_3 . It was found from AFM topography measurements that optical contrast difference provides a good enough resolution for identifying step height of one or two QLs. See figure 3.2 and 3.3 for contrast change and corresponding height differences. Moreover, the surface of as-exfoliated Bi_2Se_3 is nearly atomically flat over the area of a few μm^2 , indicating highly single crystal nature of the starting material.

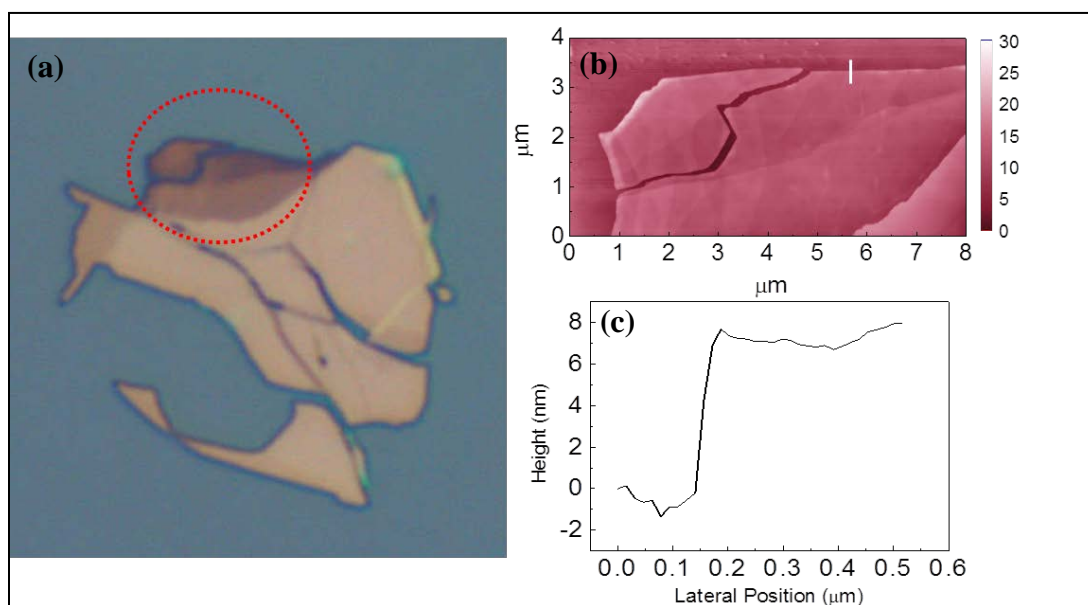


Figure 3.3 (a) Optical and (b) Atomic Force Microscopy of a few quintuple layer Bi_2Se_3 flake. (c) Height profile along the white vertical line indicated in (b).

3.1.2 Field effect transistor fabrication process

After thin film identification by combined use of optical microscopy and AFM measurements, field effect transistors are made using conventional electron-beam lithography. The process flow, detailed recipes, and optical inspections of in-line products are summarized in Appendix A. The fabrication process starts with alignment marker deposition near the target thin Bi_2Se_3 flake as follows. Alignment markers act as reference points for further processes. Substrates with Bi_2Se_3 samples are spin-coated with two-layer e-beam resist, which consists of a bottom layer of MMA/MAA copolymer (MMA EL11, MicroChem Corp.) spun at 4000 rpm for 50 seconds and a top layer of poly(methyl methacrylate) resist (950 PMMA A4, MicroChem Corp.) spun at 6000 rpm for 50 seconds. The MMA layer provide undercut for easy lift-off while PMMA has good definition of patterns under electron-beam exposure.

The relative position of each thin film is roughly measured relative to some large features (a corner of the substrate or a cross written by electron-beam lithography) using an optical microscope equipped with digital coordinate readout. At the same time, optical images of the area around the sample including thick Bi_2Se_3 flakes are taken, which serve as reference objects for accurate alignment. The sample is then inserted into a scanning electron microscope (FEI XL30). Based on the relative position and the large feature visible under SEM, the substrate is moved by the SEM mechanical stage. A pattern of alignment markers is written using the Nanometer Pattern Generation System (NPGS) software control. The sample is then removed from the SEM and the resist is developed in PMMA and copolymer resist developer (IPA/MIBK 3:1, MicroChem Corp.) for 35 seconds.

For the metallization, I mainly used a thermal evaporation method. The basic principle of operation is to thermally evaporate metals by Joule heating so that evaporated materials deposit on the surface of the sample. The process is normally done under high vacuum conditions lower than a few 10^{-6} Torr to ensure that the mean free path of evaporated material exceeds distance between the source and the sample. I used Au for both align markers and electrodes. However, Au adheres poorly on the oxide surfaces, and thin layer of Cr or Ti under Au layer is normally deposited to enhance adhesion. In the align marker deposition, 5/50 nm of Cr/Au metal is deposited. The resultant sample covered with Cr/Au is then dipped in acetone to remove the resist masks. In this “lift off” process, as the resists dissolve in acetone, the metal layer covering the non-developed PMMA/MMA resist masks is “lifted off” the substrate and only metals within the desired patterned areas remain on the surface.

As-exfoliated Bi_2Se_3 flakes have irregular shapes. For accurate determination of the geometric factor relating the measured resistance to the resistivity, the flakes are etched into regular Hall bar geometry (see Appendix A). Etch masks are prepared by similar electron-beam lithography and resist developing techniques described above except that only PMMA is used as the resist to achieve better resolution. The typical Hall bar consists of channel width of 2 μm and length exceeding 4 μm . The voltage probe arms are designed to have width less than 1 μm . This ensures that little current flows through the metal voltage probes, and defines a precise aspect ratio of the conducting path. The resultant pattern is transferred to a dry etching system (Technics PE-IIA), where the non-masked area is removed by Ar plasma at a pressure of ≈ 70 mTorr. After the etching process the resist mask is removed in acetone.

The final process is the deposition of metal electrodes for providing electrical connection to the measurement instruments. The sample, spin coated with MMA/PMMA double layer, is again inserted into the SEM for patterning of the desired metal electrode pattern to contact Bi_2Se_3 . It was found that metallization with mere thermal deposition does not form a good ohmic contacts. I resolved this problem by briefly dry etching the contact area right before the thermal deposition of metals as follows. The sample with the developed resist pattern defining the electrodes is loaded in the dry etching system, and a brief (<10 s) surface treatment with N_2 or Ar plasma was done. The plasma treatment removes surface oxides or residues of resists on the contact area, while the patterned resist act as physical mask keeping the other areas intact. By limiting etching time less than 10 seconds, I verified that about 600nm thick PMMA/MMA resist is not etched significantly and provide good enough resolution. The sample was then immediately

transferred to the thermal evaporator and the metal deposition was done similar to the process of alignment marker deposition. Liftoff was accomplished by immersing substrates in acetone for 2 hours.

3.2 Novel *p*-type doping methods for achieving topological transport regime

As discussed in the Chapter 1, reducing unintentional doping in TIs is of central importance in realizing surface-dominant conduction. As prepared Bi_2Se_3 is observed to be *n*-type due to Se vacancies [24]. Moreover, I find that mechanically exfoliated thin Bi_2Se_3 on SiO_2/Si is invariably highly *n*-doped with sheet charge densities $> 10^{13} \text{ cm}^{-2}$, much greater than expected considering the bulk charge density ($\approx 10^{17} \text{ cm}^{-3}$) in the low-doped starting material, suggesting additional doping is induced by mechanical cleavage, reaction with ambient species, or substrate interaction [27]. In order to remove this doping, I have employed two types of *p*-type doping schemes on mechanically-exfoliated thin Bi_2Se_3 field-effect transistors [28]: (1) chemical doping with 2,3,5,6-tetrafluoro-7,7,8,8-tetracyanoquinodimethane (F4TCNQ) or (2) electrochemical doping with a polymer electrolyte top gate. Figure 3.4 shows the schematic doping schemes and material preparation recipes for both types of methods.

3.2.1 Charge transfer doping with organic molecules

As a first method, I adopted surface charge-transfer doping which provides simple and effective method for *p*-type doping TI thin films [28]. The doping agent considered here is 2,3,5,6-tetrafluoro-7,7,8,8-tetracyanoquinodimethane (F4TCNQ). It has high electron affinity ($\approx 5.4 \text{ eV}$) and has been conventionally used as a *p*-type dopant in organic photo voltaic cells [45], or more recently in carbon nanotubes and graphene [46].

I deposited thin layer (≈ 10 nm) of F4TCNQ (Synquest Labs.) molecules by thermal evaporation (Fig. 3.4a) on the Bi_2Se_3 Hall bar devices that are fabricated as described in the previous section. The main results for p -type doping efficiency for this method will be discussed in Chapter 4.

Along with reducing initial n -type doping, addressing gate field induced band bending effect in TI thin films is also important for unambiguous analysis of surface transport. In order to address this issue, in addition to singly gated samples, I fabricated dual-gated samples based on F4TCNQ doped samples. The detailed procedure is described in Appendix A, optional processes. Briefly, about 60 nm of hydrogen silsequioxane (HSQ, XR-1541, Dow Corning) was spin coated on a F4TCNQ coated Bi_2Se_3 device and a top gate electrode was defined by electron beam lithography, metal deposition, and lift off. It was found that further fabrication on pre-doped devices increased the n -type doping level so that the carrier density was approximately $1.2 \times 10^{13} \text{ cm}^{-2}$ at zero gate voltage (see Chapter 4).

3.2.2 Polymer electrolyte gating

The second method was achieved by applying negative voltage to a polymer electrolyte. I adopted this method from previous studies for carbon nanotubes and graphene devices [47], where it has been demonstrated that carrier density can be tuned over a wide range ($>10^{13} \text{ cm}^{-2}$) exploiting the high capacitance of electrochemical double layer formed between surface of the sample and accumulated ions. LiClO_4 and polyethylene oxide (PEO) was mixed in the weight ratio 0.12:1, and the mixture was dissolved in methanol. For the application, I used a micro pipet to put a small droplet

around the device, and the electrolyte was dried at ambient condition for an hour. During the measurement, negative voltage on the order of 1 V was applied to the gate electrode near the sample (Fig 3.4b), and the devices were subsequently cooled down. For both methods of *p*-type doping, further tuning of carrier density was done by sweeping the back gate voltage at cryogenic temperature. For electrolyte-gated measurements, the samples were cooled down to 250K in less than 1 minute after applying the top gate voltage to minimize electrochemical reactions.

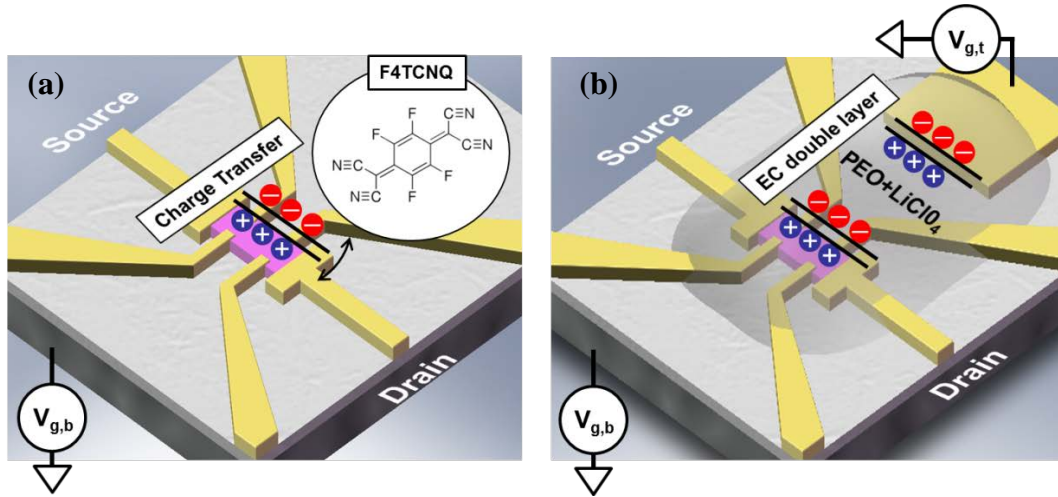


Figure 3.4 Schematics of device structure and *p*-type doping schemes. **(a)** Charge transfer doping with F4TCNQ organic molecules. **(b)** Polymer electrolyte (Polyethylene oxide : LiClO₄=1 : 0.12 by weight ratio) top gating method

3.3 Measurement setup

3.3.1 Four probe AC lock-in technique

The longitudinal and transverse (Hall) resistivities were measured by an ac setup using a lock-in amplifier (Stanford Research Systems SR830). The typical lock-in technique involves sinusoidal excitation current flowing through the device, and

measuring voltage whose frequency is locked to that of excitation signal. As shown in Figure 3.5, the lock-in amplifier outputs a sinusoid voltage signal at a near DC frequency (≈ 17 Hz) which is low compared to any frequency dependence of the sample's conductivity. A $10\text{ M}\Omega$ resistor (tolerance 0.1%) is in series with the voltage source which, combined with the 1 V output voltage, acts as a current source with rms amplitude of 100 nA. This is a very good approximation for the source current since the device typically has two probe source-drain resistance of the order of $\sim\text{k}\Omega$, which can be neglected compared to the source resistance of the current source ($10\text{ M}\Omega$). This signal is also taken as a reference signal inside the lock-in amplifier. The voltage difference from the voltage probes of the sample is measured using the lock-in differential inputs A and B. The input resistances of the lock-in is $100\text{ M}\Omega$, which is much larger compared with typical resistance of the sample and ensures that the excitation current flows only through the device thereby enabling accurate determination of sample's electrical resistivity.

The main function of a lock-in amplifier can be understood in terms of orthogonality of triangular functions. The measured voltage signal typically includes large noise signals whose frequencies are typically uncorrelated with the reference signal. A mixer inside the amplifier multiplies the measured input signal with the reference signal, and the modulated signal is integrated in time (typically 30ms). Due to orthogonality of sine or cosine functions with different frequencies, the output DC signal is becomes only proportional to the input signal whose frequency is the same as that of the reference signal. In this manner, one can recover the signal even when there are large noise components.

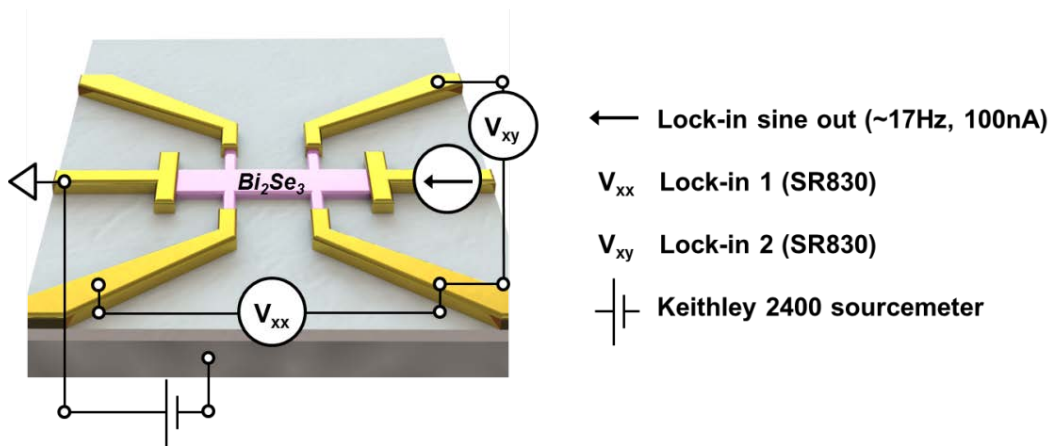


Figure 3.5 Schematic of gate-tuned longitudinal and Hall resistivity measurement setup

3.3.2 Variable temperature ^4He cryostat

In order to control environmental temperature and magnetic field, a commercial variable temperature cryostat equipped with 9 T superconducting magnet (Quantum Design, Physical Property Measurement System) was used. Figure 3.6 shows the main Dewar and the schematic cross section of the chamber near sample mounting area. The vacuum space between the outer and inner vacuum tubes contains reflective superinsulation to minimize radiative power loss into the helium bath. Liquid ^4He bath, through controlled heat exchange with vacuum sealed sample area, can initially cool sample down to ≈ 7 K, where further cooling can be done with impedance assembly. The impedance assembly enables or disables the flow of helium into the ^4He pot located at the bottom of the chamber from the Dewar. By controlling ^4He inlet flow and pumping rate in the ^4He pot, the sample area can be cooled down to ~ 1.8 K.

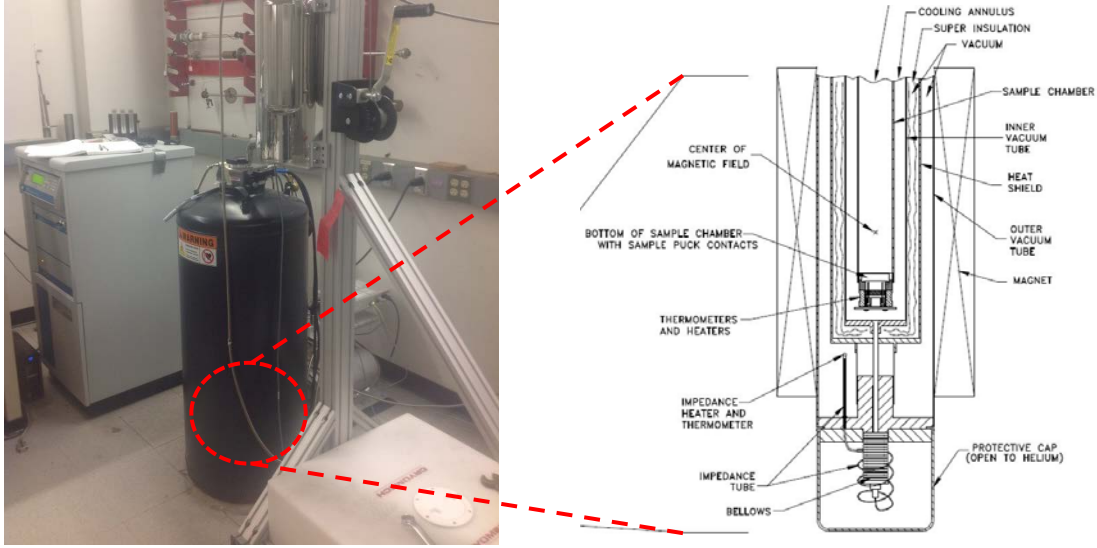


Figure 3.6 Quantum Design PPMS equipped with pulse condenser and 9T superconducting magnet.

The main probe of the PPMS provides 12 electrical connections, which are normally connected to a built-in source-measure unit. I used an external user-bridge cable and controlled the measurement using custom built LabVIEW programs. The main programs I run are as follows.

(1) The measurement of lock-in voltage (SRS830) as a function of applied gate voltage (Keithley 2400) at +1, 0, and -1 T of magnetic field. Zero field values are stored for longitudinal resistivity while transverse (Hall) voltages at these magnetic fields were anti-symmetrized to remove longitudinal voltage components.

(2) The measurement of lock-in voltage (SRS830) as a function of applied magnetic field at fixed gate voltage and temperature. Typical sweep rate of the field was set to 50 G/s.

In all measurements, the lock-in time constant was set at 30 ms, which requires at least a delay of 0.15 s for each data sampling point. At this time constant, the low-pass

filter has a cutoff frequency at 5.3Hz , which is lower than the ac reference frequency. With the help of the synchronous filters, the noise from the reference/detection frequency can be easily removed.

Chapter 4 Surface conduction of topological Dirac electrons in bulk insulating Bi_2Se_3

As the simplest case among the existing TIs, Bi_2Se_3 has single Dirac cone with Dirac point located at zero momentum (Γ point) [2, 38]. In this chapter, I demonstrate and discuss the electronic transport properties in TIs when the conduction is dominated by surfaces. In section 4.1, I show the efficiency of the p-type doping methods introduced in the chapter 3, and demonstrate the most fundamental signature of the TI surface states: ambipolar metallic electronic transport in the topological surface of an insulating bulk. I show that the surfaces of thin, low-doped Bi_2Se_3 crystals are strongly electrostatically coupled, and a gate electrode can completely remove bulk charge carriers and bring both surfaces through the Dirac point simultaneously. In section 4.2, a theory of charge disorder in a Dirac band introduced in the chapter 2 is used to explain both the magnitude and the variation with disorder strength of the minimum conductivity and the residual (puddle) carrier density. It was found from comparison of the experiment and theory that the surface transport properties of current TI samples are consistent with the Dirac electronic conduction assuming charged impurity density of order $\sim 10^{13} \text{cm}^{-2}$.

4.1 Electronic transport in the topological insulator regime

4.1.1 *p*-type doping effects near room temperature

Using the four probe lock-in techniques described in chapter 3, I confirmed the efficiency of the *p*-type doping methods developed in this work. Figure 4.1a shows Hall carrier density $n_H=1/eR_H$, where R_H is the measured Hall coefficient, at zero gate voltage and at room temperature for 15 different Bi_2Se_3 devices ranging in thickness from 5 to 17 nm (QL) with (red) or without (blue) 10 nm of F4TCNQ deposition. The n_H of as-fabricated Bi_2Se_3 devices scatters with respect to average value of $\approx 1.5 \times 10^{13} \text{ cm}^{-2}$, however, it appears that there is no correlation between n_H and thickness. This points to a surface origin for the initial *n*-type doping. For given bulk doping of the starting material ($\sim 10^{17} \text{ cm}^{-3}$), 2D density only of order $\sim 10^{11} \text{ cm}^{-2}$ of carriers for 10 nm thick Bi_2Se_3 is expected, suggesting that the high initial doping of order $\sim 10^{13} \text{ cm}^{-2}$ mostly stem from the surface of the sample, the amount of which varies from sample to sample [48]. On average, the deposition of F4TCNQ molecules results in a change of doping of $-1 \times 10^{13} \text{ cm}^{-2}$ (arrows in Fig. 4.1a); the negative sign indicates a shift toward *p*-type doping, i.e. a reduction in *n*-type doping. Moreover, the resultant change of n_H on F4TCNQ deposition is similar regardless of sample thickness, further supporting that the initial doping resides on the surface [49].

Figure 4.1b shows conductivity $\sigma(n_H)$ of a F4TCNQ-doped 12 nm device at room temperature and ambient condition. The device was exposed to air for 1 (black square), 15 (red circle), and 25 (green triangle) days. In all measurements the range of gate voltage through 300 nm SiO_2 dielectric was fixed from 0 to -20 V. The doping at zero gate voltage changes less than 10% in 15 days but shows negligible change from 15 to 25

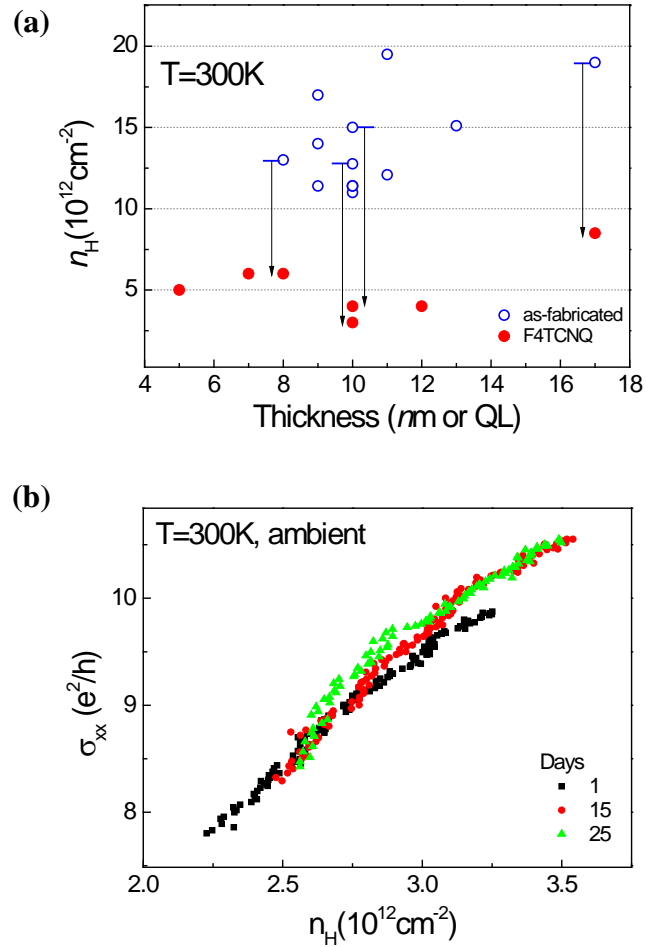


Figure 4.1 Charge transfer p-type doping with F4TCNQ. **(a)** Hall carrier density n_H at zero gate voltage and at room temperature for 15 devices with (red) or without (blue) F4TCNQ deposition ranging in thickness from 5 to 17 nm. Arrows indicate change of n_H measured in the same sample. **(b)** Conductivity σ of a F4TCNQ-doped 12 nm thick device as a function of n_H at 300 K and ambient condition. The device was exposed to air for 1 (black square), 15 (red circle), and 25 (green triangle) days.

days. I obtain the Hall mobility of $\approx 600 \text{ cm}^2/\text{Vs}$ in all measurements, which shows good thermal stability of p-type doping by F4TCNQ molecules. This is in contrast to the behavior of Bi_2Se_3 device without F4TCNQ layer as surface degradation and mobility reduction is commonly observed upon prolonged exposure to ambient [49]. Therefore, I conclude that F4TCNQ not only provides effective p-type doping but also act as stable capping layer for protecting the Bi_2Se_3 surface from degradation.

I now turn to discuss the effect of electrolyte gating. Figure 4.2 shows longitudinal resistivity ρ_{xx} (black curves) and n_H (red curves) of a 10 nm Bi_2Se_3 with polymer electrolyte on top as functions of electrolyte gate voltage measured at room temperature. Although the initial gate capacitance for the polymer electrolyte was found to be $\approx 1 \mu\text{F}/\text{cm}^2$, which is about 100 times larger than that of 300nm SiO_2 , the gate efficiency decreased rapidly as the gate voltage exceeded $\approx 0.8\text{V}$ likely due to onset of electrochemical reaction [47]. Notable hysteresis in the forward and backward voltage scans was also found whose origin is not yet known. However, I note that the curves are reproducible at given sampling rate as long as I limit the magnitude of maximum voltage less than 1V. The advantage of polymer electrolyte gating over F4TCNQ deposition is that it has wider range of carrier density tunability (over $-1.5 \times 10^{13} \text{cm}^{-2}$ in Fig 4.2) and the experimental implementation is simpler. However, I find that application of gate voltage exceeding 2V typically resulted in rapid surface damage due to onset of electrochemical reaction. Moreover, the electrolyte, right upon application on the sample, can initially n -type dope the sample. For this reason, I mainly focus on F4TCNQ-doped samples in the later chapters.

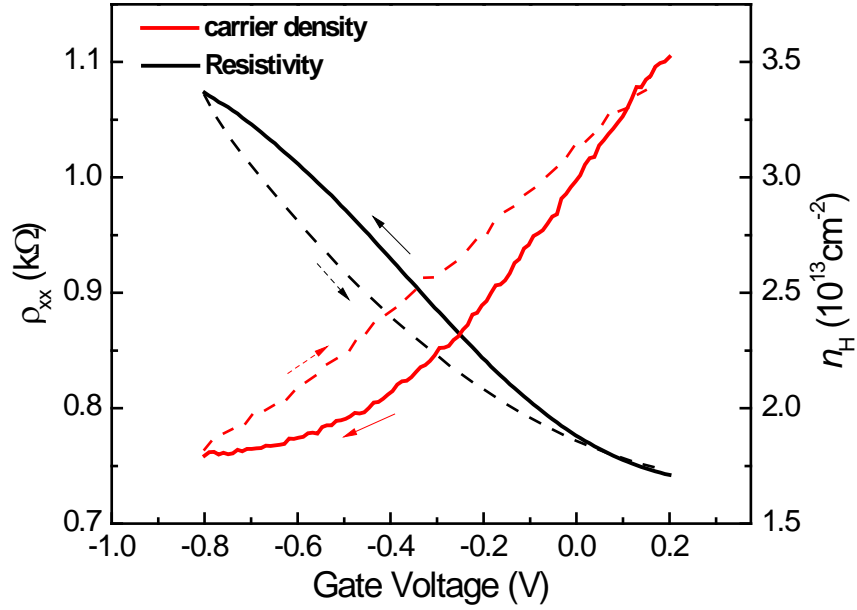


Figure 4.2 Electrolyte gating of a 10 nm Bi₂Se₃ device at 300K. Resistivity (ρ_{xx}) and sheet carrier density determined from Hall voltage (n_H) as a function of electrolyte gate voltage.

4.1.2 Gapless ambipolar field effect

The gapless Dirac dispersion relation in topological surface states implies that the gate tuned electronic conduction will show *n*-type to *p*-type transition without showing insulating behavior in between as the Fermi level moves from upper to lower part of Dirac cone. Using *p*-type doped 10 nm Bi₂Se₃ devices, I performed gate tuning experiments at cryogenic temperatures. Figure 4.3a and b show ρ_{xx} and n_H of a representative device (F4TCNQ-doped device) at various temperatures T from 2K to 50K as a function of back gate voltage V_g . $\rho_{xx}(V_g)$ shows a peak at approximately $V_{g,0} = -45$ V, and n_H changes sign at a similar V_g , diverging positively (negatively) when approaching

$V_{g,0} = -45$ V from above (below). There is no evidence of an energy gap: $\rho_{xx}(T)$ is metallic ($d\rho_{xx}/dT > 0$) and saturates at low T , and $n_H(T)$ shows little temperature dependence. The behavior is strongly reminiscent of that seen for the two-dimensional Dirac electronic system in graphene. (see Fig. 2.1) [32, 41]. Likewise, I identify the linear regions of n_H vs V_g for $V_g > -35$ V and $V_g < -60$ V as unipolar n - and p -doped regimes respectively, and the region $-35 < V_g < -60$ V as an inhomogeneous regime characterized by residual carrier density $2n^*$ (see section 4.2) where electron and hole transport are both present [37]. Therefore, the clear ambipolar field effect with no evidence of an intervening gap, along with simultaneous sign change of Hall signal, strongly suggests surface dominated conduction in the present Bi_2Se_3 devices. From 2K to 50K, I observe shift of the charge neutrality point (dashed lines) as well as reduction of capacitance in hole transport regime. This behavior, which is absent in temperature dependent transport in graphene, will be discussed in detail in chapter 5 (see also Ref. [29]). Below in this chapter I focus on the dependence of the measured ρ_{xx} and ρ_{xy} on carrier density and magnetic field at low temperature.

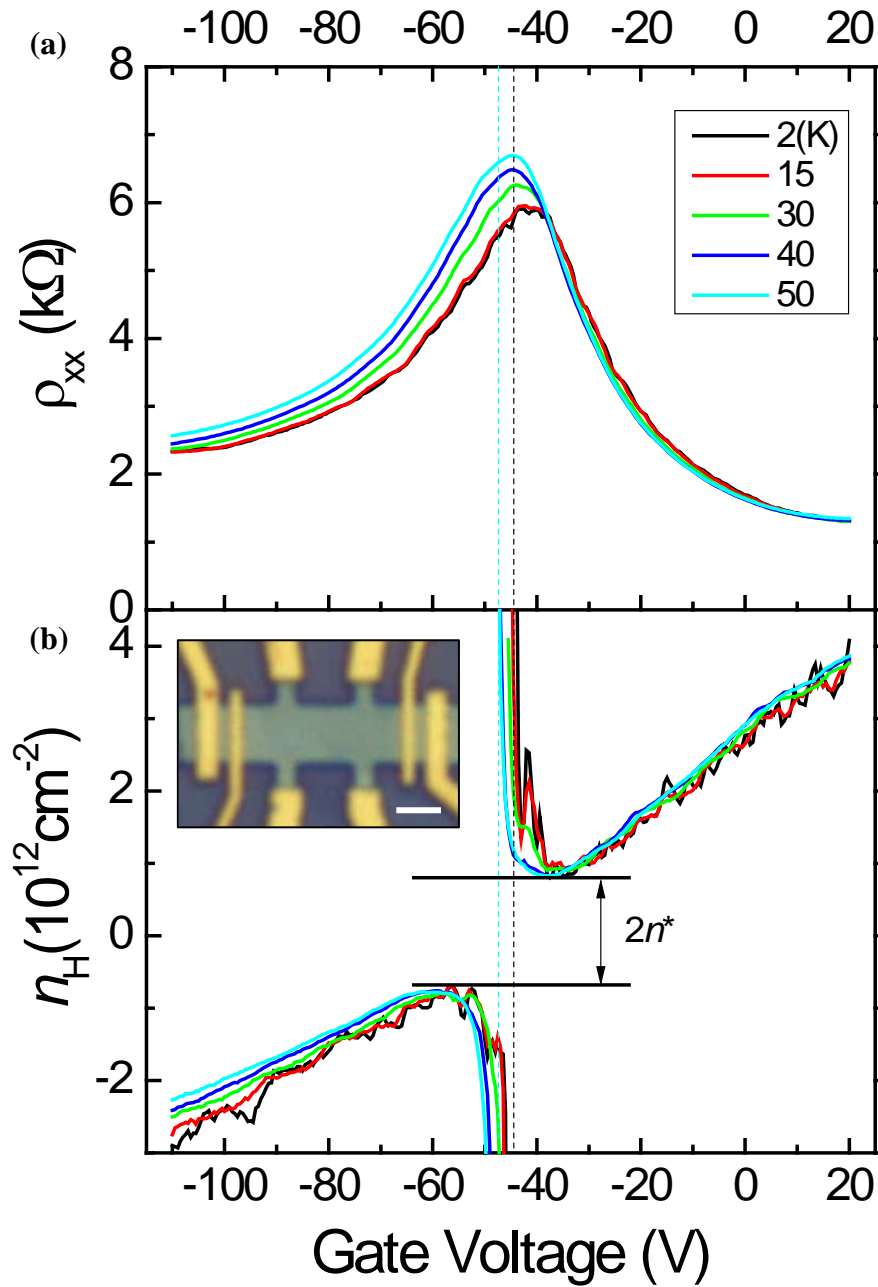


Figure 4.3 Gate tuned transport in TI regime. **(a)** Longitudinal resistivity (ρ_{xx}) and **(b)** Hall carrier density n_H of device 4 (F4TCNQ doped) as functions of back gate voltage at various temperatures from 2 K to 50 K indicated in caption. The inset shows an optical micrograph of the device. The scale bar is $2\mu\text{m}$.

4.1.3 Single band conduction in the topological transport regime

In gated semiconductor structures with non-negligible bulk doping, the gate field is screened by free carriers in the bulk, where the effective depth of gating is approximately set by the Thomas-Fermi screening length. In thin films of TIs, ignoring the side surfaces, it was not clear whether gate field through order of 10 nm thick sample is significantly screened, in which case gate electrode tunes the Fermi level of one surface preferentially, or the gate field can tune both top and bottom surfaces simultaneously [27]. Moreover, mechanically exfoliated Bi_2Se_3 crystals may have considerable in-gap impurity states so that the sample can show similar ambipolar effects if the conduction is dominated by the presence of significantly populated impurity states. Because of the geometry of the current samples, it is not possible to independently measure transport in each surface. However, these issues can be addressed by examining magneto-transport and by samples with dual gate geometry, as explained below.

I first examine the dependence of ρ_{xy} as a function of external magnetic field B to look for evidence of multi-band transport. Figure 4.4 shows the ρ_{xy} as a function of B of the device I used to show gapless ambipolar effect at various gate voltages in the unipolar n - and p -doped regimes. The ρ_{xy} in the unipolar regime is always linear over the entire range of magnetic field (± 9 T), indicating all bands contributing to the transport have similar mobility and same carrier sign. If more than one band type was significantly contributing to the conductivity, such as contributions from surface and bulk, or two surfaces with very different carrier density and mobility, then $\rho_{xy}(B)$ must be non-linear. The simple two fluid model predicts $\rho_{xy}(B)$ in the form [50],

$$\rho_{xy}(B) = \frac{(R_1\rho_1^2 + R_2\rho_2^2)B + R_1R_2(R_1 + R_2)B^3}{(\rho_1 + \rho_2)^2 + (R_1 + R_2)^2 B^2} \quad (4.1)$$

where $R_{1,2}$ and $\rho_{1,2}$ are Hall coefficient and resistivity of each band, respectively. In particular, for two bands of same carrier sign and different mobility, $\rho_{xy}(B)$ would be significantly non-linear on the scale of $B \sim 1/\mu$ where μ is the highest mobility of the two bands. If two bands of similar mobility but different carrier sign are present, $\rho_{xy}(B)$ would again be non-linear on the scale of $B \sim 1/\mu$. The presence of both bulk and surface channels in conduction indeed gave rise to non-linear $\rho_{xy}(B)$ in the previous studies [48, 51]. However, since $1/\mu \sim 7$ T for the current sample (see Figure 4.3), and $\rho_{xy}(B)$ is linear for both electron and hole type conduction up to 9 T, one can conclude that all bands contributing to conduction have similar mobility and switch carrier sign at the same gate voltage, as expected for the two surface bands with similar carrier density and mobility, but not if bulk or impurity bands significantly contribute to the conduction. One can also rule out conduction due to bulk impurity bands due to their extremely low carrier mobility (< 10 cm²/Vs, Ref. [27]), whereas the measured carrier mobility ($>10^3$ cm²/Vs), is much higher. The measured linear ambipolar Hall effect with carrier mobility of $>10^3$ cm²/Vs is therefore a strong indication that conduction in current samples is dominated by the surface states.

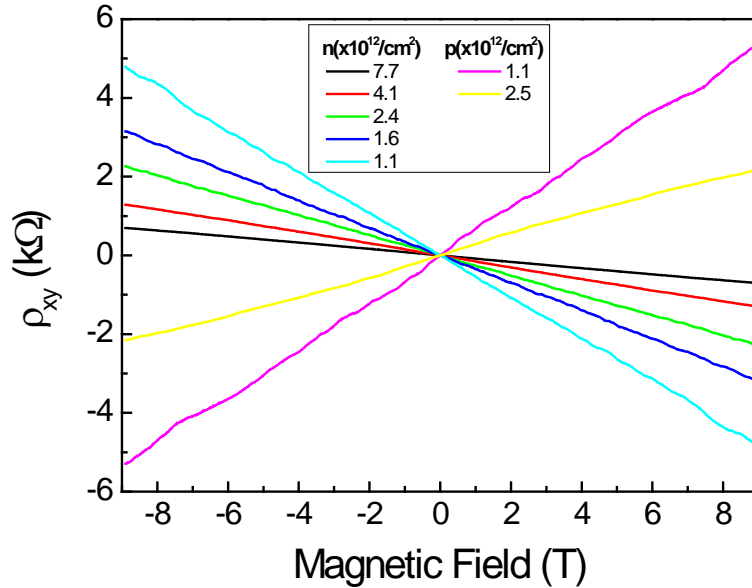


Figure 4.4 Single band conduction in TI regime. Hall resistivity ρ_{xy} of the F4TCNQ-doped 10 nm Bi_2Se_3 device as a function of magnetic field B at a temperature of 2 K at different carrier densities tuned by the back gate electrode.

4.1.4 Absence of band bending effect : the role of bulk capacitance

I note that a previous work on singly-gated Bi_2Se_3 of similar thickness of 10 nm but heavily (0.5%) Ca-doped device [27] also showed a superficially similar resistivity peak, interpreted there as the transition from bulk to surface conduction and no region of unipolar p -type Hall effect was observed. The authors concluded that significant band-bending in these highly-doped crystals led to very different carrier densities on either side of the device as well as an effective reduction of the bulk gap. On the other hand, the linearity of $\rho_{xy}(B)$ in my devices already indicates that the top and bottom surfaces cannot have widely different carrier densities [28]. In order to corroborate our picture of surface dominant conduction, I fabricated an additional top gate on an F4TCNQ-doped device, using hydrogen silsequioxane (HSQ) as a top-gate dielectric. The detailed process and recipes for top gate fabrication can be found in Chapter 3 and Appendix A. Figure 4.5a

shows schematic structure of dual gating geometry. From n_H vs. gate voltage measurements, bottom and top gate capacitance were determined to be ≈ 11 nF/cm² and ≈ 33 nF/cm², respectively, which are reasonable considering the dielectric constants of SiO₂ ($\kappa \approx 3.9$) and HSQ ($\kappa \approx 3$). Because of the capacitance difference, I converted gate voltage to displacement field of the back gate D_{bg} and top gate D_{tg} to directly compare the effect of the two gate electrodes on the transport properties.

Figure 4.5b shows ρ_{xx} of the dual-gated Bi₂Se₃ device as a function of D_{tg} and D_{bg} surfaces. The data are presented as a polar plot of normalized resistivity (ρ_{xx}/ρ_{max}) of the device as a function of total magnitude of displacement field $D_{total}=|D_{bg} + D_{tg}|$ and asymmetry factor defined by $\alpha = (4/\pi) \tan^{-1}[(D_{tg} - D_{bg})/D_{total}]$. As examples, the asymmetry factors $\alpha = -1, 0, 1$ correspond to $D_{total} = D_{tg}$, $D_{tg} = D_{bg} = 1/2 D_{total}$, and $D_{total} = D_{bg}$, respectively at a given D_{total} . I find that the measured resistivity depends only on the total displacement field, proportional to the total charge density in the Bi₂Se₃ slab, but not on the symmetry between D_{bg} and D_{tg} . I conclude from the observed azimuthal symmetry that both surfaces are gated simultaneously with either gate, and their chemical potential lies at the same level. If the gates acted independently on top and bottom surfaces, the maximum resistivity peak associated with the transition from n - to p -doping in each surface should broaden or split with increasing asymmetry; no such effect is observed. Remarkably, I find that simultaneous gating can be achieved even with a single gate electrode (α approaching 1 or -1). These results show that, the surfaces of thin (≈ 10 nm), low bulk doped Bi₂Se₃ ($\approx 10^{17}$ /cm³) crystals are strongly electrostatically coupled, and a gate electrode can completely remove bulk charge carriers and bring both surfaces through the Dirac point simultaneously. As discussed in detail below, I ascribe this effect

to (1) the strong electrostatic coupling of the surfaces due to the large intersurface capacitance provided by the thin, lightly doped Bi₂Se₃, which has a high relative dielectric constant $\kappa \approx 100$; and (2) the small density of states of the Dirac surface. The net result is that the electrostatic intersurface capacitance exceeds the quantum capacitance of each surface, in which case the two surface potentials become locked together.

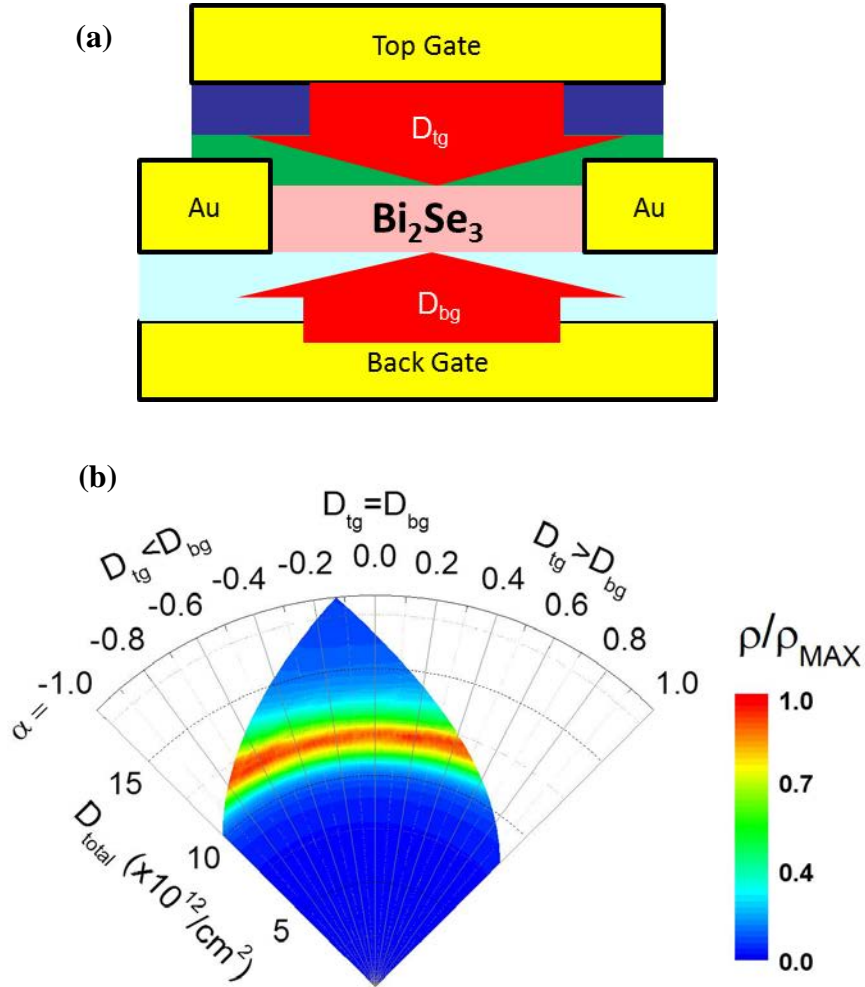


Figure 4.5 Dual gate transport in TI regime. **(a)** Schematic of dual dielectric gating on a F4TCNQ doped Bi_2Se_3 device. **(b)** Polar plot of the normalized longitudinal resistivity ρ of a dual gated Bi_2Se_3 thin film device as a function of total magnitude of displacement field (D_{total}) and gating asymmetry factor α (defined in the text).

In order to explain possible origin of observed simultaneous gating of topological surfaces, I modeled the electrostatic response of the two topological surfaces to back and top gate voltage by the effective capacitor network as shown in the figure 4.6a, which includes the electrostatic gate capacitances $C_{\text{g,t}}$ and $C_{\text{g,b}}$ to top and bottom surfaces respectively, and the quantum capacitances $C_{\text{q,t}}$ and $C_{\text{q,b}}$ of top and bottom surfaces. The quantum capacitance reflects the change in charge required to change the Fermi energy

E_F in a material. For small changes in Fermi energy, C_q is often approximated by $e^2(dn/dE_F)$, where e is the elementary charge and dn/dE_F is the density of electronic states $D(E)$. Since $D(E)$ varies significantly in a 2D Dirac material such as the topological surface state, I will use the full quantum capacitance $C_q = e^2(n/E_F)$ where n is the carrier density. Note that the two surfaces are coupled by an interlayer capacitance C_{il} , which originates from the bulk part of the Bi_2Se_3 thin film. For the dual-gated device, I measure $C_{g,b} = 11 \text{ nF/cm}^2$, $C_{g,t} = 33 \text{ nF/cm}^2$, and estimate C_{il} to be order of $\sim 10 \text{ uF/cm}^2$ considering nominal thickness ($\approx 10 \text{ nm}$) and dielectric constant ($\kappa \approx 100$ [24]) of Bi_2Se_3 films. For electrolyte-gated devices, I measure a capacitance to the back gate at cryogenic temperatures which is greater than 11 nF/cm^2 ; I assume that the excess capacitance is due to a high polarizability of the polymer electrolyte which provides additional coupling of the back gate to the top surface about 16 nF/cm^2 . The near-equivalence of the capacitance of the back gate to top and bottom surfaces in electrolyte-gated devices further enhances equilibration of charge on top and bottom surfaces above what would be expected in the analysis below.

I assume a linear dispersion relation for surface states in Bi_2Se_3 which is valid up to $n \approx 5 \times 10^{13} / \text{cm}^2$ per surface [35], thus considering degeneracy of one, $E_{F,b(t)} = 2\hbar v_F (\pi n_{b(t)})^{1/2}$ where \hbar is Planck's constant and $v_F = 3 \times 10^5 \text{ m/s}$ to $7 \times 10^5 \text{ m/s}$ is the Fermi velocity in Bi_2Se_3 , representing roughly the average Fermi velocity for the conduction cone for energies below the bulk conduction band [38]. I use the experimentally observed $n_0 \approx 12 \times 10^{12} / \text{cm}^2$ at zero displacement field as a reference point; equal carrier density ($n_t = n_b = 6 \times 10^{12} / \text{cm}^2$) at this gate voltage (see Fig. 4.5b) was assumed. The carrier density of each surface can be expressed as

$$n_{b(t)} = n_{bg(tg)} \mp n_{il} \quad (4.2)$$

where $n_{bg(tg)} = C_{g,b(t)}(eV_g - E_{Fb(t)})/e^2$, $n_{il} = C_{il}(E_{ft} - E_{fb})/e^2$, and V_g is the applied back gate voltage.

Figure 4.6b shows calculated carrier density for bottom and top surface carrier densities as functions of total magnitude of applied field for symmetric ($\alpha = 0$, dashed) and highly asymmetric ($\alpha = -0.5$) gating schemes assuming $C_{g,b} = 11 \text{ nF/cm}^2$ and $C_{g,t} = 33 \text{ nF/cm}^2$ corresponding to the dual gated Bi_2Se_3 device. I compared carrier densities for the same parameters for gate capacitances in the strong ($C_{il}/C_q \gg 1$, $C_{il} = 30 \text{ uF/cm}^2$, solid lines), intermediate ($C_{il}/C_q \sim 1$, $C_{il} = 3 \text{ uF/cm}^2$, dotted lines), and weak coupling limit ($C_{il}/C_q \ll 1$, $C_{il} = 0.1 \text{ uF/cm}^2$, dashed-dot lines). In the weak coupling limit the large difference in applied field ($D_{gb} = 3D_{gt}$ for $\alpha = -0.5$) leads to very different carrier densities on either side of the device so that a splitting of maximum resistivity at Dirac point is expected. However, the presence of large inter-surface capacitance (C_{il}) enhances the tendency to equalize the surface charge densities. As interlayer capacitance becomes comparable to quantum capacitance of Dirac surface, it dramatically reduces carrier density difference of the surfaces.

For estimated $C_{il} \approx 11 \mu\text{F/cm}^2$ of the device ($t_{\text{tot}} \approx 10 \text{ nm}$), the carrier density difference at charge neutrality $\Delta n = n_t - n_b \approx 1.2 \times 10^{12} \text{ cm}^{-2}$, which is comparable to the observed width of charge inhomogeneity $2n^*$ of the current devices (Fig. 4.3b). However, I note that the surface electronic state has some finite extent into the bulk [52], thus especially in thin film geometry, C_{il} can be significantly larger. For $C_{il} > 13 \mu\text{F/cm}^2$, Δn becomes less than $2n^*$ ($\approx 1 \times 10^{12} \text{ cm}^{-2}$), and for C_{il} exceeding $20 \mu\text{F/cm}^2$ which is

conceivable when $t_{\text{bulk}} < 5$ nm, Fermi energies of bottom and top surfaces are essentially locked together with negligible Δn . The experimental observations in the dual gated device suggest the samples approach this limit since I observed that the simultaneous gating approximation holds even when $\alpha = \pm 1$, where gating field is applied only to one of the surfaces. Since Δn is much less than the observed $2n^*$ in this limit, I conclude that n^* is dominated by local inhomogeneity in the carrier density due to disorder on each surface [53].

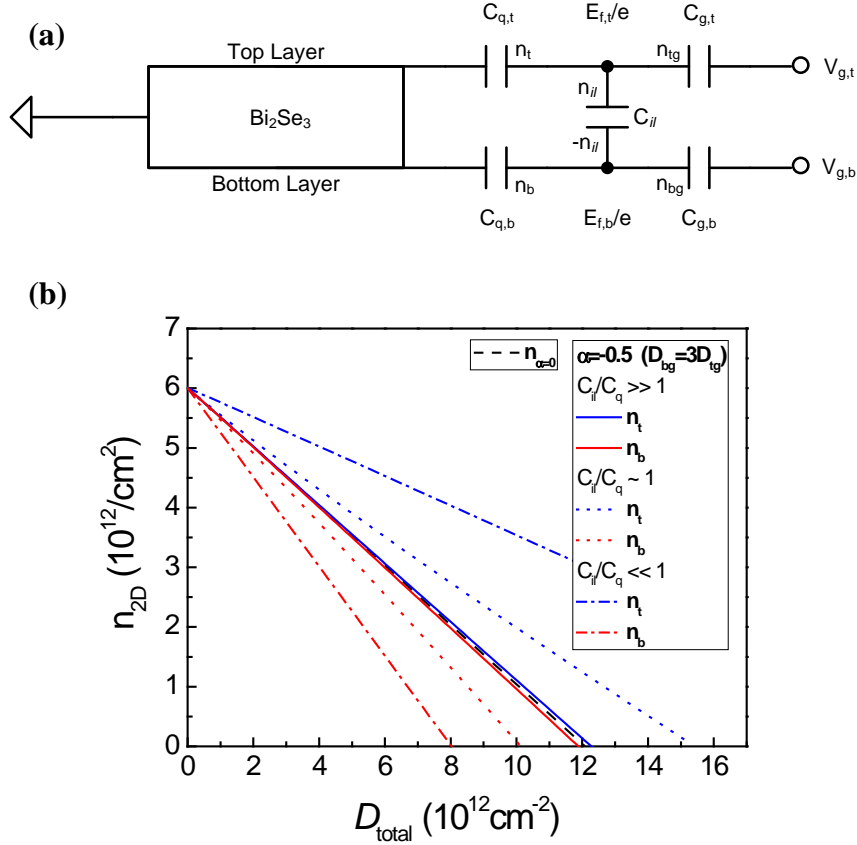


Figure 4.6 Displacement field induced surface charge density. (a) Capacitor network model of a dual gated Bi_2Se_3 thin film device. (b) Calculated charge densities for top (blue) and bottom (red) surfaces as a function of total magnitude of applied field. Dashed black line is carrier density for symmetric applied field ($\alpha=0$). The solid, dot, dashed-dot lines are charge densities calculated for highly asymmetric applied field ($\alpha=-0.5$) in the strong, intermediate, and weak interlayer coupling limits, respectively.

4.2 Charge inhomogeneity driven minimum conductivity in Dirac surface states

4.2.1 Charged-impurity limited transport in the Boltzmann transport regime

Having eliminated the possibilities of band-bending or significant contribution to the conductivity by bulk or impurity states, the current measurement probes the conductance of the simultaneously-gated ambipolar Dirac surface states. This result therefore represents the first experimental demonstration of metallic, ambipolar, gapless electronic conduction of the topological surface state in Bi_2Se_3 in the absence of bulk

carriers, the defining quality of a topological insulator. Moreover, the demonstration of nearly equal Fermi level of both surfaces on gate tuning opens an opportunity to analyze the transport of one surface only, since in this case we can reasonably approximate the conductivity of one surface as one half of the measured total conductivity.

Below, I analyze in more detail the transport properties of the topological surface state as a function of carrier density per surface n estimated from $n = (C_g/2e)(V_g - V_{g,0})$ where $V_{g,0}$ is the gate voltage at which $R_H = 0$, which corresponds closely to the gate voltage of minimum conductivity. Figure 4.7 shows (a) conductivity per layer (σ), (b) the Hall carrier density per layer ($n_{H,layer} = 1/2R_H e$), and (c) field effect mobility $\mu = \sigma/ne$ vs. carrier density per layer n . Data are shown for devices 1-3 with electrolyte gating, and devices 4-5 charge transfer doped with F4TCNQ. Several features are notable immediately in Figure 4.7 and comprise the major experimental observations in this chapter. Upon carrier density tuning, (1) σ and $n_{H,layer}$ show clear ambipolar conduction with well-defined p - and n - regions, (2) $|n_{H,layer}|$ shows a minimum value (n^*) for p - and n - conduction, (3) σ shows a roughly linear carrier density dependence for $n^* < n < n_{bulk}$ where $n_{bulk} \approx 5 \times 10^{12}/\text{cm}^2$ is the carrier density above which the bulk conduction band is expected to be populated, and (4) a minimum conductivity ($\sigma_{min} = 2 e^2/h$ to $5 e^2/h$) is observed.

As briefly introduced in the chapter 2, theoretical calculation of 2D transport in Dirac systems including graphene and the surface of TIs predicts the conductivity limited by charged-impurity scattering in of the form (assuming linear Dirac band) [35],

$$\sigma(n) \sim C \left| \frac{n}{n_{imp}} \right| [e^2/h] \quad \text{for } n > n^* \quad (4.3a)$$

$$\sigma(n) \sim C \left| \frac{n^*}{n_{\text{imp}}} \right| [e^2/h] \text{ for } n < n^* \quad (4.3b)$$

where n_{imp} is the charged impurity density, C is a constant which depends on the Wigner-Seitz radius r_s , and n^* is identified as the residual carrier density in electron and hole puddles. For Bi_2Se_3 on SiO_2 [35, 36, 38] we expect $0.05 < r_s < 0.2$ and $30 < C < 300$. For $n^* < n < \approx 5 \times 10^{12}/\text{cm}^2$, I fit $\sigma(n)$ to Eqn. (4.3a) (Fig. 4.7a-dashed lines), to obtain the field-effect mobility $\mu_{\text{FE}} = Ce/n_{\text{imp}}h$ for each device. μ_{FE} ranges from $320 \text{ cm}^2/\text{Vs}$ to $1500 \text{ cm}^2/\text{Vs}$ reflecting different amounts of disorder in the samples. The observed linear $\sigma(n)$ implies that charged impurity limits charge transport at low n (but outside charge inhomogeneous regime) in the current devices, as expected from theoretical calculation. I identify the initial n -type dopants, and environmental doping induced by mechanical exfoliation as likely sources of the disorder. The decrease in μ_{FE} with further electrolytic gating (device 1 run 2 compared to run 1) indicates electrochemical damage, likely solvation of Se ions. Along with the charged impurity scattering, it was shown in chapter 2 that short range disorder, i.e, neutral point defects or acoustic phonons, results density independent conductivity. As discussed in Chapter 2, the experimentally observed sublinear $\sigma(n)$ can naturally be explained by a combination of long-range ($\sigma \propto n$) and short-range ($\sigma \propto \text{constant}$) scattering, since the conductivities add in inverse according to Matthiessen's rule.

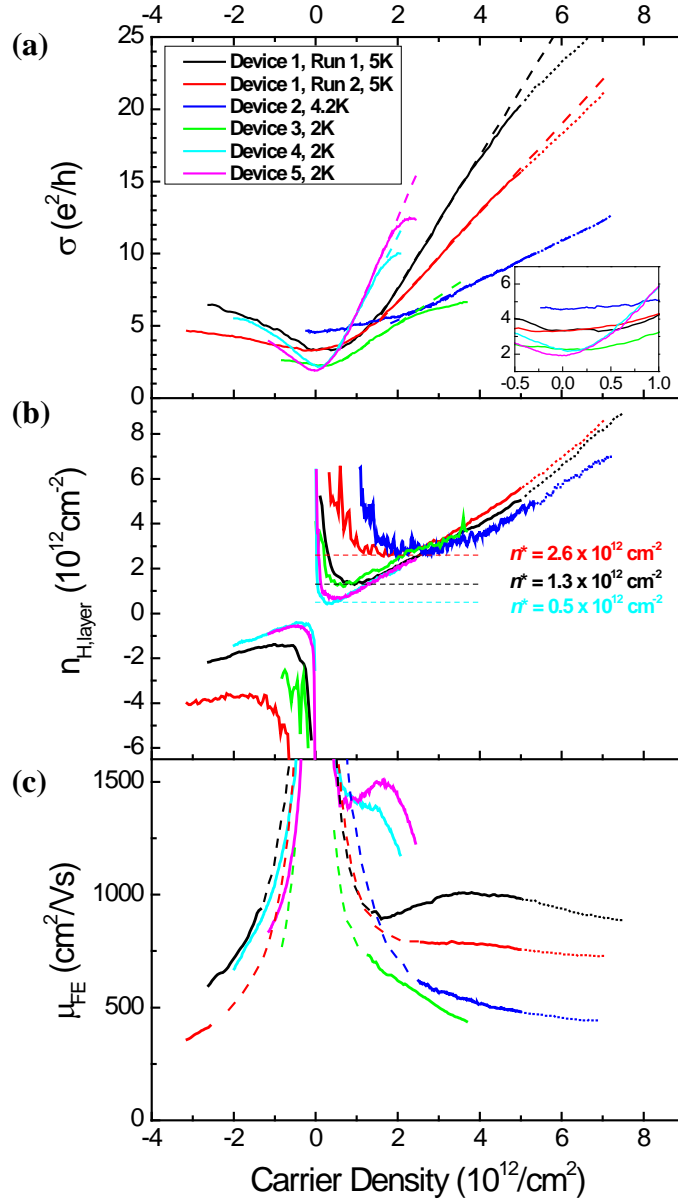


Figure 4.7 Transport properties of Bi_2Se_3 surface state. **(a)** The conductivity per surface vs. carrier density per surface $\sigma(n)$ at zero magnetic field for five different devices. Device 1 to 3 are electrolyte gated and device 4 and 5 are F4TCNQ doped. The inset shows $\sigma(n)$ near the Dirac point. Dashed lines are fits to Eqn. (1a). Transport data outside the topological regime ($n > n_{\text{bulk}} = 5 \times 10^{12}/\text{cm}^2$) are denoted as dotted curves. **(b)** Hall carrier density per surface vs. carrier density measured at the same conditions as in **(a)**. Dashed lines show residual carrier density n^* (defined in the text) for different devices **(c)** Variation of field effect mobility as a function of carrier density. Dashed curves indicate the region $|n| < n^*$ within which electron and hole puddles dominate transport.

4.2.2 Charge inhomogeneity driven electron hole puddles and minimum conductivity

The limit of charge transport in the current Bi_2Se_3 is identified as charged impurities in the last section. In intrinsic surface state of TIs, the Dirac point is a singular point that separates the conduction and the valence band. However, the presence of charged impurities will induce carriers in the system, so that intrinsic Dirac point cannot be realized experimentally [31]. Moreover, the spatially inhomogeneous potential fluctuation implies that these residual carriers are distributed randomly over the surface [53]. Each band of the residual distribution are filled up to certain Fermi energy, E_F , determined by the electrostatic potential configuration of the surface environment and, depending on averaged E_F , can be electron or hole like.

These charge inhomogeneity driven effective carriers called “electron-hole puddles” have been experimentally observed both for graphene and TIs [37, 53]. Figure 4.8 shows representative observations in graphene (a) and Mn doped Bi_2Se_3 (b). In Ref. [37], electron-hole puddles were measured using scanning single electron transistors, where n^* was measured to be in the order of $\sim 10^{11}\text{cm}^{-2}$. More recently, these puddles in TIs were observed using scanning tunneling microscopy and n^* order of 10^{12}cm^{-2} was estimated from the known band structure of Bi_2Se_3 [53]. In this sense the transport properties we measure at this low Fermi level or carrier density regime is determined by the amount of charged impurities in the system, as pointed out in Chapter 2, where I briefly introduced self-consistent determination of electron-hole puddle density n^* and associated minimum conductivity σ_{\min} . In transport experiment, the inhomogeneity

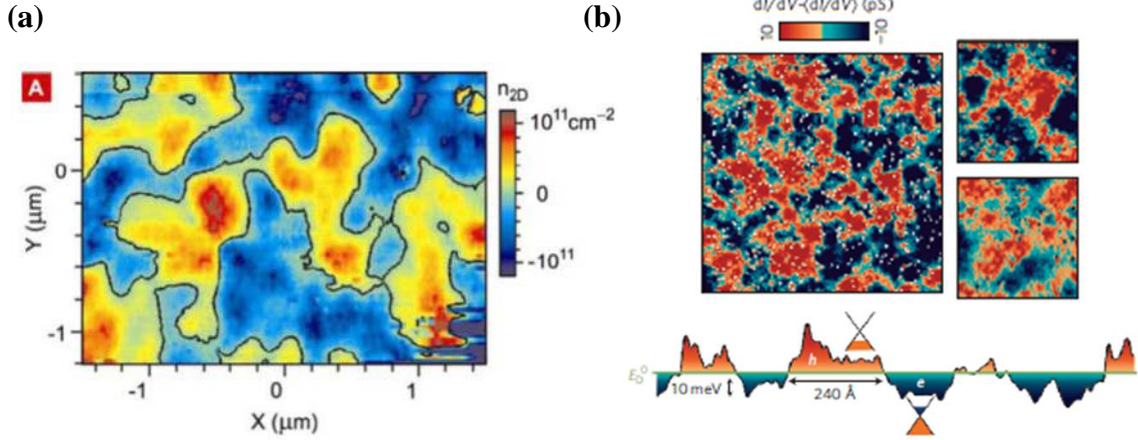


Figure 4.8 Charge inhomogeneity driven electron-hole puddles in (a) graphene measured using scanning single electron transistor [37] ($n^* \sim 10^{11} \text{cm}^{-2}$) (b) Mn-doped Bi_2Se_3 using scanning tunneling microscope [53] ($n^* \sim 10^{12} \text{cm}^{-2}$)

driven electron-hole puddles can be directly measured by measuring minimum carrier density in

Hall measurement (Fig. 4.7b dashed lines). Within $|n| < n^*$ the conduction is carried through charged compensated landscape, and the single band conduction cannot hold.

The observed σ_{\min} of the Dirac electronic band can be well understood through Eqn. 4.3b as due to the residual carrier density n^* in electron and hole puddles induced by the charged impurity potential at nominally zero carrier density, $\sigma_{\min} = n^* e \mu$, where n^* is calculated self-consistently as a function of n_{imp} , r_s , and d , the distance of the impurities to the Dirac surface. Qualitatively, the self-consistent theory predicts that n^* almost linearly increases with increasing disorder, whereas mobility $\sim 1/n_{\text{imp}}$ so that σ_{\min} depends only weakly on disorder. I employed the self-consistent theory developed by S. Adam et al. [31], and applied to Bi_2Se_3 . I included in Appendix B the detailed *Mathematica* codes I wrote for iterative calculation of n^* and σ_{\min} as a function of n_{imp} . At low density, the finding that $n^* \ll n_{\text{imp}}$ (Eq. 2.6) for the case of Bi_2Se_3 is an important prediction of the

self-consistent theory. If n^* was of the same order as n_{imp} as assumed in Ref. [35] then the disorder induced energy fluctuations would be comparable to the band-gap and we would have been unable to observe the minimum conductivity and other surface (p -type) band properties.

Figure 4.9 shows the experimentally observed residual carrier density n^* per surface for each device (Fig. 4.9a) as well as σ_{min} per surface (Fig. 4.9b) as a function of the experimentally-measured inverse mobility $1/\mu_{\text{FE}}$ which reflects the disorder strength. (For devices in which n^* could be measured for p and n -type conduction, both values are shown.) The shaded regions reflect the expectations of the self-consistent theory using parameter ranges $0.05 < r_s < 0.2$, and $d = 0.1 \text{ \AA}$ to 15 \AA . I found a good agreement between experiment and theory in that (1) σ_{min} is weakly dependent on disorder strength ($1/\mu_{\text{FE}}$) and (2) n^* increases with disorder strength ($1/\mu_{\text{FE}}$). Particularly for increasing disorder in the same device (device 1 run 1 vs. run 2), n^* increases but σ_{min} is nearly unchanged (arrows in Figs. 4a and 4b). The experimental data agree best with the upper range of the theoretical estimates, corresponding to small $d = 0.1 \text{ \AA}$ and large $r_s = 0.2$. Assuming $r_s = 0.2$, I infer an impurity density n_{imp} ranging from $0.5 \times 10^{13} \text{ cm}^{-2}$ to $2.3 \times 10^{13} \text{ cm}^{-2}$, much larger than for graphene exfoliated on similar SiO_2 substrates [41], but comparable to the observed initial doping level of $1 \times 10^{13} \text{ cm}^{-2}$ to $3 \times 10^{13} \text{ cm}^{-2}$ (see Fig. 4.1a), which, along with observed linear $\sigma(n)$ at Boltzmann transport regime, suggests that the dopants are the charged impurities responsible for limiting the mobility.

The simple theory somewhat underestimates n^* and σ_{min} , but it is expected that the theory can be refined to take into account the non-linearity and asymmetry of the

Bi₂Se₃ surface state bands [36]. Notably, the larger Fermi velocity for the electron band would increase the conductivity above the estimate in Eq. 4.2a for n-type conduction, indicating that disorder strength is likely somewhat underestimated from the n-type mobility. Shifting the points to the right (to larger disorder strength) in Fig. 4.9 would indeed improve the agreement between experiment and theory.

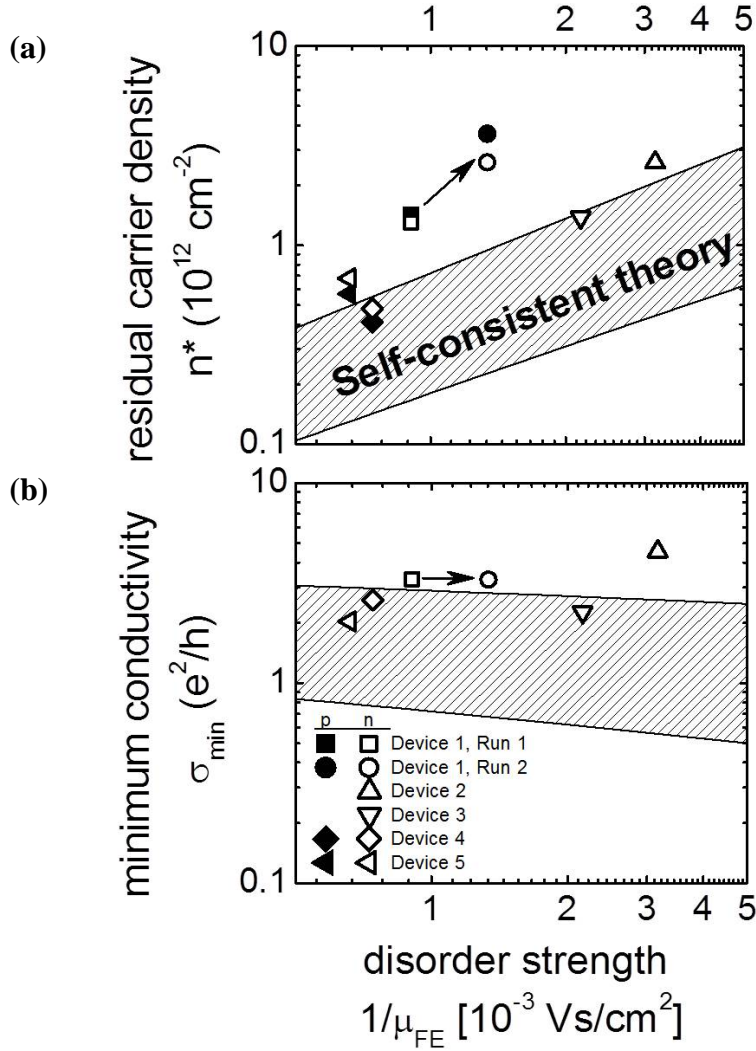


Figure 4.9 Minimum conductivity and charge inhomogeneity vs. inverse mobility. **(a)** Residual carrier density n^* vs. inverse field effect mobility ($1/\mu_{FE}$) and **(b)** minimum conductivity σ_{min} vs. $1/\mu_{FE}$. Shaded areas indicate the expectations of the self-consistent theory of Ref. [31], symbols are experimental data.

4.3 Conclusion

Reducing n-type doping of TI thin films by external agents provides an effective and simple way to probe topological surface transport properties in the absence of bulk conduction. I demonstrated the fundamental signatures of surface-only transport in my samples at cryogenic temperatures, including linear Hall resistivity and a well-defined gapless ambipolar field effect, as well as a charge-inhomogeneous minimum conductivity region. Moreover, I showed that in the thin film geometry the Fermi energy of both top and bottom surfaces can be simultaneously tuned due to strong capacitive coupling provided by insulating bulk with high dielectric constant, the result from which I deduce transport quantities of each surface. For present Bi_2Se_3 devices the level of charged impurity disorder is in the order of $\sim 10^{13} \text{ cm}^{-2}$ limiting the mobility to $320 \text{ cm}^2/\text{Vs}$ to $1500 \text{ cm}^2/\text{Vs}$. For comparison, this is two orders of magnitude larger impurity density compared to nominal graphene ($n_{\text{imp}} \sim 10^{11} \text{ cm}^{-2}$). However, due to large dielectric constants in existing topological insulators, reduction of impurity concentrations to levels seen in the best bulk crystals ($< 10^{17} \text{ cm}^{-3}$ corresponding to $< 10^{11} \text{ cm}^{-2}$ in a 10 nm thick crystal [24]) would allow mobilities exceeding $10^5 \text{ cm}^2/\text{Vs}$. Hence understanding and eliminating the doping presently observed in all thin crystals and films is of central importance to increasing the mobility of the topological surface state.

Chapter 5 Intrinsic electron-acoustic phonon resistivity of Bi_2Se_3 in the topological insulator regime

The helicity of the surface carriers in TI is protected by time reversal symmetry and is exhibited in spin-momentum locking [6] which may be exploited in spintronic [54] and opto-spintronic devices [55, 56]. While the helical surface state is robust against backscattering by time-reversal-invariant disorder [9], the eventual surface conductivity and mobility is determined entirely by carrier scattering from disorder and phonons since scattering at angles less than π is possible in the two-dimensional surface state. The intrinsic limits to conductivity and mobility at finite temperature will be set by the electron-phonon interaction, hence the study of electron-phonon coupling in TIs is of central importance in assessing potential electronic applications.

Electron-acoustic phonon scattering in a Dirac band was shown to give a resistivity which is *independent* of carrier concentration but linearly dependent on temperature in the high-temperature limit, a result which explained the relative independence of the resistivity on carrier concentration in intercalated graphites long before the experimental study of graphene [57]. The carrier density independent electron-phonon resistivity has since been observed in graphene [58], but not in the topological insulator surface state which also has a Dirac dispersion.

The goal of the current chapter is to combine experiment and theory in order to ascertain the intrinsic limit to the 2D transport mobility of TI surface carriers arising from phonon scattering. In Section 5.1 and 2, I first discuss experimentally observed temperature dependent Hall carrier density and compare the result with thermal activation

model with approximated Bi_2Se_3 surface and bulk band structure in order to identify the region of Fermi level where thermal activation from the bulk band negligible. In section 5.3, the temperature dependent longitudinal resistivity in this regime is explored both experimentally and theoretically, and implications for the surface conductivity and mobility limit at room temperature are discussed.

5.1 Temperature dependent carrier density in gate tuned Bi_2Se_3 : experiment

Topological insulator consists of two very distinct types of electronic band structures: gapped bulk and gapless metallic surface bands. Although I showed in chapter 4 that surface-dominant conduction can be realized by gate tuning at cryogenic temperatures, it is not clear whether this can hold at elevated temperature. Thus, before examining temperature dependent resistivity, it is important to determine contribution of bulk and surface bands to the transport. For this purpose, the measurement of temperature dependent Hall carrier density provides valuable information. Briefly speaking, metallic conduction in the surface band is marked by nearly temperature-independent carrier density as probed by the Hall effect. On the other hand, the carrier density can be strongly temperature dependent in the presence of the gapped bulk band, and the much lower mobility of the bulk band compared to the surface band causes the Hall carrier density to deviate from the expected value inferred from the gate charge. In the Section 5.1 and 5.2, I show that when the gate-tuned chemical potential of a Bi_2Se_3 thin film is near or below the Dirac point the carrier density is strongly temperature dependent reflecting thermal activation from the nearby bulk valence band, while above the Dirac point, unipolar n-type surface conduction can be achieved with negligible thermal activation of bulk

carriers. In this regime temperature dependent resistivity can be used to determine electron-phonon coupling of the surface bands.

Figure 5.1 (a) shows the Hall carrier density n_H of a 10 nm thick Bi_2Se_3 device as a function of gate voltage V_g and temperature T , where several line cuts with respect to V_g at various temperatures are plotted in figure 5.1 (b). Similar to the devices studied in chapter 4, one can observe the gapless ambipolar electric field effect, which is indicated by the sign change in n_H at the charge neutrality point ($V_{g,0}$, Fig. 5.1(b) dashed lines) associated with the Dirac point of the topological surface states. Likewise, the positive (negative) divergence in n_H when approaching $V_{g,0}$ from above (below) is due to inhomogeneity-driven electron-hole puddles as shown in Chapter 4. At low temperature (e.g., 2 K), $n_H(V_g)$ is linear over broad ranges of n - and p -doping with slope $dn_H/dV_g = C_g/e$ indicating a gate capacitance $C_g = 11 \text{ nFcm}^{-2}$ as expected for 300 nm-thick SiO_2 . However as temperature is raised, n_H shows markedly different behaviors depending on the level of Fermi energy tuned by V_g . On one hand, $V_{g,0}$ shifts to a more negative voltage and the slope dn_H/dV_g is reduced near and below $V_{g,0}$. On the other hand, $n_H(V_g)$ remains temperature-independent for the unipolar n -type conduction regime ($V_g > -20 \text{ V}$).

I first explore the origin of the temperature dependence of n_H . In chapter 4, I experimentally demonstrated by dual electrostatic gating that significant band bending is absent in thin, lightly doped Bi_2Se_3 crystals due to strong capacitive coupling of the two topological surfaces through the high-dielectric-constant insulating bulk Bi_2Se_3 . Therefore, although a superficially similar shift of $V_{g,0}$ was observed in Ref. [27] and interpreted there as due to a reduction in the effective bulk gap due to band-bending, I rule out this effect in my devices. In figure 5.1 (c) I show an example of temperature-

dependent increase of electron concentration (decreasing hole concentration) at $V_g = -90V$. Note that the temperature-dependent n-type doping at fixed gate voltage implies that, although the total induced charged density is fixed by a gate voltage, there is an additional source/drain of charges in the sample, which is not detected in the Hall measurement.

An important clue on the source of electrons can be obtained from the behavior of $V_{g,0}$. At $V_{g,0}$ we expect that the surface band is completely electron-hole compensated, thus the shift of $V_{g,0}$ at a certain temperature compared to 2K, gives a number additional electrons we need to remove to achieve charge neutrality of the surface band by the relation $n_{\text{excess}} = C_g(V_{g,0} - V_{g,0}(2K))$. The location of $V_{g,0}$ is shown in Fig. 5.1(a) as a pink dashed curve. I found that the shift in $V_{g,0}$ hence n_{excess} , shows roughly thermally activated behavior. Figure 5.2 shows an Arrhenius plot of n_{excess} (T) in the range of $80 < T < 200$ K (Fig. 5.2), where fitting to the form $n_{\text{excess}} = n_0 \exp(-E_v/k_B T)$ gives an activation energy of 60 meV.

The roughly thermally activated behavior of n_{excess} implies that the additional carriers originate from the nearby bulk band. The energy scale for thermal activation corresponds well with the expected separation of the bulk valence band and the Dirac point of the topological surface band in Bi_2Se_3 [38]. Hence significant thermal activation of electrons from the bulk valence band to the surface band, hence leaving holes in the bulk valence band, should occur at modest temperatures, resulting in a negative shift of $V_{g,0}$. In the next section, in order to corroborate this picture, a more detailed model of temperature dependent carrier density is developed and compared with the experimental observation.

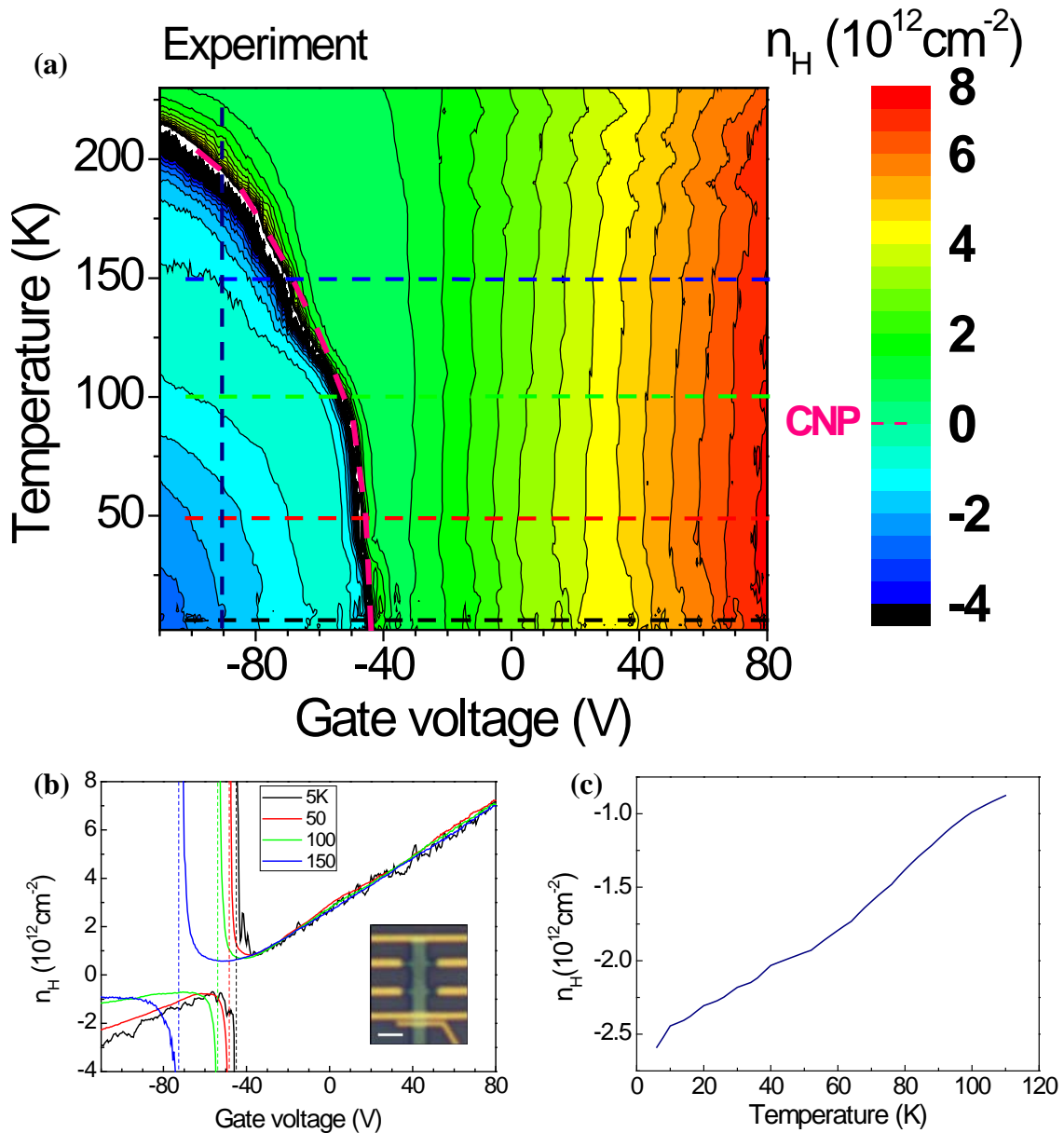


Figure 5.1 Temperature dependent carrier density : experiment (a) Measured Hall carrier density (n_H) of a thin exfoliated Bi_2Se_3 device as a function of back gate voltage (V_g) and temperature (T). Pink dashed curve shows a T dependent trace of charge neutrality point (CNP; $V_{g,0}$) (b) n_H vs. V_g at various temperatures indicated by dashed lines in (a). Dashed lines indicate points of charge neutrality. The inset shows an optical micrograph of the device. The scale bar is $2 \mu\text{m}$. (c) n_H vs. T at $V_g = -90$ as indicated by a vertical dashed line (a).

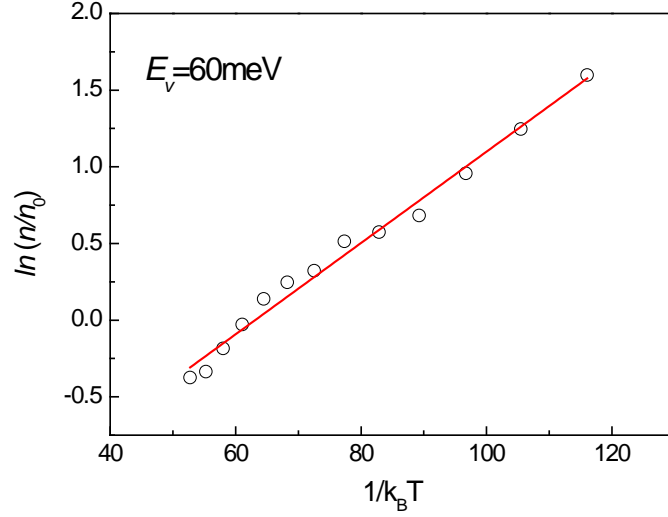


Figure 5.2 Determination of bulk valence band edge. Arrhenius plot of excess carrier density $n = C_g(V_{g,0}(T) - V_{g,0}(2K))$ in the temperature range $50 < T < 200$. Linear fit to the form $n = n_0 \exp(-E_v/k_B T)$ results the position of bulk valence band edge $E_v = 60 \text{ meV}$.

5.2 Temperature dependent carrier density in gate tuned Bi_2Se_3 : modelling

I develop a more detailed model of $n_H(T)$ as follows. As discussed in the above section, the discrepancy between gate induced and measured charge density suggests that there are charges in the bulk band that are not picked up in Hall measurement. I assume that n_H reflects the density of surface carriers only. Since in a multi-band system the net Hall conductivity is the mobility-weighted average of the Hall conductivities of each band, the assumption reflects the expectation of much lower carrier mobility for the bulk valence band which has much higher effective mass and no topological protection from backscattering [2].

I assume that two bands are important in determining $n_H(T)$: The surface band with dispersion, $E_{2D}(k) = \hbar v_{F,0}k + \frac{\hbar^2 k^2}{2m_s^*}$ and the bulk valence band with dispersion, $E_{3D}(k) = E_v - \frac{\hbar^2 k^2}{2m_b^*}$ where I estimate the energy of band edge $E_v = -60 \text{ meV}$ from the observed temperature dependent shift of $V_{g,0}$ (I neglect the bulk conduction band for the Fermi level near Dirac point, since it is significantly farther from the Fermi energy). For the calculation, I used the parameters of the Fermi velocity near Dirac point $v_{F,0} = 3 \times 10^7 \text{ cm/s}$, and the effective mass $m_s^* = 0.3 m_e$ of the surface band, where m_e is the mass of free electron. The effective mass of the valence band is not well known but thought from theory and ARPES measurements [21, 59] to be large; I found a good fit to my experimental data on thermal activation of carriers by using $m_b^* = 2.6 m_e$ for the bulk valence band.

Using these band structures, the temperature and gate voltage dependent carrier density of the surface band $n_{2D}(V_g, T)$ are calculated as follows. The gate voltage induced total carrier density as a function of chemical potential μ and temperature can be written as,

$$n_{tot}(\mu, T) = C_g (V_g - V_{g,0} |_{2K}) / e = \int_0^\infty D_{tot}(E) f(E - \mu) dE - \int_{-\infty}^0 D_{tot}(E) (1 - f(E - \mu)) dE \quad (5.1)$$

where $D_{tot} = D_{2D} + tD_b$ is total density of states including surface (D_{2D}) and bulk valence band (D_b) and $f(x) = 1 / (e^{x/k_B T} + 1)$ is Fermi-Dirac distribution function.

The purpose of this calculation is to obtain $n_{2D}(V_g, T)$ from $n_{tot}(\mu, T)$. Eqn. (5.1) is numerically inverted to obtain μ as a function of V_g and T . The information of $\mu(V_g, T)$ is used to calculate n_{2D} similar to Eqn. (5.1) replacing D_{tot} to D_{2D} . In the Appendix B, I

included *Mathematica* code for this calculation. Figure 5.2(b) shows the Bi_2Se_3 density of states $D(E)$ for surface and bulk bands used in our model. Figure 5.2a shows the calculated $n_{2D}(V_g, T)$ based on these $D(E)$. As shown in the Figure 5.2a, the model captures the essential characteristics of the measured $n_H(V_g, T)$ (compare with Fig. 5.1a): $V_{g,0}$ shifts to negative voltage in a roughly thermally-activated manner, C_g in the hole-doped region is comparable to that of 300nm SiO_2 at low temperatures but is gradually suppressed as temperature is increased due to thermal activation from bulk valence band, and n_H in the electron-doped region ($V_g > -20$ V) is nearly independent of temperature. The model fails to describe the divergence of n_H near $V_{g,0}$ due to charge inhomogeneity which is not included in the model. However, the overall success of the model supports our picture of unipolar *n*-type transport dominated by the topological surface state in the absence of bulk carriers in the region -20 V $< V_{g,0} < 80$ V, corresponding to carrier densities in the topological surface of ranging from $1.5 \times 10^{12} \text{ cm}^{-2}$ to $8 \times 10^{12} \text{ cm}^{-2}$. Therefore, one can examine temperature dependent resistivity in this gate voltage range to determine electron-phonon coupling of the surface state of Bi_2Se_3 topological insulator, which is the subject of the following section.

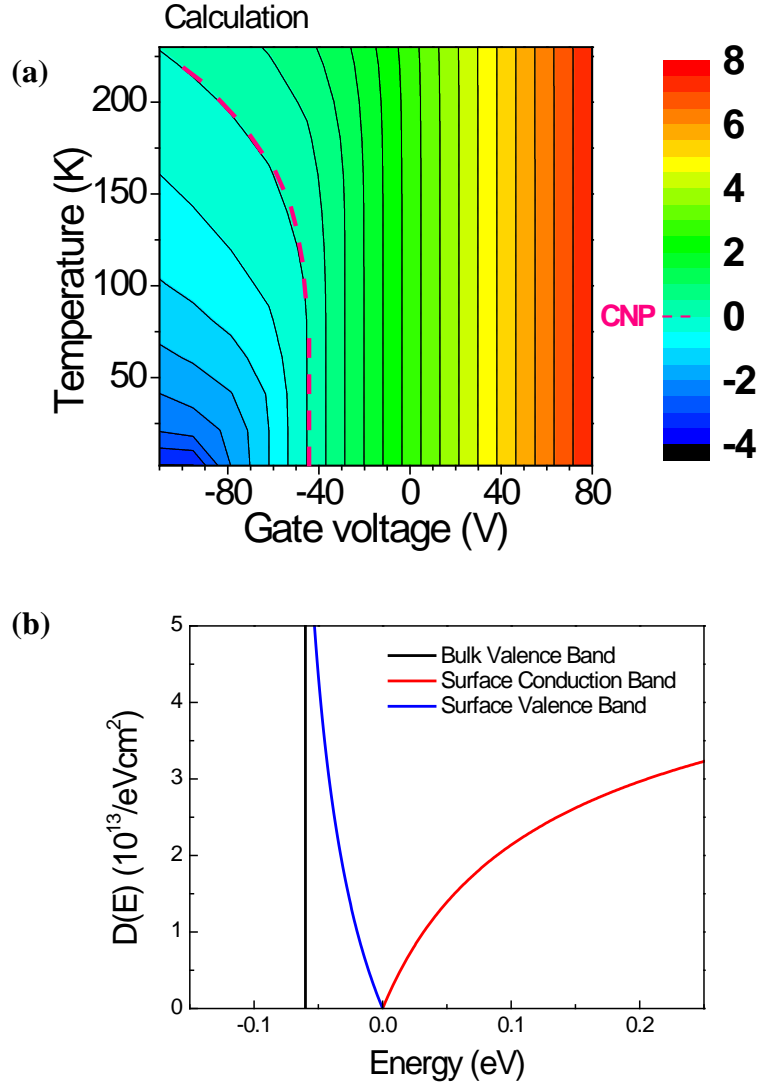


Figure 5.3 Temperature dependent carrier density : calculation **(a)** Calculated surface band carrier density as a function of V_g and T using a thermal activation model discussed in text. **(b)** Energy-dependent density of states $D(E)$ for the thermal activation model, showing surface (red and blue solid lines) bands and bulk valence (black solid line) band.

5.3 Electron-acoustic phonon resistivity

Experimental studies of inelastic scattering processes at the TI surface have been confined to angle-resolved photoemission [60, 61] or helium atom surface scattering

probes [62] of the quasiparticle or phonon lifetimes respectively. These studies do not measure directly the resistivity, and the inferred electron-phonon coupling constants are not consistent with each other, varying by a factor of ≈ 5 . The high level of doping in bulk TI crystals, hence dominant bulk conduction, hinders the unambiguous analysis of surface signatures in electronic transport [24, 51, 63]. However, I demonstrated above that by comparing experimental observation and simple thermal activation model that surface dominant conduction even at elevated temperatures can be achieved in the range of n -type carrier densities from $1.5 \times 10^{12} \text{ cm}^{-2}$ to $8 \times 10^{12} \text{ cm}^{-2}$ for the case of a gate tuned thin Bi_2Se_3 device.

I now discuss temperature-dependent longitudinal resistivity $\rho_{xx}(T)$ in this unipolar n -type regime for two Bi_2Se_3 devices with similar thickness of 10nm and initial doping. Figure 5.3a shows entire 2D map of $\rho_{xx}(T)$ of device 1 as a function of V_g and T . Figure 5.3b shows $\rho_{xx}(T)$ at different n_H (from $1.5 \times 10^{12} \text{ cm}^{-2}$ to $7 \times 10^{12} \text{ cm}^{-2}$) tuned by V_g . Generally, $\rho_{xx}(T)$ is metallic ($d\rho_{xx}/dT > 0$) and saturates at low $T < 40\text{K}$ as expected for gapless surface states. In the intermediate temperatures of $50 \text{ K} < T < 150 \text{ K}$, $\rho_{xx}(T)$ is linearly increasing with T consistent with scattering of degenerate electrons with phonons that are populated according to the classical equipartition distribution. For device 1 the highest Hall mobility at low temperature is $1430 \text{ cm}^2/\text{Vs}$ at $n_H = 2.6 \times 10^{12} \text{ cm}^{-2}$ which is reduced by more than 20% to $1120 \text{ cm}^2/\text{Vs}$ at $T = 150 \text{ K}$.

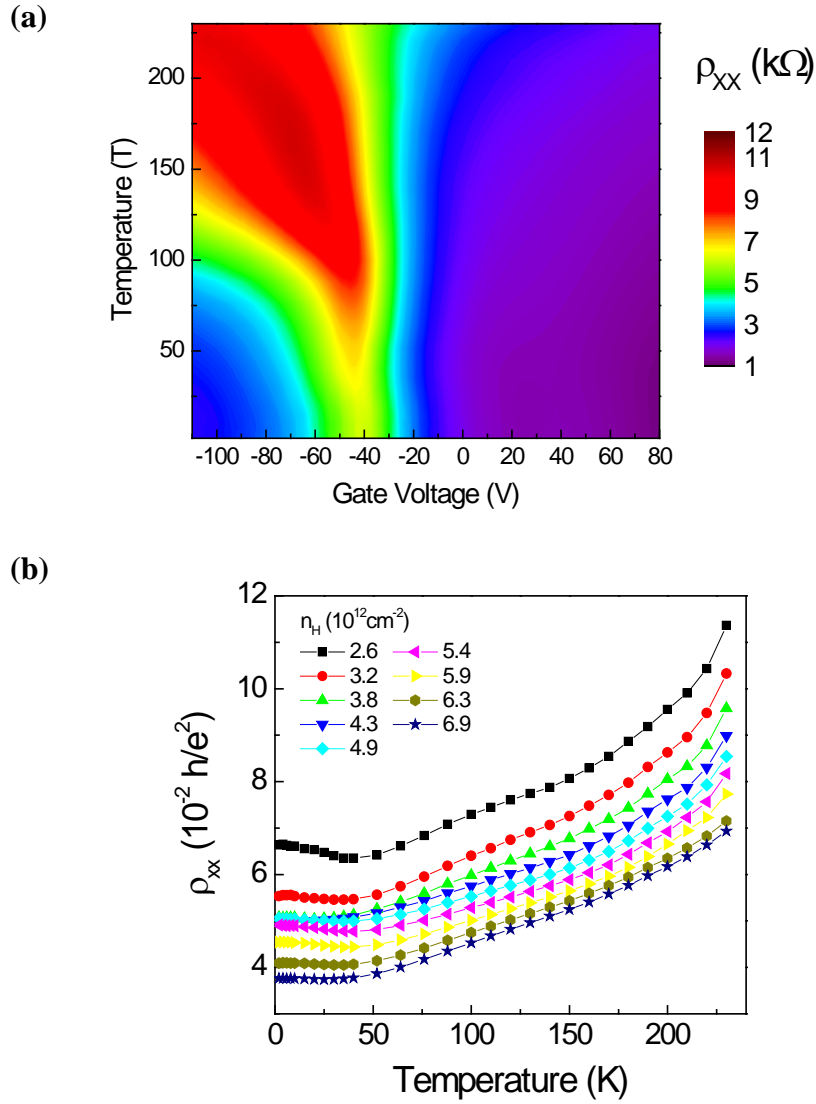


Figure 5.4 Temperature dependent resistivity : experiment **(a)** Longitudinal resistivity ρ_{xx} of a 10nm thick Bi_2Se_3 (device 1) as a function of gate voltage V_g and temperature T **(b)** ρ_{xx} of the device 1 as a function of temperature at different carrier densities for which thermal activation from the bulk is negligible.

In the high temperature and high carrier density regime, the temperature dependence of resistivity $d\rho_{xx}/dT$ mainly comes from the electron-phonon scattering, the asymptotic high-temperature behavior of which can be expressed as

$$\rho_{ph} \sim \frac{\pi D^2 k_B T}{e^2 \hbar v_F^2 v_{ph}^2 \rho_m} \quad (5.2)$$

where ρ_{ph} is the electron-phonon scattering limited resistivity, D is the deformation potential and $v_{ph} = 2900$ m/s is the phonon velocity, $\rho_m = 7.68 \times 10^{-7}$ gcm⁻² is the mass density of Bi₂Se₃ for a single quintuple layer (thickness ~ 1 nm) corresponding to the penetration length of the topological surface state into the bulk [64]. As can be seen from Eqn. (5.2), $d\rho_{ph}/dT$ is determined by the ratio of the deformation potential to the Fermi velocity $D/\hbar v_F$.

In real samples with disorder, other effects (e.g. screening, potential fluctuation induced puddles) may contribute to the temperature dependence of the resistivity. Charged impurity scattering and potential fluctuations play important roles in determining the minimum conductivity and low temperature transport of the topological surface state [28, 31], as analyzed in detail in chapter 4. Due to the strong suppression of the back-scattering in TI surface transport, metallic temperature-dependent screening effects are relatively weak [65], and are therefore not discussed here. Thermal activation across potential fluctuations gives rise to an insulating behavior of temperature-dependent resistivity ($d\rho/dT < 0$) which may be important at low carrier density where phonon effects are suppressed. To determine whether Eqn. (5.2) accurately describes the resistivity in our samples, I collaborated with Qiuzi Li in Prof. Shanker Das Sarma group in University of Maryland for calculating a realistic values of temperature-dependent resistivity of the topological surface state including electron-phonon scattering [66, 67] and the effects of charged impurity scattering [65] and potential fluctuations [28, 53]. Briefly speaking, she have calculated the resistivity by using Boltzmann transport theory

and effective medium theory, in which it is assumed that the potential fluctuation follows a Gaussian form parameterized by the potential strength s . The detailed theories have been presented in a recent publication [68], and I quote the main results in this section.

One serious issue in a quantitative theoretical determination of the temperature dependence is that the deformation potential coupling for the surface electrons is simply not known, and theoretical determination from first principles is imprecise. Since the resistivity depends on the square of the deformation potential $\rho \sim D^2$ any imprecision in D is magnified in ρ . An experiment-theory comparison is therefore essential to determine the value of D . Qiuzi Li and I have therefore carried out a careful regression fit to make the linear temperature dependence of the experiment and theory agree with each other so as to obtain the best possible estimate of D in the system.

Figures 5.4a and b show the calculated $\rho_{xx}(T)$ for two different disorder (charged impurity density) strengths in the range of temperatures for which the experiment sees linear $\rho_{xx}(T)$. We find the best match to the experimentally measured $d\rho_{xx}/dT$ at high carrier density for a deformation potential $D = 22 \text{ eV}$ and Fermi velocity $v_F = 7 \times 10^7 \text{ cm/s}$ ($D/\hbar v_F = 4.7 \text{ \AA}^{-1}$). We take the effective background dielectric constant to be $\kappa = 33$, the average distance of the charged impurity from the topological surface $d = 1 \text{ \AA}$. In Fig. 5.4a, the charged impurity density $n_{\text{imp}} = 3 \times 10^{13} \text{ cm}^{-2}$ (charge inhomogeneity driven potential fluctuation $s = 90 \text{ meV}$) and in Fig. 5.4b $n_{\text{imp}} = 1.5 \times 10^{13} \text{ cm}^{-2}$ ($s = 65 \text{ meV}$). The disorder strength is the major determinant of the carrier density dependence of the resistivity as reflected in Figs. 5.3a and 5.3b. The calculated resistivities bracket the experimental data, indicating that the experimental disorder is comparable to the estimates. A quantitative agreement in the carrier density dependence of the resistivity is

not expected since the model does not include the significant non-linearity of the surface bands [36].

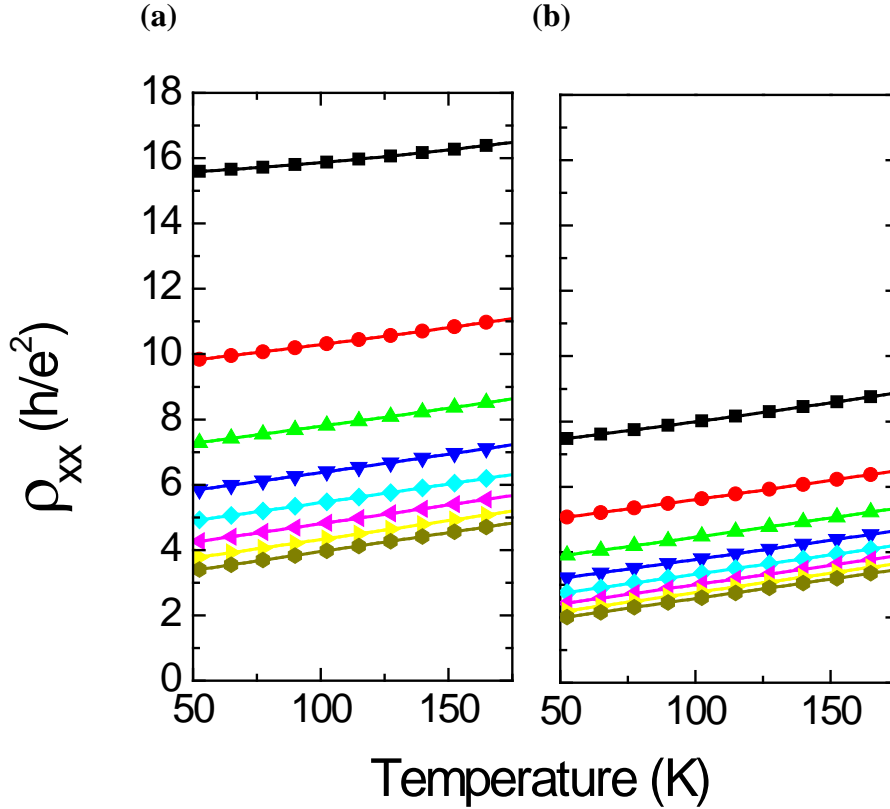


Figure 5.5 Temperature dependent resistivity : calculation. Calculated total resistivity ρ_{xx} as a function of temperature for different carrier densities $n = 2,3,4,5,6,7,8,9 \times 10^{12} \text{ cm}^{-2}$ from top to bottom. In (a) the charged impurity density is $n_{\text{imp}} = 3 \times 10^{13} \text{ cm}^{-2}$ and the potential fluctuation strength $s = 90 \text{ meV}$. In (b) $n_{\text{imp}} = 1.5 \times 10^{13} \text{ cm}^{-2}$ and $s = 65 \text{ meV}$.

I now turn to estimation of electron-acoustic phonon coupling strength and intrinsic limit of surface mobility from the measured and calculated $d\rho_{xx}/dT$. Figure 5.6a shows the average slope $d\rho_{xx}/dT$ for $50 \text{ K} < T < 150 \text{ K}$ at different n_H for two different experimental runs with two different samples. $d\rho_{xx}/dT$ varies by less than a factor of 1.75

while the carrier density varies almost fourfold. A broad peak in $d\rho_{xx}/dT$ occurs around $n_H = 3.5 \times 10^{12} \text{ cm}^{-2}$, and $d\rho_{xx}/dT$ approaches a roughly density independent value of $3 \Omega/K$ at high n_H . Figure 5.5b shows the calculated slope $d\rho_{xx}/dT$ for $50 \text{ K} < T < 150 \text{ K}$ as a function of carrier density n . At low n the slope increases monotonically with density, and is disorder-dependent. At high n , the slope asymptotically approaches a constant consistent with Eqn. (5.2). The results indicate that the slope measured at high n reflects electron-phonon scattering even at large disorder strength; hence the experimentally measured slope of $3 \Omega/K$ determines the ratio $D/\hbar v_F = 4.7 \text{ \AA}^{-1}$ at high carrier density. Assuming a Fermi velocity $v_F = 5\text{-}7 \times 10^5 \text{ cm/s}$ consistent with ARPES measurements [2, 38], the corresponding deformation potential is $D = 15 - 22 \text{ eV}$. The experimentally observed $d\rho_{xx}/dT$ shows a peak at lower carrier density, which we understand as a competition between decreasing v_F due to the non-linearity of the surface bands (not included in the theory) which leads to increased $d\rho_{xx}/dT$, and thermal activation across the potential fluctuations which leads to a reduced $d\rho_{xx}/dT$ near the Dirac point as seen in Fig. 5.5b.

Using the observed value of $d\rho_{xx}/dT = 3\Omega/K$, total electron-phonon resistivity at room temperature is $\sim 900 \Omega$, therefore the resistivity per surface is 1800Ω since they are in parallel. This result is roughly independent of carrier density. The corresponding maximum conductivity per surface is $560 \mu\text{S} \approx 14 e^2/h$. The surface conductivity may be expressed as $\sigma = (e^2/2h)k_F l$ where k_F is the Fermi wavevector and l is the mean free path. Thus the surface is only modestly above the Ioffe-Regel limit $k_F l = 1$, and strongly diffusive at room temperature. The Fermi velocity decrease near the Dirac point leads to higher resistivity and lower $k_F l$.

One may also estimate the maximum carrier mobility for the surface state. For a roughly constant conductivity as found for a Dirac band limited by acoustic phonon scattering, the mobility diverges at low carrier density: $\mu = \sigma/ne$. At finite temperature the lowest achievable carrier density is the intrinsic carrier density:

$$n_{\text{int}}(T) = \int_0^{\infty} D(E)g(E)dE = \frac{(kT)^2}{2\pi\hbar^2v_F^2} \int_0^{\infty} \frac{E/kT}{e^{E/kT} + 1} dE/kT = \frac{(kT)^2}{2\pi\hbar^2v_F^2} 0.82247$$

Due to asymmetry of the surface band, about factor of two reduction of $v_F = 3 \times 10^7$ cm/s is expected next Dirac point. Thus using $v_F = 3 \times 10^7$ cm/s and $T = 300\text{K}$, I estimate the intrinsic carrier density $n_{\text{int}} = 2.1 \times 10^{11} \text{ cm}^{-2}$ per surface at room temperature. Moreover, correcting for reduced Fermi velocity also for resistivity, I estimate 3000-4200 $\Omega/\text{surface}$. Therefore highest possible mobility is $1/n_{\text{int}}e\rho = 7000\text{-}10000 \text{ cm}^2/\text{Vs}$. For comparison, this is approximately 60 times lower than graphene's intrinsic mobility at room temperature [58].

In contrast to the intermediate- T behavior, the resistivity at higher $T > 150\text{K}$ is highly non-linear in T , and becomes significantly dependent on n_H , increasing for decreasing n_H (Fig. 5.3b). Similar behavior was observed in graphene [58], where the non-linear $\rho_{xx}(T)$ was attributed to remote interfacial scattering of electrons with polar optical phonons in SiO_2 substrate. However, fitting high temperature resistivity of Bi_2Se_3 devices to the activated form $\rho(T)=\rho_0 \exp(\Delta E/k_B T)$ yields $130 \text{ meV} < \Delta E < 170 \text{ meV}$ depending on n_H , which appears unreasonable for optical phonons of the substrate or Bi_2Se_3 . Moreover, we find that the resistivity between $250 \text{ K} < T < 300 \text{ K}$ shows appreciable hysteresis in temperature, which is likely associated with charge transfer from SiO_2 substrates to the bottom surface or absorption and desorption of F4TCNQ molecules on the top surface of the device. Thus we ascribe the observed non-linear

behavior at $T > 200 \text{ K}$ to an extrinsic contribution to $\rho_{xx}(T)$ whose origin is not yet understood.

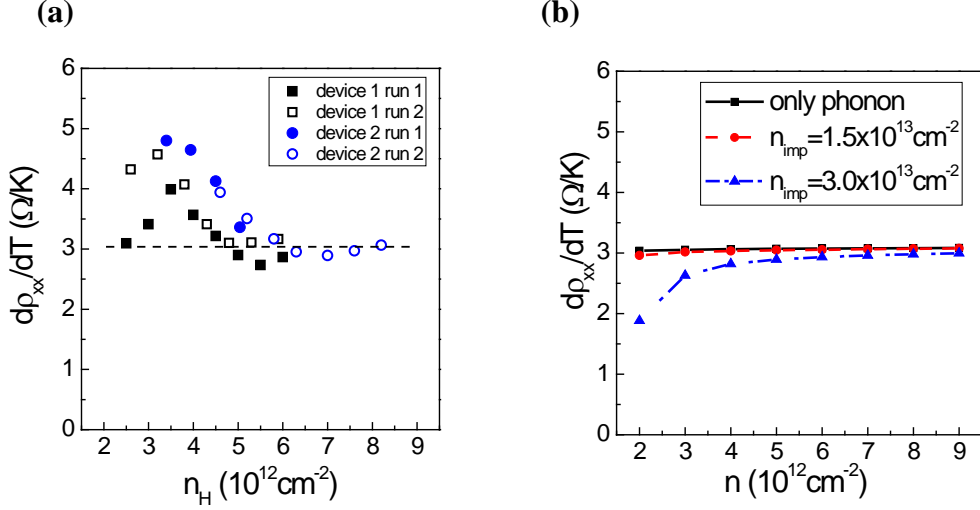


Figure 5.6 Electron-phonon coupling strength. Comparison of experimental and theoretical estimation of electron-phonon coupling strength **(a)** Slope of ρ_{xx} vs. carrier density in the linear temperature regime ($50 \text{ K} < T < 150 \text{ K}$). Dashed line indicates the high carrier density value of the slope used to compare to the theoretical model. **(b)** Calculated slope $d\rho_{xx}/dT$ vs. n in the linear temperature regime ($50 \text{ K} < T < 150 \text{ K}$). The solid line is the result including only electron-phonon scattering, while the dot-dashed and dashed lines correspond to Fig. 5.4 **(a)** and **(b)**, respectively

5.3 Conclusion

In conclusion, I have studied temperature-dependent electronic transport in the topological surface states of Bi_2Se_3 . I find significant activation of carriers from the bulk valence band for Fermi energies near or below the Dirac point, but identify a region of unipolar electron conduction where activation of bulk carriers is negligible. In this regime, the temperature-dependence of the resistivity $d\rho_{xx}/dT$ is relatively independent of carrier density, and is used to extract a ratio of deformation potential to Fermi velocity $D/\hbar v_F = 4.7 \text{ \AA}^{-1}$ which gauges the strength of the intrinsic electron-acoustic phonon interaction in

Bi_2Se_3 . Our combined theoretical-experimental work also provides an accurate estimate for the deformation potential coupling in the Bi_2Se_3 surface carriers to be 15 - 22 eV.

The strong acoustic phonon scattering places an intrinsic limit on the conductivity of the Bi_2Se_3 surface states of $\sim 550 \mu\text{S} = 14 e^2/h$ per surface, approximately 60 times lower than graphene's intrinsic conductivity at room temperature [58]. The highest achievable room temperature mobility is $< 10,000 \text{ cm}^2/\text{Vs}$. Examining Eqn. (5.2), one can see that the large difference between Bi_2Se_3 and graphene comes from the mass density ρ_s , which is much larger in Bi_2Se_3 due to the heavy elements in its composition. Since strong spin-orbit coupling is thought to be necessary to achieve the TI state, necessitating heavy elements, it is likely that any TI will be plagued with much larger electron-phonon resistivity compared to graphene.

Chapter 6 Coherent topological transport on the surface of Bi_2Se_3

The two-dimensional (2D) surface of the three-dimensional topological insulator (TI) is in the symplectic universality class [1] and exhibits perfect weak anti-localization (WAL) reflected in positive weak-field magneto-resistance (MR). In this chapter, I discuss phase coherent transport by measuring MR of gate-tuned, bulk insulating Bi_2Se_3 thin films as a function of film thickness and carrier density. In section 6.1 and 6.2, I briefly introduce WAL phenomena in thin films of TIs and review recent observations of WAL in the non TI regime in the case of coexisting surface and bulk conduction. In the later sections, I concentrate on discussing the main results of this chapter : WAL in the TI regime and multichannel crossovers. For thick samples the magnitude of MR indicates two decoupled (top and bottom) symplectic 2D surfaces. On reducing thickness, I observe first a crossover to a single symplectic 2D channel indicating coherent coupling of top and bottom surfaces via interlayer tunneling, and second a complete suppression of WAL. I show that the first crossover is governed by the ratio of phase coherence time to the inter-surface tunneling time, and the second crossover occurs when the hybridization gap becomes comparable to the disorder strength.

6.1 Phase coherent transport

6.1.1 Weak localization and anti-localization

In the Altland-Zirnbauer symmetry classification [69] the topological insulators belong to the symplectic universality class. This symmetry class is characterized by the presence of time-reversal symmetry. A two dimensional electron gas (2DEG) with strong spin-orbit coupling is also in the symplectic class, as well as graphene in the absence of inter-valley scattering; we refer to these systems as symplectic metals. The symplectic metal is characterized by weak anti-localization (WAL) phenomena.

Weak localization (WL) and WAL describe corrections to the classical electrical conductivity of two-dimensional electron gases due to coherent interference of time-reversed paths [70]. A conventional (non-Dirac) two-dimensional electron gas in the absence of spin-orbit coupling exhibits WL: time-reversed paths which involve multiple scatterers interfere constructively, leading to localization (see Fig. 6.1a). At zero temperature all carriers are localized and the system is insulating. At finite temperature WL leads to a correction to the conductivity which is logarithmic in the temperature.

When a Dirac fermion in TI surface state traverses a loop in space, the spin rotates by 2π due to the spin-momentum locking (see Fig. 6.1b). The wave function, being a spinor, acquires a phase (Berry phase) of π induced by the Dirac point. This phase affects quantum interference, in particular changes the constructive interference of spin-less fermions, which gives rise to enhanced backscattering probability and WL, into destructive interference, which results in suppressed backscattering and WAL. Therefore electrons in a Dirac electronic system cannot be localized by disorder which does not couple to the spin degree of freedom. In graphene, point disorder couples to the

pseudospin, and can localize the electrons. Additionally, higher-order terms in the Hamiltonian of graphene are not symplectic, and graphene shows both WAL and WL behavior. In contrast, the TI surface is protected from disorder that does not break time-reversal symmetry, and in the absence of such disorder may be the unique example of a 2D electron system in the symplectic symmetry class at all timescales, remaining metallic at zero temperature.

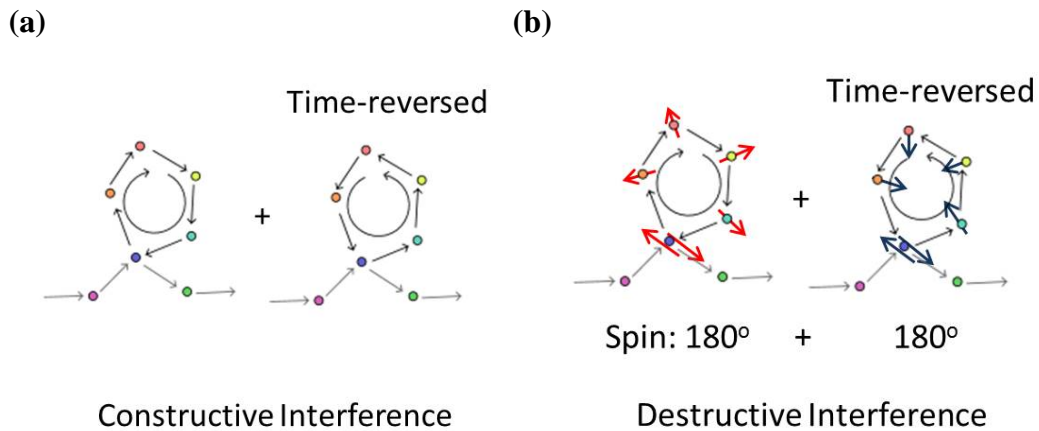


Figure 6.1 Quantum correction due to self-intersecting time reversed loops (a) Enhanced backscattering (constructive interference) of a spin-less electron wave function leading to weak localization (b) Suppressed backscattering (destructive interference) of a Dirac electron by acquiring Berry phase of π leading to weak anti-localization

Experimentally, the observation of WAL is possible by applying perpendicular magnetic field to the sample as shown in Fig. 6.2b. As the applied magnetic field increases, it contributes an Aharonov-Bohm phase to the closed orbits of scattered electrons, reducing the constructive (destructive) interference characteristic of WL (WAL). At very high magnetic fields the sample's conductivity approaches the classical value. In the WAL case, conductivity at zero field is higher than the classical value

because of reduced backscattering probability, thus the sample shows negative magneto-conductance. In their seminal paper, the importance of spin-orbit coupling and the resulting WAL correction to the conductivity was first derived by Hikami, Larkin and Nagaoka in the following form [70].

$$\Delta\sigma(H) = \alpha \frac{e^2}{\pi h} \left[\ln \frac{H_0}{H} - \psi \left(\frac{1}{2} + \frac{H_0}{H} \right) \right] \quad (6.1)$$

where $H_0 = \hbar / 4D_e e\tau_\phi$ is a characteristic field related to the phase coherence time τ_ϕ and diffusion constant D_e , ψ is the digamma function, and α is the overall amplitude whose expected value for a single 2D channel is 1/2.

Eqn. 6.1 is a limiting case of a more general expression derived in Refs. [70] and [71], where the magneto-conductance correction depends on the elastic scattering time τ_e , the phase coherence time τ_ϕ , the spin-flip time τ_{sf} and the spin-orbit scattering time τ_{so} . WAL as described by Eqn. 6.1 with $\alpha = 0.5$ is obtained when $\tau_\phi \gg \tau_{so}$, in which case the first digamma function can be approximated as log function. The samples in this study are assumed to contain no magnetic impurities and therefore τ_{sf} is expected to be infinite. One should also note that the WAL correction to the conductivity was originally derived for conventional 2D electron gases with spin-orbit coupling. The details of the derivation for Dirac fermions are slightly different, but the final answer for the WAL correction is the same, as shown by Suzuura and Ando [72] and McCann et al. [73] in the context of graphene. This is to be expected since the two systems are in the same universality class. (Qualitatively one can imagine that the perfect spin-orbit coupling in the Bi_2Se_3 surface state implies the limit $\tau_{so} \rightarrow 0$ and therefore Eqn 6.1 should be exact.) Therefore I mainly use Eqn. (6.1) throughout this chapter for the description of WAL in Bi_2Se_3 thin films.

6.1.2 Weak anti-localization in topological insulator thin films in multi-channel limit

The above HLN result was derived for a single 2D transport channel, where $\alpha = 0.5$. In TI thin film geometry, however, there can be at most three transport channels: top, bottom, and bulk (effectively 2D in a thin film) if bulk bands are populated. WAL in this multichannel transport regime is sensitive to the competition between the phase coherence time τ_ϕ and other time scales [74]. Charge carriers may scatter into additional conducting channels (from top to bottom surface, or into the conducting bulk), modifying the WAL behavior. The validity of Eqn. (6.1) in the multichannel limit has been addressed in a number of previous studies [74-77], finding that Eqn. (6.1) correctly describes WAL in the presence of multi-channels and coupling between them, though the prefactor α can take on almost any value, and is not limited to multiples of 1/2. Here I summarize the argument for the case of two channels given in Ref. [74].

First consider the case when $\tau_\phi \gg \tau_{ic}$ where τ_{ic} represents characteristic time of inter-channel scattering. In this limit inter-channel mixing rate is so high that the overall WAL is same as that of strongly coupled single channel (Eqn 6.1 with $\alpha = 0.5$). Secondly, consider the opposite limit of $\tau_\phi \ll \tau_{ic}$. In this limit, phase coherence of an electron in one channel is lost before it can scatter into the other channel so that the system shows WAL correction from two independent coherent channels. These two channels could be a bulk and surface, two surfaces, or a surface and a mixed channel such as coherently coupled bulk and the opposite surface. Both the bulk and surface corrections should follow Eqn. 6.1, each with $\alpha = 0.5$. A key component is the logarithmic part, which is an approximation to a digamma function. The total correction for two channels can be written as

$$\Delta\sigma(H) = \alpha \frac{e^2}{\pi h} \left(\left[\ln \frac{H_{01}}{H} - \psi \left(\frac{1}{2} + \frac{H_{01}}{H} \right) \right] + \left[\ln \frac{H_{02}}{H} - \psi \left(\frac{1}{2} + \frac{H_{02}}{H} \right) \right] \right) \quad (6.2)$$

Combining two logarithmic parts, the WAL correction now has exactly the same form of Eqn. 6.1,

$$\Delta\sigma(H) = \alpha \frac{e^2}{\pi h} \left(\left[2 \ln \frac{H_{eff}}{H} - \psi \left(\frac{1}{2} + \frac{H_{01}}{H} \right) - \psi \left(\frac{1}{2} + \frac{H_{02}}{H} \right) \right] \right) \quad (6.3)$$

where the $H_{01,02}$ term is replaced therefore introduce an effective dephasing field $H_{eff} = \sqrt{H_{01}H_{02}}$. Moreover, since the digamma function varies appreciably only for $H < H_{eff}$, in the opposite limit, the modulation with H of the WAL correction is governed by the logarithmic part. Moreover in this limit one can neglect $H_{01,02}$ in the argument of digamma function for $H \gg H_{01,02}$, leading to the final form of WAL,

$$\Delta\sigma(H) = 2\alpha \frac{e^2}{\pi h} \left(\left[\ln \frac{H_{eff}}{H} - \psi \left(\frac{1}{2} \right) \right] \right) \quad (6.4)$$

which is the same as Eqn (6.1) except that the overall coefficient α now becomes $2\alpha=1$. Therefore Eqn (6.1) provides a robust physical description of WAL behavior even in the multichannel limit irrespective of the Drude conductivity of each channel [74, 77]. In this approximation, $\alpha = m/2$ probes the number of channels m .

Previous studies of WAL in TI thin films [39, 74, 75, 77-80] are confined to the non TI regime with a highly conducting bulk channel. Figure 6.2 shows a representative study where the authors considered gate-tuned top surface and mixed bulk plus bottom channels. There the gate tunable surface to bulk scattering is the main source of inter-channel coupling. In this study, they observed that the magnitude of α starts from near 0.5 at zero gate voltage since two channels are strongly coupled by surface to bulk scattering. However continuous increase of α to 1 was observed as the top gating field was increased,

and it was interpreted as crossover from coupled single to two independent coherent channel limit due to formation of depletion layer.

In contrast to the previous studies, I measure WAL in gate-tuned, bulk insulating Bi_2Se_3 thin films where we expect negligible surface-bulk scattering [28]. In this TI regime I show that top and bottom surfaces are relevant transport channels in the system, and inter channel coupling is determined by inter-surface tunneling induced by top and bottom surface hybridization, which I briefly introduce in the next section.

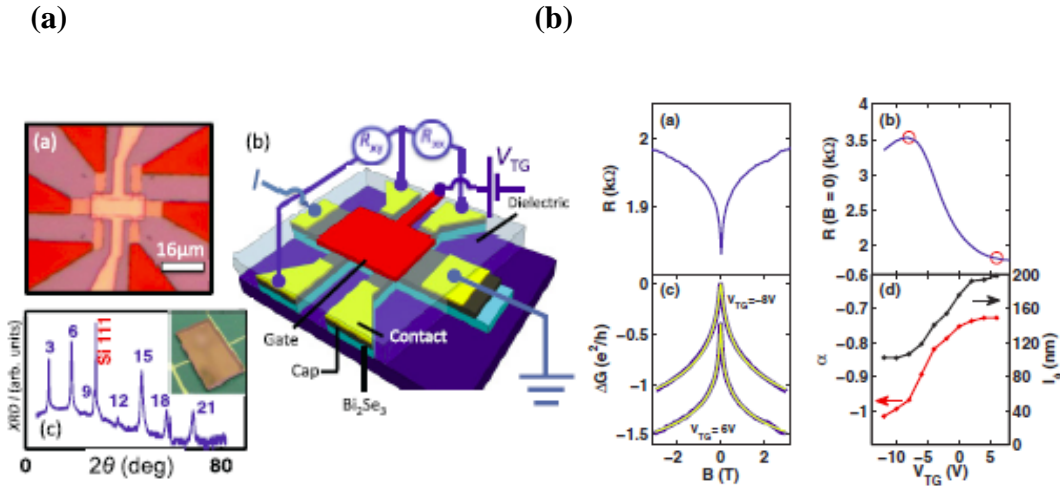


Figure 6.2 Gate tunable coherent coupling of multi-channels in non TI regime (from Ref. [74]). (a) Optical micrograph and schematic of device structure (b) Measured WAL correction and variation of α as a function of top gate voltage V_{TG} .

6.2 Finite size effects in thin films of topological insulators

6.2.1 Inter-layer coupling and band gap opening

Along with p -type doping with external agents, fabrication of thin film geometry is a general approach to realize TI regime. An interesting question is: How thin can

Bi_2Se_3 be while retaining its three-dimensional topological insulator character? The thinnest layer that maintains a 2:3 Bi:Se stoichiometry is the quintuple layer (QL) of five alternating Se and Bi planes, while the thinnest slab which retains the symmetry of bulk Bi_2Se_3 is one unit cell, or three QL units, thick. In Ref. [81], Zhang et al, reported ARPES measurement in 1~6 QL Bi_2Se_3 films as seen in Fig. 6.3. They observed opening an energy gap of surface states in films of thickness below 6 QLs and reported that the gap size increases with decreased number of QLs. This phenomenon can be understood well in terms of inter-surface tunneling. The topological states, strictly localized at the either surface in the case of thick films, can be hybridized when the film becomes only a few QL thin to form symmetric and anti-symmetric eigenstates, where the energy splitting of these combinations are represented by energy gap Δ . Therefore electron state initially localized at one surface can tunnel to the other surface as time evolves.

Opening of an energy gap indicates that ultrathin Bi_2Se_3 films of thickness below 6 QL are not three-dimensional topological insulators. However, there has been numerous theoretical works on ultrathin topological insulator films [8, 82] especially about whether they are topologically trivial or nontrivial, in other words, whether they are conventional insulators or two dimensional topological insulators with gapless spin-full one-dimensional edge states (which cannot be observed with ARPES technique). In a later transport study [83] (Fig. 6.3b), by measuring electronic transport in ultrathin Bi_2Se_3 devices, it was shown that the ultrathin film (3 QL) of 3D TI becomes ordinary insulator with clear insulating behavior indicated by activation energy gaps up to 250 *meV*.

The transport study in Ref. [83] is focused on the effect of energy gap on the semi-classical Drude transport. Likewise, WAL correction in the ultrathin films of TI are significantly affected by hybridization induced inter-surface tunneling and it is nontrivial question whether gapped TI films will still show WAL behavior for strictly speaking, Eqn (6.1) is derived assuming gapless Dirac electron. In a recent theoretical study of WAL in TI thin films, the variation of Berry phase θ_B from π in a gapped TI thin film was derived in the form $\theta_B = \pi(1 - \Delta/2E_f)$ so that the system will show WAL behavior when $\Delta/2E_f \sim 0$ but WAL to WL crossover is expected when $\Delta/2E_f \sim 1$. Experimentally Δ and E_f can be tuned by varying thickness and applying gate voltage to the TI films, respectively.

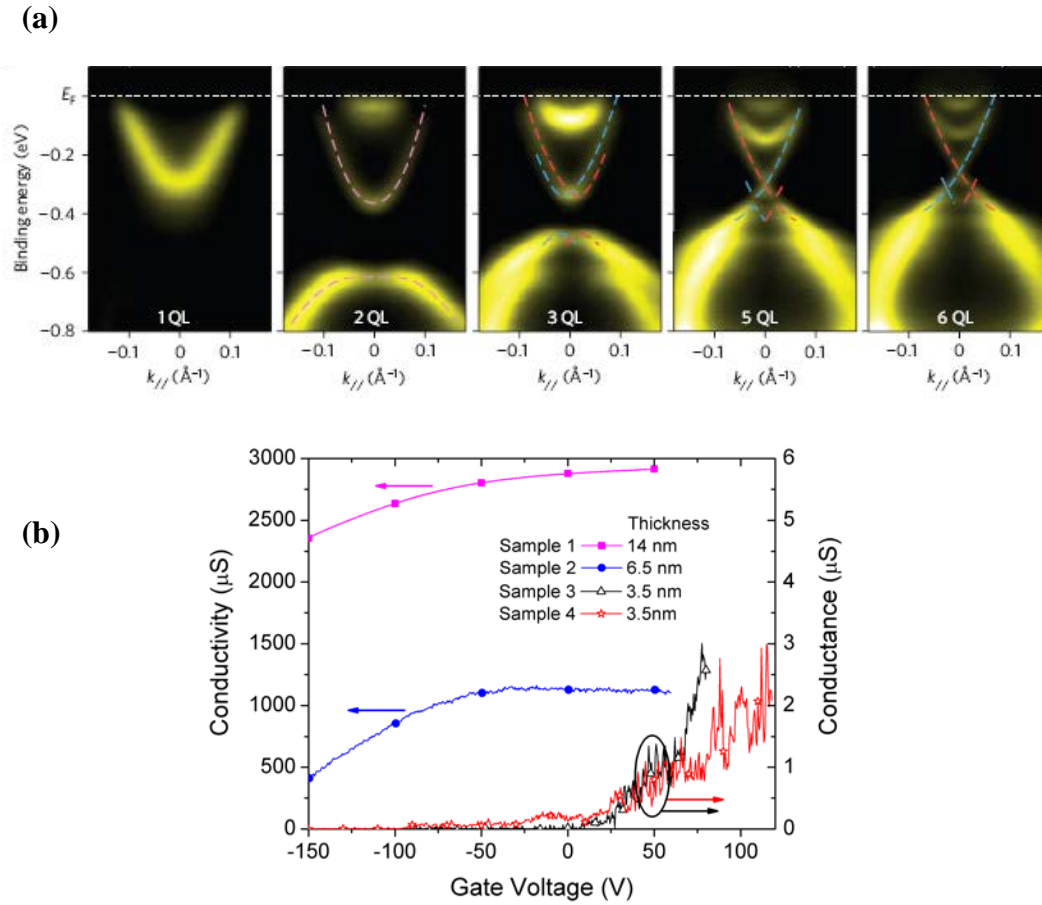


Figure 6.3 ARPES and transport study of opening a band gap in ultrathin Bi₂Se₃ thin films. **(a)** ARPES band structure of MBE grown ultrathin Bi₂Se₃ films. Figure from Ref. [81] **(b)** Insulating behavior observed in the transport study of mechanically exfoliated Bi₂Se₃. Figure from Ref. [83]

6.2.2 Signatures of hybridization induced band gap in gate tuned semi-classical transport

In order to study WAL behavior in TI thin films with varying Δ , I mechanically exfoliated Bi₂Se₃ single crystals ranging in thickness from 5 to 17 quintuple layers (QL=1nm). Figure 6.4a shows a representative device (thickness 12 QL), where height profiles across the width direction of the 17, 12, 7, and 5 QL devices are shown in figure 6.4b. All devices are p-type doped with F4TCNQ organic molecules as described in Chapter 3.

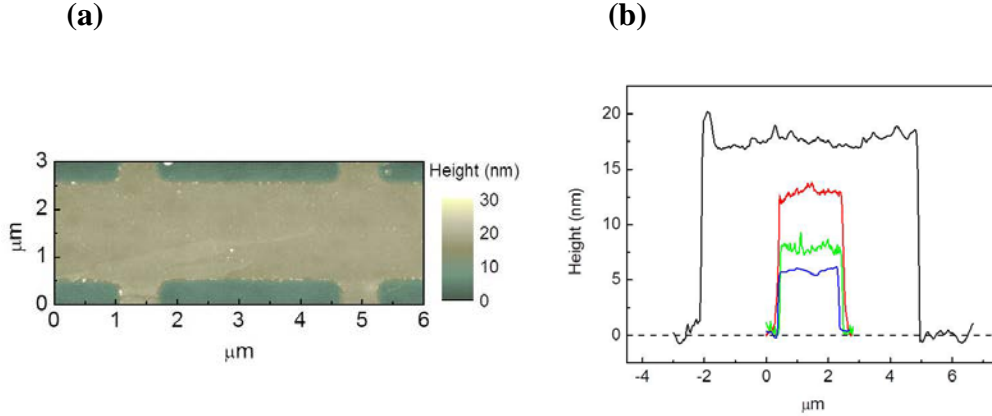


Figure 6.4 (a) AFM image of a 12QL Hall bar device. (b) height profiles of 5,7,12,17QL Bi_2Se_3 thin films.

Figure 6.5a and b show the longitudinal resistivity ρ_{xx} and Hall carrier density $n_H = 1/(eR_H)$ of the devices at a temperature of 2K as a function of back gate voltage V_g . n_H are in the range of $2\text{-}7 \times 10^{12} \text{ cm}^{-2}$ at zero gate voltage hence, as discussed in the chapter 5, the devices are in the TI regime before application of a back gate voltage. Ambipolar electric field effects are indicated by the sharp peak of $\rho_{xx}(V_g)$ and the sign change in n_H at the charge neutrality points ($V_{g,0}$, figure. 1c dashed lines). The dependence of $\rho_{xx}(V_{g,0})$ on temperature T in all of our devices, including 5 QL, shows metallic behavior (see below) which is likely due to conduction through inhomogeneity-driven electron-hole puddles. However the thinnest (5 QL) device shows an anomalously large maximum $\rho_{xx}(V_{g,0})$ of about 23 k Ω which cannot be understood within the self-consistent theory for a Dirac band in the presence of charge disorder [31], suggesting that the inter-surface hybridization gap Δ becomes important in determining the resistivity in this regime. Note that true insulating behavior (divergent ρ_{xx} as $T \rightarrow 0$) is not observed for the 5 QL sample, but was previously observed for 3QL Bi_2Se_3 [83].

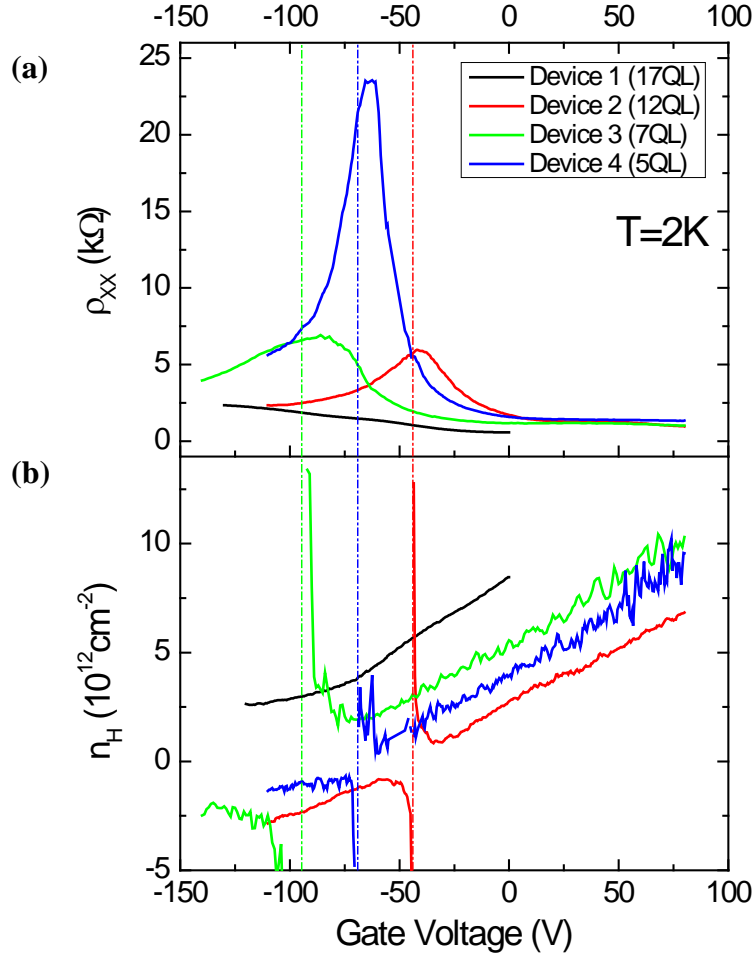


Figure 6.5 Drude transport in thin TI films ranging in thickness from 5 to 17 QL. **(a)** Longitudinal resistivity ρ_{xx} . **(b)** sheet carrier density n_H determined from Hall measurement as a function of back gate voltage at the temperature of 2K.

I first discuss the possible origin of metallic conduction in gapped TI thin films. Figure 6.6a shows $\rho_{xx}(V_g, T)$ of the 5 QL device. The shift of maximum resistivity ρ_{max} (dashed line) is due to thermal activation from bulk valence band when the Fermi level E_f is close to charge neutrality point (Chapter 5). As can be seen in figure 6.6b, ρ_{xx} increases linearly with temperature for $T > 50 K$, which is consistent with the study of gate tuned 10QL Bi_2Se_3 in Chapter 5. The trace of $\rho_{max}(T)$ shows metallic behavior, i.e. $d\rho_{max}/dT >$

0 (inset of Fig. 6.6b). A weak insulating behavior ($d\rho_{\max}/dT < 0$) can be seen for $T < 40$ K for data taken at fixed gate voltage (main panel Fig. 6.6b) but the temperature dependence is much weaker than thermal activation. Similar behavior was observed in MBE grown Bi_2Se_3 thin films and interpreted as electron-electron interaction corrections to the conductivity [84, 85].

The hybridization induced energy gap Δ in few-QL Bi_2Se_3 has been measured in the previous ARPES study [81] (see Fig. 6.3a). Transport experiment shows clearly insulating behavior in 3 QL thick Bi_2Se_3 field effect transistor [83], and an energy gap as large as 250 meV was estimated. However, Δ is expected to decrease exponentially as a function of thickness. Moreover in the presence of finite disorder the surface, although gapped, can conduct through inhomogeneity-driven electron-hole puddles. For the 5 QL device I estimate Δ from the fit to ARPES study to be 34 meV. Previous scanning tunneling microscopy study of disorder driven electron-hole puddles in TIs [53] shows energy fluctuation of about 10~16 meV for doped Bi_2Se_3 with amount of disorder $n_{\text{imp}} 5 \times 10^{12} \text{cm}^{-2}$, which is comparable to $\Delta/2 \sim 17$ meV, and we generally estimate larger n_{imp} in micro-fabricated devices. This is a qualitative comparison only, since the screening will be poor for Fermi energies within the gap, and charge inhomogeneity will always create screening puddles with $E_F > \Delta/2$. However, the fact that the observed disorder scale for ungapped Bi_2Se_3 is comparable to the observed gap Δ is suggestive that the devices should be dominated by inhomogeneity near Dirac point. Therefore I conclude that the observed metallic temperature dependent resistivity in gapped TI thin films is due to conduction through inhomogeneity-driven electron-hole puddles.

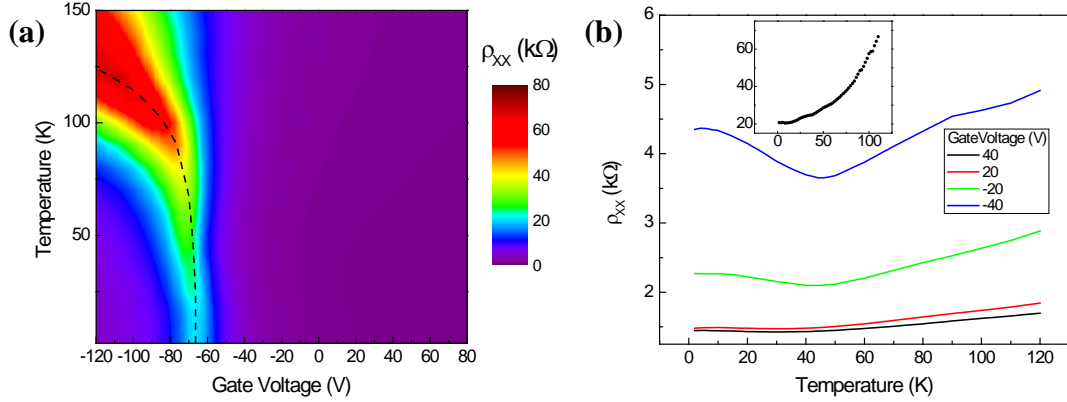


Figure 6.6 Temperature dependent resistivity of 5QL device. **(a)** Longitudinal resistivity ρ_{xx} as a function of gate voltage V_g and temperature T . Dashed curve shows a trace of the position of ρ_{max} . **(b)** ρ_{xx} vs. T at various gate voltages. The inset shows ρ_{max} as a function of T .

6.3 Weak anti-localization in the topological insulator regime

6.3.1 Coherently coupled single channel to multichannel crossovers

I now turn to discuss gate-tuned WAL behavior in the TI regime. Figure 6.7 shows the magneto-conductivity $\Delta\sigma(H)$ for all four devices. Curves are taken at similar carrier density $n = C_g(V_g - V_{g,0})/e$ (where gate capacitance $C_g \approx 11 \text{ nF cm}^{-2}$) ranging from $\approx 7 \times 10^{12} \text{ cm}^{-2}$ (n -type) to $-2 \times 10^{12} \text{ cm}^{-2}$ (p -type) except for the 17 QL device where only n -type carrier density (7 and $2 \times 10^{12} \text{ cm}^{-2}$) could be observed due to relatively high initial doping. The data for the entire range of n and thickness can be fitted (dashed curves in Fig. 6.7) well with Eqn. 6.1, as expected from the discussion in the Section 6.1.

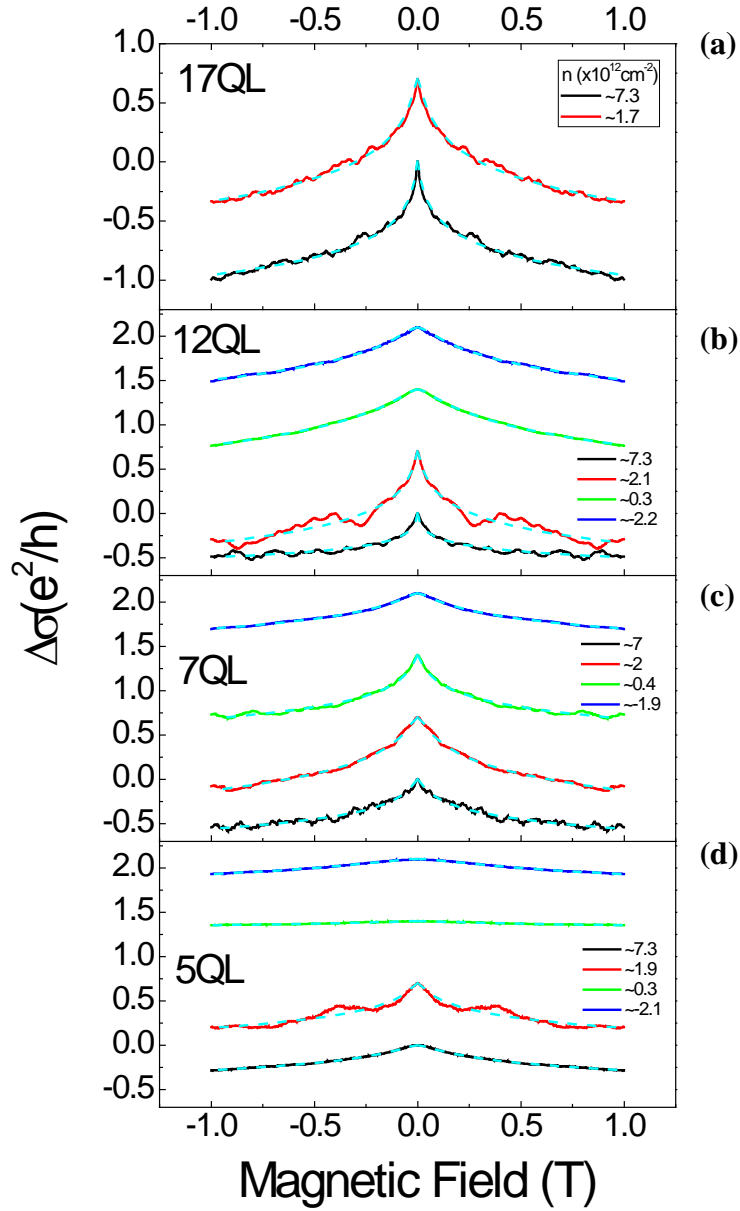


Figure 6.7 Weak anti-localization in the topological insulator regime. Magnetoconductivity $\Delta\sigma$ as a function of perpendicular magnetic field H in (a) 17, (b) 12, (c) 7, and (d) 5QL devices measured at 2 K at gate-induced carrier densities indicated in the legends. Dashed curves show least-square fits to Eqn. 6.1. Zeros of all curves are offset by $0.7 e^2/h$ for clarity.

Figure 6.8 shows the variation of α obtained from the fit to Eqn. 6.1 as a function of n for 17 (black), 12 (red), 7 (green), and 5 (blue) QL devices measured at 2 K. In all devices α is close to 1/2 at high $n \approx 8 \times 10^{12} \text{ cm}^{-2}$, which can be interpreted as WAL in a single strongly coupled coherent channel. However, the behavior of α upon gate tuning shows very different behaviors depending on the thickness of the devices. The thickest device (17 QL) shows WAL consistent with two decoupled top and bottom topological surfaces ($\alpha \approx 1$) starting at moderate $n \approx 6 \times 10^{12} \text{ cm}^{-2}$, maintained down to the minimum accessible n . I do not rule out the possible contribution of bulk-surface scattering in 17 QL at high n since at this high n bulk carriers starts to be populated and the surface to bulk scattering will dominate inter-channel coupling. However, at low n , in particular near Dirac point, surface to bulk scattering is negligible so that gate-tuned surface to bulk scattering cannot explain the general behavior of α for low n and thinner devices. Notably, I identify two crossovers in the 12 QL device: I observe sharp transition of α from $\approx 1/2$ to ≈ 1 near $n \approx 1 \times 10^{12} \text{ cm}^{-2}$ (n -type), and back to 1/2 at $n \approx -1 \times 10^{12} \text{ cm}^{-2}$ (p -type). $\Delta\sigma(H)$ in the present devices include a moderate contribution from (universal) conductance fluctuations (Fig. 6.7), as commonly observed in micro-fabricated Bi_2Se_3 devices. However I repeated similar WAL measurements at 2 K for the 12 QL device on five different thermal runs, where the conductance fluctuation contribution is randomized, and find that the crossovers are reproducible within the experimental uncertainty (Fig. 6.8, error bars). This transition is absent in the 7 QL device where WAL in the entire range of n indicates a strongly coupled single channel ($\alpha \approx 1/2$). Finally, at an even smaller thickness (5QL), I observe strong suppression of WAL for $-1 \times 10^{12} \text{ cm}^{-2} < n < 1 \times 10^{12} \text{ cm}^{-2}$, (inset of Fig. 6.8, see also Fig. 6.7).

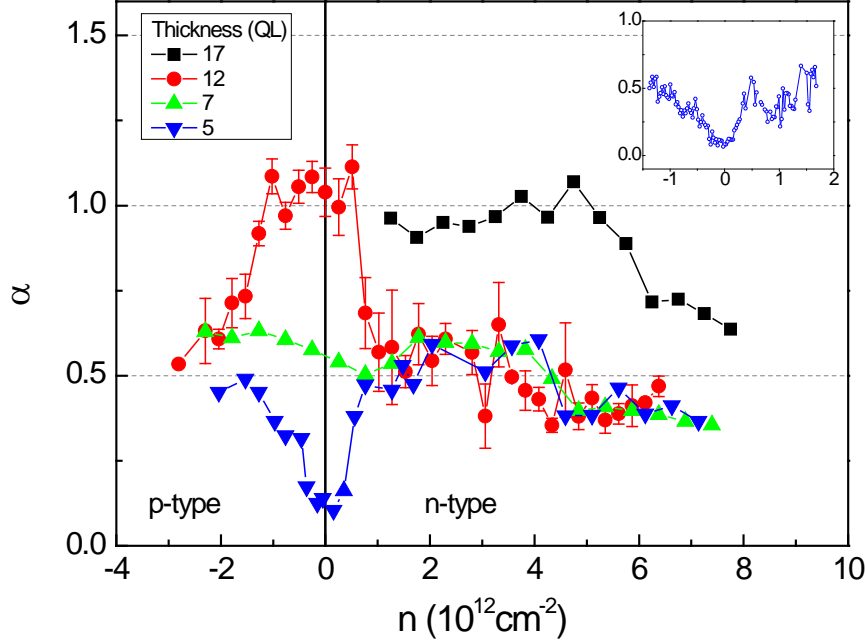


Figure 6.8 Coupled / decoupled coherent transport in Bi_2Se_3 surface states. Variation of the amplitude of weak anti-localization α as a function of 2D carrier density n for 17 (black square), 12 (red circle), 7 (green triangle), and 5 QL (blue triangle) thick devices measured at 2K. For the 12 QL device, the error bars show standard deviations determined from WAL measurements taken at five different thermal runs. The inset shows detailed behavior of suppression of WAL for 5 QL at small n .

6.3.2 Physical origin of the crossovers

I now examine the coherence time τ_ϕ and compare to the estimated interlayer tunnel time τ_t . We estimate $\tau_\phi = \hbar / 4eD_e H_0$ from the fits to Eqn. 6.1 and using $D_e = \tau v_f^2 / 2$ where Fermi velocity $v_f \approx 3 \times 10^7 \text{ cm/s}$ for Bi_2Se_3 [38], and the momentum relaxation time τ is calculated from the measured $\sigma(n)$ using Drude model. τ_t represents the characteristic time of transition (half the period Rabi oscillations) between localized states in two quantum wells with energy splitting Δ , thus $\tau_t = \hbar / 2\Delta$. Figure 6.9 shows experimentally measured (open circles) and theoretically predicted (open triangles) Δ as

functions of thickness in QL [86]. As shown in figure 6.9, theoretical calculations of finite size effects in Bi_2Se_3 predict systematically smaller Δ at a given thickness and also suggest that Δ shows oscillatory decaying behavior, which do not seem to be observed in the previous work or this work. Considering experimental uncertainty in ARPES measurement, I examined range of $\Delta(t)$ by including (1) sizable Δ in 2,3,4,and 5QL (upper bound) and (2) all data from 2 to 8QL (lower bound) in the fit and obtain $\Delta(t)=[992 \text{ meV}]e^{-0.67[t \text{ (nm)}]}$ and $\Delta(t)=[879 \text{ meV}]e^{-0.62[t \text{ (nm)}]}$. The resultant range of Δ is 34.8~39.5, 9.1~11.44, 0.32~0.51, and 0.01~0.02 meV for 5, 7, 12, and 17 QL, respectively.

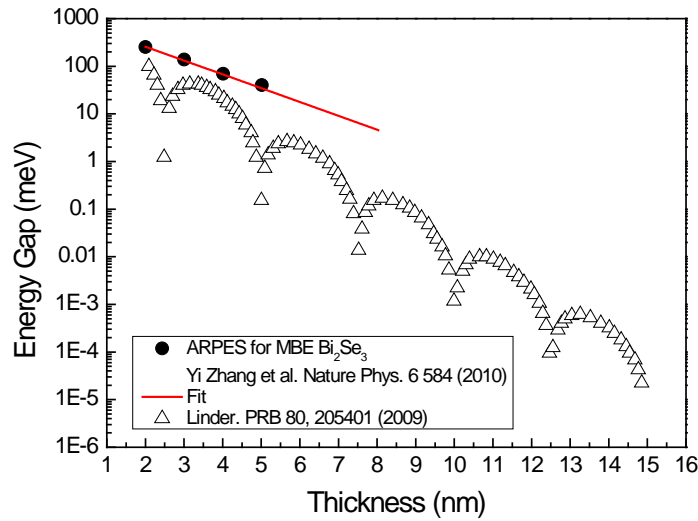


Figure 6.9 Comparison of experimentally measured and theoretically predicted hybridization induced surface gap Δ in Bi_2Se_3 . Solid circles are ARPES data from Ref. [81] and open triangles are theoretical calculation from Ref. [86]

Figure 6.10 shows the estimated τ_ϕ and τ_t as functions of n for the different thickness samples. Upon gate tuning, τ_ϕ changes by an order of magnitude ranging from ≈ 4 to $\approx 50 \text{ ps}$, and shows a sharp dip near $n = 0$ (Dirac point). For the 17 QL device, τ_ϕ/τ_t

$\ll 1$ in the entire range of n . In this limit electrons on either surface lose coherence before scattering to the other, thus each surface acts as an independent coherent transport channel and $\alpha \approx 1$. In contrast a crossover occurs from $\tau_\phi/\tau_t \gg 1$ at high unipolar n - and p -type carrier densities to $\tau_\phi/\tau_t < 1$ near $n = 0$ in the 12 QL device, which is consistent with the observed crossover from $\alpha = 1/2$ to $\alpha = 1$ (Fig. 6.8). In the thinner device (7 QL), the condition $\tau_\phi/\tau_t \gg 1$ is satisfied, and the two surfaces are strongly coupled ($\alpha \approx 1/2$) for the entire range of n . Although generally estimation of τ_ϕ becomes inaccurate at $n = 0$ due to charge inhomogeneity, the comparison of τ_ϕ/τ_t in different thicknesses provides reasonable explanation on the physical origin of the crossovers in number of coherent channels.

The behavior described above is in general consistent in the 5 QL device except near the Dirac point, where WAL is strongly suppressed. The suppression of WAL can be understood in terms of the expected change of Berry phase $\theta_B = \pi(1 - \Delta/2E_f)$ in TIs as a function of Δ and the Fermi energy E_f [39]; θ_B is reduced from π when hybridization induced gap opens. Assuming a gapped Dirac dispersion $E_F = \sqrt{(\hbar v_F k_F)^2 + (\Delta/2)^2}$, I estimate $E_f \leq 52 \text{ meV}$ and $\theta_B \leq 0.67\pi$ at $|n| \leq 1 \times 10^{12} \text{ cm}^{-2}$. This range of n is comparable to the electron-hole puddle density $n^* \approx 0.5 \times 10^{12} \text{ cm}^{-2}$ per surface (Fig. 6.5b) hence transport occurs through a landscape of electron and hole puddles with θ_B spanning the entire range $0 \leq \theta_B \leq \pi$. It appears that in this regime of highly inhomogeneous Berry phase that both WAL and WL (expected as $\theta_B \rightarrow 0$) are suppressed. I note that similar suppression of WAL was recently observed in thin epitaxial Bi_2Se_3 of varying thickness (and Δ) but fixed E_f [39], and a competition between WAL and WL was observed in gated 4 QL epitaxial $(\text{Bi}_{0.57}\text{Sb}_{0.43})_2\text{Te}_3$ [87]. The observation of the WAL by tuning both

E_f (by gate-tune) and Δ (by varying thickness) allows one to identify the ratio of τ_ϕ/τ_t as the driver for the crossover between coupled and decoupled surfaces, and the ratio of Δ to disorder strength as the driver for the crossover to the regime of suppressed WAL/WL.

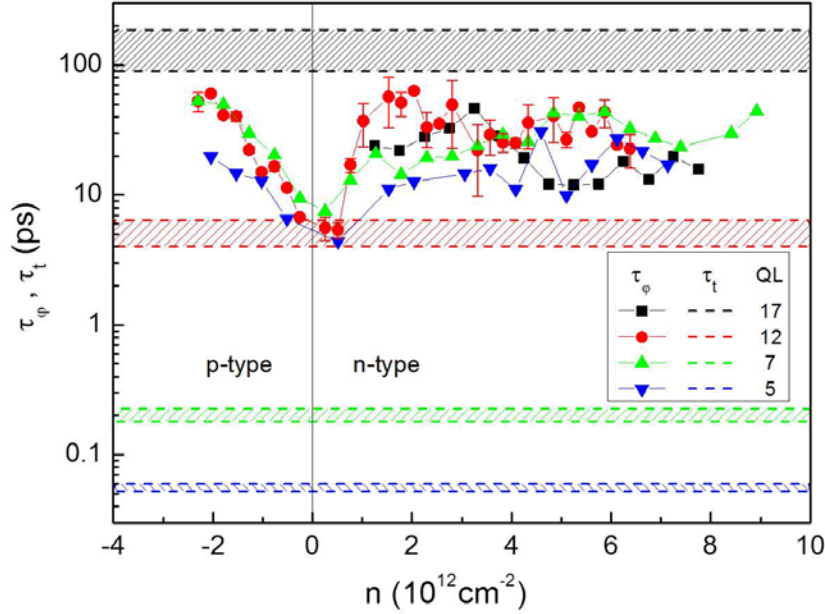


Figure 6.10 Phase coherence time (τ_ϕ) vs. interlayer tunneling time (τ_t). Comparison of phase coherence time τ_ϕ determined from fit to Eqn. 6.1 and transport scattering time to interlayer tunneling time τ_t estimated from surface hybridization induced energy gap Δ as a function of 2D carrier density n . Symbols are experimentally measured τ_ϕ for 17 (black square), 12 (red circle), 7 (green triangle), and 5 QL (blue triangle) devices. The hatched areas with corresponding colors show estimated windows of inter-surface tunneling time τ_t .

6.4 Conclusion

In contrast to semi-classical Boltzmann transport in Bi_2Se_3 TI films, where the signature of finite size effect appear only in the ultrathin limit ($\leq 3\text{QL}$), phase coherent transport offers an exquisitely sensitive probe of the hybridization of top and bottom transport channels. I find that the WAL behavior in TI regime is governed by the ratio of τ_ϕ/τ_t ,

displaying crossovers in number of coherent transport channels depending on the thickness and carrier density. For thick films, $\tau_\phi/\tau_t < 1$ and I observe WAL according to HLN formula with $\alpha = 1/2 + 1/2 = 1$ corresponding to two decoupled TI surfaces each with $\alpha = 1/2$. A thickness and doping-dependent crossover is observed when $\tau_\phi/\tau_t > 1$ to a regime where $\alpha = 1/2$, indicating the coherent coupling of two TI surfaces. The result shows that WAL can detect a gap Δ as small as 0.3 meV in the 12 QL TI film. In our mechanically exfoliated Bi_2Se_3 thin films, τ_ϕ fall in the range of $4\text{ps} < \tau_\phi < 50\text{ps}$, and thickness as thick as 12QL shows single 2D behavior except at low carrier density. Since τ_t is primarily determined from the thickness of Bi_2Se_3 thin films whereas τ_ϕ can vary significantly depending on the sample quality, we expect that the 2D to 3D crossover thickness is not universal but can occur in different thickness if surface phase coherence can be modified. For instance, decreasing phase coherence of the surface electrons by addition of magnetic impurities should result in a reduced critical thickness above which decoupled coherent transport can be observed.

I also find that destruction of topological protection occurs in the few QL film when Δ becomes comparable to disorder strength, which was the case of 5QL device in the present work. For this device, Berry's phase is completely randomized at low carrier density causing the suppression of WAL and WL, reflecting the loss of topological protection for strongly coupled surfaces. We expect that these results are important in identifying the regimes of carrier density and film thickness in which effects related to topological coherent transport can be observed in thin topological insulator films.

Chapter 7 Conclusion and outlook

In this thesis, by reducing n -type doping by applying novel p -type doping agents, I have shown that it is possible to observe surface dominant transport in Bi_2Se_3 . The successful achievement of TI regime opened new opportunities in addressing fundamental transport properties of surface electrons, and I summarize below the three main conclusion of this thesis.

(1) Like graphene, the topological Dirac surface transport shows gapless, ambipolar, and metallic surface conduction properties. By using the existing theoretical predictions, I have shown that the charge transport of surface Dirac electrons in the current Bi_2Se_3 thin films at low temperatures are limited by the presence of charged impurities, showing expected behavior of linear $\sigma(n)$ away from Dirac point as well as minimum conductivity that is self-consistently determined electron hole puddle density driven by charge disorder in the system. For present devices (and arguably for all currently existing Bi_2Se_3 thin film samples) the level of charged impurity disorder is in the order of $\sim 10^{13} \text{ cm}^{-2}$ limiting the mobility to the order of $\sim 1000 \text{ cm}^2/\text{Vs}$.

(2) I have addressed the problem of electron-acoustic phonon scattering in TI regime. I have first showed that gate tuned carrier density is strongly temperature dependent due to thermal activation of carriers from a massive bulk band into the Dirac surface state for Fermi energies near the Dirac point, but there is negligible activation of bulk carriers for Fermi energies well into the surface state conduction band. There I observe linear $\rho_{xx}(T)$, which is characteristic metallic conduction due to electron phonon

scattering at high temperature. In collaboration with Qiuzi Li and Sankar Das Sarma, we have shown that for Fermi energies near the conduction band edge the ratio of deformation potential to Fermi velocity is $D/\hbar v_f = 4.7 \text{ \AA}^{-1}$, which limits highest achievable surface conductivity and mobility at room temperature of $550 \mu\text{S}$ and $10000 \text{ cm}^2/\text{Vs}$, respectively.


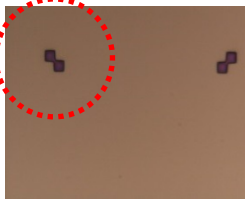

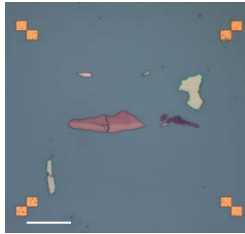
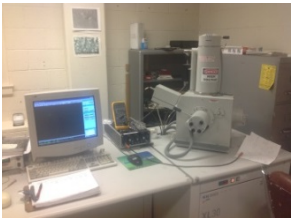


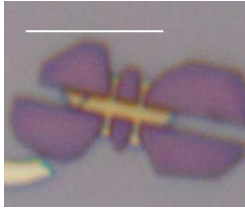
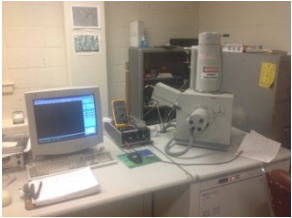
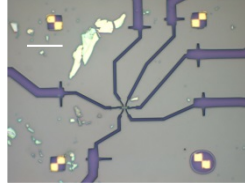
(3) I have addressed effect of hybridization induced gap on WAL in the TI regime. When Δ is small compared to the disorder strength the TI film exhibit WAL that can be described by classical HLN formula, where the channel number crossovers were determined by the ratio τ_ϕ/τ_t . It was found that only for $> 17\text{QL}$ the signature of perfect weak anti-localization can be observed in quantitative agreement with two decoupled surfaces in the symplectic symmetry class while the surfaces of a $< 17\text{QL}$ TI film may remain coherently coupled even for thicknesses as large as 12 QL . On the other hand when Δ becomes comparable to disorder strength, Berry's phase is completely randomized at low carrier density causing the suppression of WAL and WL, reflecting the loss of topological protection for strongly coupled surfaces.

Apart from p-type doping methods introduced (including substitution with Ca or Sb and the method I developed in this thesis), there has been significant progress by other groups in achieving surface dominant transport, such as TI ternary compound of $\text{Bi}_2\text{Te}_2\text{Se}$ [88], and it appears that the TI regime can be routinely accessible in the current transport studies as of 2013. However the currently available methods for achieving TI regime rely on compensation doping rather than removing the source of initial doping. Thus, as pointed out in the first conclusion of my thesis, the surfaces of currently

available 3D topological insulators are extremely dirty, which strongly limits surface mobility. Understanding and eliminating the doping presently observed in all thin crystals and films is of central importance to increasing the mobility of the topological surface state.

Using currently available samples with moderate surface quality, the fields are gradually moving to experimentally confirming novel transport properties that topological Dirac electron are predicted to show such as anomalous spin valve effect due to spin-momentum locking [89], Dirac electron mediated magnetism in magnetically doped TIs [23], and inducing super-current by proximity effects [18, 90]. Although this thesis is confined to charge transport of a representative 3D TI, I believe that the clear surface transport demonstrated and understood here will serve as basis for future studies.

Appendix A. Summary of device fabrication process and recipes

Process	Equipment	Recipe	Product (scale bar : 20 μ m)
Align marker lithography	<p>JEOL XL-30 SEM</p> 	<p>Spin coat:</p> <ol style="list-style-type: none"> MMA 4000rpm, 50sec PMMA 6000rpm, 50sec <p>Pre-Baking: 150°C, 10min</p> <p>E-beam writing Dose: 170 μC/cm²</p> <p>Develop: MIBK:IPA Rinse: IPA</p>	
Align marker deposition	<p>Thermal Evaporator</p> 	<p>Materials & deposition:</p> <ol style="list-style-type: none"> Cr : 2 x 10⁻⁶ Torr, 5nm Au : 2 x 10⁻⁶ Torr, 50nm <p>Lift-off : Acetone 2 hrs. Rinse: IPA</p>	
Hall bar pattern lithography	<p>JEOL XL-30 SEM</p> 	<p>Spin coat:</p> <ol style="list-style-type: none"> PMMA 6000rpm, 50sec <p>Pre-Baking: 150°C, 10min</p> <p>E-beam writing Dose: 175 μC/cm²</p> <p>Develop: MIBK:IPA=1:3 45sec</p> <p>Rinse: IPA</p>	 <p>Etching Areas</p>
Hall bar dry etching	<p>Technics PE-IIA etcher</p> 	<p>Chamber clean: Ar ~300mT, 300W, 3min</p> <p>Etching: Ar ~70mT, 50W, 40sec</p> <p>Remove mask : Acetone Rinse: IPA</p>	
Electrode pattern lithography	<p>JEOL XL-30 SEM</p> 	<p>Spin coat:</p> <ol style="list-style-type: none"> MMA 4000rpm, 50sec PMMA 6000rpm, 50sec <p>Pre-Baking: 150°C, 10min</p> <p>E-beam writing Dose: 170 μC/cm²</p> <p>Develop: MIBK:IPA=1:3 35sec</p>	



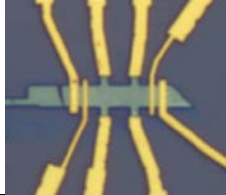
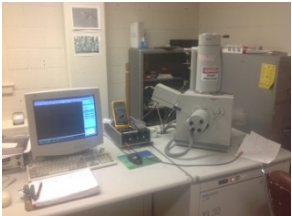
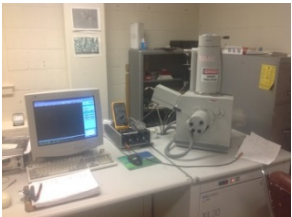
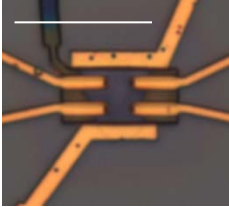

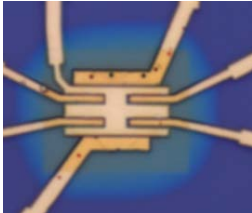
Contact area plasma treatment	Technics PE-IIA etcher 	Chamber clean: Ar ~300mT, 300W, 3min Etching: Ar ~200mT, 50W, 5~10sec	Enhanced Ohmic conduction
Electrode metal deposition	Thermal Evaporator 	Materials & deposition: 1. Cr $\sim 7 \times 10^{-7}$ Torr ~5nm 2. Au $\sim 7 \times 10^{-7}$ Torr ~60nm Lift-off : Acetone 2 hrs. Rinse: IPA	final device – single gate 
(Optional) Top gate dielectric lithography	JEOL XL-30 SEM 	Spin coat: 1. HSQ(6%) 6000rpm, 50sec, thickness : 60nm Pre-Baking: 170°C, 10min E-beam writing Dose: 400 $\mu\text{C}/\text{cm}^2$ Develop: MF26, 240sec Rinse: DI water	HSQ dielectric layer on Bi ₂ Se ₃ device
(Optional) Top gate electrode lithography	JEOL XL-30 SEM 	Spin coat: 1. MMA 4000rpm, 50sec 2. PMMA 6000rpm, 50sec Pre-Baking: 150°C, 10min E-beam writing Dose: 170 $\mu\text{C}/\text{cm}^2$ Develop: MIBK:IPA=1:3 35sec	
(Optional) Top gate electrode deposition	Thermal Evaporator 	Materials & deposition: 1. Cr $\sim 7 \times 10^{-7}$ Torr ~5nm 2. Au $\sim 7 \times 10^{-7}$ Torr ~60nm Lift-off : Acetone 2 hrs. Rinse: IPA	final device – dual gate 

Table A.1 Bi₂Se₃ field effect device fabrication process.

Appendix B. *Mathematica* codes for numerical calculations

1. Calculation of self-consistently determined electron-hole puddle density and minimum conductivity.

(* This program numerically calculates electron-hole puddle density and minimum conductivity, based on the theory S.Adam et al PNAS (2009) *)

```

g = 1; (* degeneracy factor in Bi2Se3 *)
rs = 0.087; (* Wigner-Seitz radius (interaction parameter in Bi2Se3) *)
d = 10 × 10-8; (* distance between charged impurities and Bi2Se3 surface *)

kf[n_] :=  $\sqrt{\frac{4 \pi n}{g}}$ ; (* Fermi wave vector *)

y[n_] := n/ni;
ε[q_, n_] := Piecewise[{{1 +  $\frac{g kf[n] rs}{q}$ , q < (2) kf[n]}, {1 +  $\frac{\pi rs}{2}$ , q ≥ (2) kf[n]}}];

(* dielectric function in RPA approximation, derivation given in PNAS (2009) *)
Crpa[n_] :=  $\frac{g}{2} rs^2$  NIntegrate[ $\frac{e^{-2qd}}{q (\epsilon[q, n])^2}$ , {q, 0, ∞}, MaxRecursion → 30]

Do[ni = i 4 × 1012;
  nstar = 1010; While[Abs[y[nstar] - Crpa[nstar]] > 10-4, nstar = Crpa[nstar] ni]; omin[i] = 201 (nstar/ni);
  nst[i] = nstar, {i, 1, 50}] (*numerical iteration to find electron hole puddle density (nst)
  and minimum conductivity (omin) at given charged impurity density *)
omindata = Table[{i 4 × 1012, omin[i]}, {i, 1, 50}];
nstardata = Table[{i 4 × 1012, nst[i]}, {i, 1, 50}];

```

2. Temperature dependent gate tuned 2D carrier density in Bi₂Se₃.

```

g = 1;

(*degeneracy factor*)
vF = 3 × 107; (*Fermi velocity*)
ħ = 6.58211928 × 10-16; (*Planck's constant*)
eVperJ = 1.602 × 10-19;
k = 8.617 × 10-5; (*Boltzmann constant*)
s0 = -0.06; (*Bulk valence band edge*)
mstar = 2.6 × 9.10938188 × 10-31; (*Bulk effective mass*)
mstars = 0.3 × 9.10938188 × 10-31; (*Surface effective mass*)
t = 13 × 10-7; (*Surface effective mass*)
FD[s_, sF_, T_] :=  $\frac{1}{1 + e^{(s - s_F)/(kT)}}$ 
k[s_] :=  $\frac{1}{\hbar^2} 0.8333333333 \left( -7.49063670411985 \cdot \hbar^{14} mstars v_F + 1.2239801227242092 \cdot \hbar^{15} \sqrt{3.745318352059925 \cdot \hbar^2 mstars^2 v_F^2 + 12 \cdot \hbar^2 mstars s} \right)$ 

Db[s_] := Piecewise[{{ $\frac{t}{2\pi^2} \frac{1}{eVperJ^{3/2} \cdot 10^6} \sqrt{\frac{-(s - s_0)}{\left(\frac{\hbar^2}{2 mstar}\right)^3}}$ , {s < s0}}, {0, {s > s0}}]; (*Bulk density of states *)
Ds[s_] := Abs $\left[ \frac{k[s]}{2\pi} \frac{1}{\frac{10^4 eVperJ \hbar^2 k[s]}{mstars} + \hbar v_F} \right]$ ; (*Surface density of states*)

Dt[s] := Ds[s] + Db[s];

ne[sF_, T_] := NIntegrate[Dt[s] FD[s, sF, T], {s, 0, ∞}]
nh[sF_, T_] := NIntegrate[Dt[s] (1 - FD[s, sF, T]), {s, -∞, 0}]
nt[sF_, T_] := ne[sF, T] - nh[sF, T]
ns[sF_, T_] := NIntegrate[Ds[s] FD[s, sF, T], {s, 0, ∞}] - NIntegrate[Ds[s] (1 - FD[s, sF, T]), {s, -∞, 0}]
nb[sF_, T_] := NIntegrate[Db[s] FD[s, sF, T], {s, 0, ∞}] - NIntegrate[Db[s] (1 - FD[s, sF, T]), {s, -∞, 0}]

Ef[sF_, T_] := ħ vF  $\sqrt{\frac{4\pi nt[sF, T]}{g} + eVperJ 10^4 \frac{\hbar^2 4\pi nt[sF, T]}{2 mstar}}$ 

(*Obtain carrier density dependent Fermi level *)
Do[Do[sol = FindRoot[Re[nt[x, T] / (5 × 1011)] == i, {x, 0}]; sF[i, T] = x /. sol, {i, -5, 8, 1}], {T, 2, 250, 20}]

(*Calculate 2D carrier density based of Ef and store data *)
eftable = Flatten[Table[{(i × (100 / (7.2 × 0.83)) - 45), T, sF[i, T]}, {i, -5, 8, 1}, {T, 2, 250, 20}], 1];
ListContourPlot[%, ContourLabels → Function[{x, y, z}, Text[Framed[z], {x, y}, Background → White]]]
nstable = Flatten[Table[{(i × (100 / (7.2 × 0.83)) - 45), T, ns[sF[i, T], T] / (5 × 1011)}, {i, -5, 8, 1}, {T, 2, 250, 20}], 1];
ListContourPlot[%, Contours → 12, ContourLabels → Function[{x, y, z}, Text[Framed[z], {x, y}, Background → White]]]

```

Bibliography

1. Hasan, M.Z. and C.L. Kane, *Colloquium: Topological insulators*. *Rev. Mod. Phys.*, 2010. **82**(4): p. 3045-3067.
2. Zhang, H., et al., *Topological insulators in Bi_2Se_3 , Bi_2Te_3 and Sb_2Te_3 with a single Dirac cone on the surface*. *Nature Phys.*, 2009. **5**(6): p. 438-442.
3. Laughlin, R.B., *Quantized Hall conductivity in two dimensions*. *Phys. Rev. B*, 1981. **23**(10): p. 5632-5633.
4. Thouless, D.J., et al., *Quantized Hall Conductance in a Two-Dimensional Periodic Potential*. *Phys. Rev. Lett.*, 1982. **49**(6): p. 405-408.
5. von Klitzing, K., *Developments in the quantum Hall effect*. *Philos. Trans. Royal Society a- Math. Phys. and Eng. Sciences*, 2005. **363**(1834): p. 2203-2219.
6. Fu, L., C.L. Kane, and E.J. Mele, *Topological Insulators in Three Dimensions*. *Phys. Rev. Lett.*, 2007. **98**(10): p. 106803.
7. Kane, C.L. and E.J. Mele, *Z_2 Topological order and the quantum spin Hall effect*. *Phys. Rev. Lett.*, 2005. **95**(14): p. 146802.
8. Bernevig, B.A. and S.-C. Zhang, *Quantum Spin Hall Effect*. *Phys. Rev. Lett.*, 2006. **96**(10): p. 106802.
9. Kane, C.L. and E.J. Mele, *Quantum Spin Hall Effect in Graphene*. *Phys. Rev. Lett.*, 2005. **95**(22): p. 226801.
10. Bernevig, B.A., T.L. Hughes, and S.-C. Zhang, *Quantum Spin Hall Effect and Topological Phase Transition in HgTe Quantum Wells*. *Science*, 2006. **314**(5806): p. 1757-1761.
11. König, M., et al., *Quantum Spin Hall Insulator State in HgTe Quantum Wells*. *Science*, 2007. **318**(5851): p. 766-770.
12. Brune, C., et al., *Spin polarization of the quantum spin Hall edge states*. *Nature Phys.*, 2012. **8**(6): p. 485-490.
13. Chen, Y.L., et al., *Experimental Realization of a Three-Dimensional Topological Insulator, Bi_2Te_3* . *Science*, 2009. **325**(5937): p. 178-181.
14. Wallace, P.R., *The Band Theory of Graphite*. *Phys. Rev.*, 1947. **71**(9): p. 622-634.
15. Hsieh, D., et al., *A tunable topological insulator in the spin helical Dirac transport regime*. *Nature*, 2009. **460**(7259): p. 1101-1105.

16. Moore, J.E., *The birth of topological insulators*. *Nature*, 2010. **464**(7286): p. 194-198.
17. Garate, I. and M. Franz, *Inverse Spin-Galvanic Effect in the Interface between a Topological Insulator and a Ferromagnet*. *Phys. Rev. Lett.*, 2010. **104**(14): p. 146802.
18. Fu, L. and C.L. Kane, *Superconducting Proximity Effect and Majorana Fermions at the Surface of a Topological Insulator*. *Phys. Rev. Lett.*, 2008. **100**(9): p. 096407.
19. Hsieh, D., et al., *A topological Dirac insulator in a quantum spin Hall phase*. *Nature*, 2008. **452**(7190): p. 970-974.
20. Moore, J., *Topological insulators: The next generation*. *Nature Phys.*, 2009. **5**(6): p. 378-380.
21. Xia, Y., et al., *Observation of a large-gap topological-insulator class with a single Dirac cone on the surface*. *Nature Phys.*, 2009. **5**(6): p. 398-402.
22. Hsieh, D., et al., *Observation of time-reversal-protected single-Dirac-cone topological-insulator states in Bi_2Te_3 and Sb_2Te_3* . *Phys. Rev. Lett.*, 2009. **103**(14): p. 146401.
23. Checkelsky, J.G., et al., *Dirac-fermion-mediated ferromagnetism in a topological insulator*. *Nature Phys.*, 2012. **8**(10): p. 729-733.
24. Butch, N.P., et al., *Strong surface scattering in ultrahigh-mobility Bi_2Se_3 topological insulator crystals*. *Phys. Rev. B*, 2010. **81**(24): p. 241301.
25. Kong, D., et al., *Ambipolar field effect in the ternary topological insulator $(\text{Bi}_x\text{Sb}_{1-x})_2\text{Te}_3$ by composition tuning*. *Nature Nanotech.*, 2011. **6**(11): p. 705-709.
26. Sacépé, B., et al., *Gate-tuned normal and superconducting transport at the surface of a topological insulator*. *Nature Comm.*, 2011. **2**: p. 575.
27. Checkelsky, J.G., et al., *Bulk band gap and surface state conduction observed in voltage-tuned crystals of the topological insulator Bi_2Se_3* . *Phys. Rev. Lett.*, 2011. **106**(19): p. 196801.
28. Kim, D., et al., *Surface conduction of topological Dirac electrons in bulk insulating Bi_2Se_3* . *Nature Phys.*, 2012. **8**(6): p. 459-463.
29. Kim, D., et al., *Intrinsic electron-phonon resistivity of Bi_2Se_3 in the topological regime*. *Phys. Rev. Lett.*, 2012. **109**(16): p. 166801.

30. Hwang, E.H., S. Adam, and S. Das Sarma, *Carrier Transport in Two-Dimensional Graphene Layers*. *Phys. Rev. Lett.*, 2007. **98**(18): p. 186806.
31. Adam, S., et al., *A self-consistent theory for graphene transport*. *Proc. Natl. Acad. Sci. U. S. A.*, 2007. **104**(47): p. 18392-18397.
32. Das Sarma, S., et al., *Electronic transport in two-dimensional graphene*. *Rev. Mod. Phys.*, 2011. **83**(2): p. 407-470.
33. Hwang, E.H. and S. Das Sarma, *Dielectric function, screening, and plasmons in two-dimensional graphene*. *Physical Review B*, 2007. **75**(20): p. 205418.
34. Culcer, D., *Transport in three-dimensional topological insulators: Theory and experiment*. *Phys. E.*, 2012. **44**(5): p. 860-884.
35. Culcer, D., et al., *Two-dimensional surface charge transport in topological insulators*. *Phys. Rev. B.*, 2010. **82**(15): p. 155457.
36. Adam, S., E.H. Hwang, and S. Das Sarma, *Two-dimensional transport and screening in topological insulator surface states*. *Phys. Rev. B.*, 2012. **85**(23): p. 235413.
37. Martin, J., et al., *Observation of electron-hole puddles in graphene using a scanning single-electron transistor*. *Nature Phys.*, 2008. **4**(2): p. 144-148.
38. Zhu, Z.H., et al., *Rashba spin-splitting control at the surface of the topological insulator Bi_2Se_3* . *Phys. Rev. Lett.*, 2011. **107**(18): p. 186405.
39. Taskin, A.A., et al., *Manifestation of topological protection in transport properties of epitaxial Bi_2Se_3 thin films*. *Phys. Rev. Lett.*, 2012. **109**(6): p. 066803.
40. Park, J., et al., *Crystal structure and epitaxy of Bi_2Te_3 films grown on Si*. *Appl. Phys. Lett.*, 2012. **101**(22): p. 221910-5.
41. Novoselov, K.S., et al., *Two-dimensional gas of massless Dirac fermions in graphene*. *Nature*, 2005. **438**(7065): p. 197-200.
42. Dean, C.R., et al., *Boron nitride substrates for high-quality graphene electronics*. *Nature Nanotech.*, 2010. **5**(10): p. 722-726.
43. RadisavljevicB, et al., *Single-layer MoS_2 transistors*. *Nature Nanotech.*, 2011. **6**(3): p. 147-150.
44. Braga, D., et al., *Quantitative determination of the band gap of WS_2 with ambipolar ionic liquid-gated transistors*. *Nano Lett.*, 2012. **12**(10): p. 5218-5223.

45. Zhang, Y., B. de Boer, and P.W.M. Blom, *Controllable molecular doping and charge transport in solution-processed polymer semiconducting layers*. *Adv. Func. Mat.*, 2009. **19**(12): p. 1901-1905.
46. Pinto, H., et al., *p-type doping of graphene with F4-TCNQ*. *Journal of Physics: Cond. Matt.*, 2009. **21**(40): p. 402001.
47. Efetov, D.K. and P. Kim, *Controlling electron-phonon interactions in graphene at ultrahigh carrier densities*. *Phys. Rev. Lett.*, 2010. **105**(25): p. 256805.
48. Bansal, N., et al., *Thickness independent transport channels in topological insulator Bi_2Se_3 Thin Films*. *Phys. Rev. Lett.*, 2012. **109**(11): p. 116804.
49. Kong, D., et al., *Rapid surface oxidation as a source of surface degradation dactor for Bi_2Se_3* . *ACS Nano*, 2011. **5**(6): p. 4698-4703.
50. Ren, Z., et al., *Large bulk resistivity and surface quantum oscillations in the topological insulator Bi_2Te_2Se* . *Phys. Rev. B.*, 2010. **82**(24): p. 241306.
51. Steinberg, H., et al., *Surface state transport and ambipolar electric field effect in Bi_2Se_3 nanodevices*. *Nano Lett.*, 2010. **10**(12): p. 5032-5036.
52. Pershoguba, S.S. and V.M. Yakovenko, *Spin-polarized tunneling current through a thin film of a topological insulator in a parallel magnetic field*. *Phys. Rev. B.*, 2012. **86**(16): p. 165404.
53. Beidenkopf, H., et al., *Spatial fluctuations of helical Dirac fermions on the surface of topological insulators*. *Nature Phys.*, 2011. **7**(12): p. 939-943.
54. Ojeda-Aristizabal, C., et al., *Towards spin injection from silicon into topological insulators: Schottky barrier between Si and Bi_2Se_3* . *Appl. Phys. Lett.*, 2012. **101**(2): p. 023102-4.
55. Appelbaum, I., H.D. Drew, and M.S. Fuhrer, *Proposal for a topological plasmon spin rectifier*. *Appl. Phys. Lett.*, 2011. **98**(2): p. 023103-3.
56. McIver, J.W., et al., *Control over topological insulator photocurrents with light polarization*. *Nature Nanotech.*, 2012. **7**(2): p. 96-100.
57. Pietronero, L., et al., *Electrical conductivity of a graphite layer*. *Phys. Rev. B.*, 1980. **22**(2): p. 904-910.
58. Chen, J.-H., et al., *Intrinsic and extrinsic performance limits of graphene devices on SiO_2* . *Nature Nanotech.*, 2008. **3**(4): p. 206-209.

59. Kuroda, K., et al., *Hexagonally deformed fermi surface of the 3D topological insulator Bi_2Se_3* . *Phys. Rev. Lett.*, 2010. **105**(7): p. 076802.
60. Hatch, R.C., et al., *Stability of the Bi_2Se_3 (111) topological state: Electron-phonon and electron-defect scattering*. *Phys. Rev. B.*, 2011. **83**(24): p. 241303.
61. Pan, Z.H., et al., *Measurement of an exceptionally weak electron-phonon coupling on the surface of the topological insulator Bi_2Se_3 using angle-resolved photoemission spectroscopy*. *Phys. Rev. Lett.*, 2012. **108**(18): p. 187001.
62. Zhu, X., et al., *Electron-phonon coupling on the surface of the topological insulator Bi_2Se_3 determined from surface-phonon dispersion measurements*. *Phys. Rev. Lett.*, 2012. **108**(18): p. 185501.
63. Yan, Y., et al., *Synthesis and quantum transport properties of Bi_2Se_3 topological insulator nanostructures*. *Sci. Rep.*, 2013. **3**.
64. Liu, C.-X., et al., *Model Hamiltonian for topological insulators*. *Phys. Rev. B.*, 2010. **82**(4): p. 045122.
65. Li, Q., E.H. Hwang, and S. Das Sarma, *Disorder-induced temperature-dependent transport in graphene: puddles, impurities, activation, and diffusion*. *Phys. Rev. B.*, 2011. **84**(11): p. 115442.
66. Hwang, E.H. and S. Das Sarma, *Acoustic phonon scattering limited carrier mobility in two-dimensional extrinsic graphene*. *Phys. Rev. B*, 2008. **77**(11): p. 115449.
67. Giraud, S., A. Kundu, and R. Egger, *Electron-phonon scattering in topological insulator thin films*. *Phys. Rev. B.*, 2012. **85**(3): p. 035441.
68. Li, Q., E. Rossi, and S. Das Sarma, *Two-dimensional electronic transport on the surface of three-dimensional topological insulators*. *Phys. Rev. B.*, 2012. **86**(23): p. 235443.
69. Altland, A. and M.R. Zirnbauer, *Nonstandard symmetry classes in mesoscopic normal-superconducting hybrid structures*. *Phys. Rev. B.*, 1997. **55**(2): p. 1142-1161.
70. Hikami, S., A.I. Larkin, and Y. Nagaoka, *Spin-orbit interaction and magnetoresistance in the two dimensional random system*. *Prog. Theor. Phys.*, 1980. **63**(2): p. 707-710.
71. Bergmann, G., *Weak localization in thin films: a time-of-flight experiment with conduction electrons*. *Phys. Rep.*, 1984. **107**(1): p. 1-58.

72. Suzuura, H. and T. Ando, *Crossover from symplectic to orthogonal class in a two-dimensional honeycomb lattice*. *Phys. Rev. Lett.*, 2002. **89**(26): p. 266603.
73. McCann, E., et al., *Weak-localization magnetoresistance and calley symmetry in graphene*. *Phys. Rev. Lett.*, 2006. **97**(14): p. 146805.
74. Steinberg, H., et al., *Electrically tunable surface-to-bulk coherent coupling in topological insulator thin films*. *Phys. Rev. B.*, 2011. **84**(23): p. 233101.
75. Chen, J., et al., *Gate-voltage control of chemical potential and weak antilocalization in Bi_2Se_3* . *Phys. Rev. Lett.*, 2010. **105**(17): p. 176602.
76. Chen, J., et al., *Tunable surface conductivity in Bi_2Se_3 revealed in diffusive electron transport*. *Phys. Rev. B.*, 2011. **83**(24): p. 241304.
77. Garate, I. and L. Glazman, *Weak localization and antilocalization in topological insulator thin films with coherent bulk-surface coupling*. *Phys. Rev. B.*, 2012. **86**(3): p. 035422.
78. Kim, Y.S., et al., *Thickness-dependent bulk properties and weak antilocalization effect in topological insulator Bi_2Se_3* . *Phys. Rev. B.*, 2011. **84**(7): p. 073109.
79. He, H.-T., et al., *Impurity effect on weak antilocalization in the topological insulator Bi_2Te_3* . *Phys. Rev. Lett.*, 2011. **106**(16): p. 166805.
80. Matsuo, S., et al., *Weak antilocalization and conductance fluctuation in a submicrometer-sized wire of epitaxial Bi_2Se_3* . *Phys. Rev. B.*, 2012. **85**(7): p. 075440.
81. Zhang, Y., et al., *Crossover of the three-dimensional topological insulator Bi_2Se_3 to the two-dimensional limit*. *Nat Phys*, 2010. **6**(8): p. 584-588.
82. Murakami, S., N. Nagaosa, and S.-C. Zhang, *Spin-Hall insulator*. *Phys. Rev. Lett.*, 2004. **93**(15): p. 156804.
83. Cho, S., et al., *Insulating behavior in ultrathin bismuth selenide field effect transistors*. *Nano Lett.*, 2011. **11**(5): p. 1925-1927.
84. Wang, J., et al., *Evidence for electron-electron interaction in topological insulator thin films*. *Phys. Rev. B.*, 2011. **83**(24): p. 245438.
85. Liu, M., et al., *Electron interaction-driven insulating ground state in Bi_2Se_3 topological insulators in the two-dimensional limit*. *Phys. Rev. B.*, 2011. **83**(16): p. 165440.

86. Linder, J., T. Yokoyama, and A. Sudbø, *Anomalous finite size effects on surface states in the topological insulator Bi_2Se_3* . *Phys. Rev. B.*, 2009. **80**(20): p. 205401.
87. Lang, M., et al., *Competing weak localization and weak antilocalization in ultrathin topological insulators*. *Nano Lett.*, 2012. **13**(1): p. 48-53.
88. Taskin, A.A., et al., *Observation of dirac holes and electrons in a topological insulator*. *Phys. Rev. Lett.*, 2011. **107**(1): p. 016801.
89. Pesin, D. and A.H. MacDonald, *Spintronics and pseudospintronics in graphene and topological insulators*. *Nat Mater*, 2012. **11**(5): p. 409-416.
90. Qu, F., et al., *Strong Superconducting Proximity Effect in $\text{Pb-Bi}_2\text{Te}_3$ Hybrid Structures*. *Sci. Rep.*, 2012. **2**.